

**ANALYSIS OF THE UNUSUAL DIPS IN ECLIPSING
WDMS BINARY SYSTEM: SDSS J102102.25+174439.9**



**A Thesis Submitted in Partial Fulfillment of the Requirements for the
Degree of Master of Science in Applied Physics
Suranaree University of Technology
Academic Year 2016**

การวิเคราะห์การลดลงที่ผิดจากธรรมดาของระบบดาวคู่อุปราคาแบบดาวแถบ
ลำดับหลักและดาวแคระขาว: SDSS J102102.25+174439.9



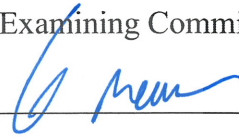
วิทยานิพนธ์นี้เป็นส่วนหนึ่งของการศึกษาตามหลักสูตรปริญญาวิทยาศาสตรมหาบัณฑิต
สาขาวิชาฟิสิกส์ประยุกต์
มหาวิทยาลัยเทคโนโลยีสุรนารี
ปีการศึกษา 2559

ANALYSIS OF THE UNUSUAL DIPS IN ECLIPSING WDMS

BINARY SYSTEM: SDSS J102102.25+174439.9

Suranaree University of Technology has approved this submitted in partial fulfillment of requirement for a Master's Degree.

Thesis Examining Committee



(Asst. Prof. Dr. Worawat Meevasana)

Chairperson



(Dr. Nuanwan Sanguansak)

Member (Thesis Advisor)



(Dr. Puji Irawati)

Member



(Asst. Prof. Dr. Amornrat Aungwerojwit)

Member



(Prof. Dr. Santi Maensiri)

Vice Rector for Academic Affairs
and Internationalisation



(Asst. Prof. Dr. Worawat Meevasana)

Dean of Institute of Science

คุณากร จันท : การวิเคราะห์การลดลงที่ผิดปกติจากธรรมดาของระบบดาวคู่อุปราคาแบบดาว
แถบลำดับหลักและดาวแคระขาว: SDSS J102102.25+174439.9 (ANALYSIS OF THE
UNUSUAL DIPS IN ECLIPSING WDMS BINARY SYSTEM: SDSS J102102.25
+174439.9) อาจารย์ที่ปรึกษา : อาจารย์ ดร.นवलวรรณ สงวนศักดิ์, 143 หน้า.

งานวิจัยนี้เราได้ศึกษาระบบดาวคู่อุปราคาใหม่ SDSS J102102.25+174439.9 แบบดาว
แคระขาวและดาวในแถบลำดับหลัก โดยมีคาบการโคจร 0.14 วัน อยู่ในช่วงของการวิวัฒนาการ
หลังวิวัฒนาการร่วมกัน ซึ่งเราได้ทำการสังเกตการณ์และเก็บข้อมูลผ่านกล้องโทรทรรศน์ ขนาดเส้นผ่าน
ศูนย์กลาง 2.4 เมตร ณ หอดูดาวเฉลิมพระเกียรติ 7 รอบพระชนมพรรษา จ.เชียงใหม่ ร่วมกับ
อุปกรณ์ ULTRASPEC โดยใช้แผ่นกรองแสง $g'r'i'z'$ KG5 และ $i'+z'$ จากข้อมูลที่ได้รับในหลาย
ช่วงความยาวคลื่นนั้นพบว่าการลดลงของความสว่างหลังจากการเกิดอุปราคาปฐมภูมิได้ประมาณ
15 นาที ซึ่งคล้ายกับกรณีการปล่อยมวลสารออกมาจากดาวในแถบลำดับหลัก จากการติดตามการ
เปลี่ยนแปลงความสว่างที่ลดลงอย่างผิดปกติเป็นเวลา 2 ปี พบว่าตำแหน่งที่ลดลงอย่างผิดปกตินี้อยู่
ใกล้กับบริเวณจุดลากรางเจียน L_5 อย่างไรก็ตามยังไม่พบความสัมพันธ์ในการลดลงของความสว่าง
เทียบกับเวลาที่เกิด จากแบบจำลองของระบบดาวคู่พบว่าค่าพารามิเตอร์ได้แก่ อัตราส่วนระหว่าง
มวลของดาวในแถบลำดับหลักและดาวแคระขาว (M_2/M_1) เท่ากับ 0.6004 ± 0.0005 อุณหภูมิยังผล
ของดาวแคระขาวและดาวในแถบลำดับหลักเท่ากับ 17000 ± 273 K และ 3182 ± 48 K ตามลำดับ
ความเอียงของระนาบการโคจรนี้คือ 81.07 ± 0.21 องศา รัศมีของดาวแคระขาวเท่ากับ $0.0112 \pm$
 $0.0001 R_\odot$ และรัศมีดาวในแถบลำดับหลักเท่ากับ $0.3488 \pm 0.0001 R_\odot$ และค่าคาบการโคจรของ
ระบบมีค่าเท่ากับ 0.14036 ± 0.00001 วัน

สาขาวิชาฟิสิกส์
ปีการศึกษา 2559

ลายมือนักศึกษา คุณากร จันท
ลายมือชื่ออาจารย์ที่ปรึกษา นอววรรณ สงวนศักดิ์
ลายมือชื่ออาจารย์ที่ปรึกษาร่วม [ลายมือ]

KHUNAGORN CHANTHORN : ANALYSIS OF THE UNUSUAL DIPS IN
ECLIPSING WDMS BINARY SYSTEM: SDSS J102102.25+174439.9.

THESIS ADVISOR : NUANWAN SANGUANSACK, Ph.D. 143 PP.

ECLIPSING/BIANRY STAR/SDSS J102102.25+174439.9/DIPS

In this work, we have studied the eclipsing post common envelope binary system, SDSS J102102.25 +174439.9 with an orbital period of 0.14 days. The data were obtain from the 2.4-meter telescope at the Thai National Observatory (TNO), Chiang Mai, with ULTRASPEC instrument using filters g' , r' , i' , z' KG5 and $i'+z'$. The drops in brightness appeared after 15 minutes of the primary eclipse. This is similar to the mass ejection from a main-sequence star. The unusual dips of brightness have been observed and studied over the past 2 years. We found the position of abnormal dips occurred near the Lagrange point L_5 . However, there is no correlation between the decrease of brightness and the time of the occurred dips. The parameters of eclipsing binary system are as follows: mass ratio of main-sequence and white dwarf (M_2/M_1) = 0.6004 ± 0.0005 , the effective temperature of the white dwarf and main-sequence are 17000 ± 273 K and 3182 ± 48 K respectively, the orbital inclination = 81.07 ± 0.21 degree, radii of the white dwarf = $0.0112 \pm 0.0001R_{\odot}$, radii of the main-sequence = $0.3488 \pm 0.0001R_{\odot}$ and the orbital period of the system is 0.14036 ± 0.00001 days.

School of Physics

Academic Year 2016

Student's Signature Khunagorn Chanthorn

Advisor's Signature N. Sanguansack

Co-advisor's Signature

ACKNOWLEDGEMENTS

I am very grateful to Dr. Nuanwan Sanguangsak. My thesis cannot be finished without her support, guidance, inspiring and kindness since the beginning of my research. I would like to thank Dr. Puji Irawati for her support and guidance in using the instruments, the data processing and including writing this thesis.

I appreciate the guidance and comments from Asst. Prof. Dr. Worawat Meevasana and Asst. Prof. Dr. Amornrat Aungwerojwit as my thesis committees.

I would like to thank the Synchrotron Radiation and Renewal Energy Research unit of Suranaree University of Technology for supporting my graduate study and the National Astronomical Research Institute of Thailand (Public Organization), Ministry of Science and Technology, Thailand for allowing me to use Thai National Telescope (2.4 meter).

I appreciate the help from Miss Napaporn A-thano for training me to analyze the data and using PHOEBE software to construct a model, Dr. Supachai Awipan and Miss Nareemas Chehlaeh for very useful comments. I would also like to thank all of the technicians teams at TNO for guiding me how to use instruments. Constructive comments and suggestions from Mr. Niwat Hemha, Mr. Kittipong Wangnok, Mr. Anut Sangka and all members of the SUT astrophysics group are greatly appreciated. Finally, I would like to thank my parent for their love, all the support and being there whenever I needed it.

Khunagorn Chanthorn

CONTENTS

| | Page |
|--|-------------|
| ABSTRACT IN THAI..... | I |
| ABSTRACT IN ENGLISH..... | II |
| ACKNOWLEDGEMENTS..... | III |
| CONTENTS..... | IV |
| LIST OF TABLES..... | VIII |
| LIST OF FIGURES..... | X |
| LIST OF ABBREVIATIONS..... | XIII |
| CHAPTER | |
| I INTRODUCTION..... | 1 |
| 1.1 Post-common envelope binaries evolution..... | 1 |
| 1.2 Motivation..... | 2 |
| 1.3 Thesis objectives..... | 3 |
| II THEORY..... | 5 |
| 2.1 Binary stars..... | 5 |
| 2.1.1 Classification of close binaries..... | 5 |
| 2.1.1.1 Detached binaries..... | 5 |
| 2.1.1.2 Semidetached binaries..... | 6 |
| 2.1.1.3 Contact binaries..... | 7 |
| 2.1.2 Orbital properties of close binaries..... | 8 |

CONTENTS (Continued)

| | Page |
|---|-------------|
| 2.2 Roche geometry..... | 9 |
| 2.3 Lagrangian points..... | 14 |
| 2.4 Trojan..... | 18 |
| 2.5 Common envelope evolution..... | 19 |
| 2.5.1 The formation of the common envelope..... | 19 |
| 2.5.2 The common envelope phase..... | 19 |
| 2.6 White dwarf..... | 21 |
| 2.7 M-type stars..... | 21 |
| 2.8 Mass ejection..... | 22 |
| 2.9 Time scale for periodic of eclipses..... | 22 |
| 2.10 Ephemeris parameters and O-C diagram..... | 25 |
| 2.11 Ellipsoidal variations..... | 27 |
| III METHODOLOGY..... | 29 |
| 3.1 Observation..... | 29 |
| 3.2 Data reduction..... | 34 |
| 3.2.1 Bias frames..... | 37 |
| 3.2.2 Flat-fielding..... | 38 |
| 3.2.3 Reducing data..... | 38 |
| 3.3 Light curve analysis..... | 39 |

CONTENTS (Continued)

| | Page |
|--|-------------|
| 3.4 The initial parameters..... | 42 |
| 3.4.1 Orbital separation..... | 42 |
| 3.4.2 Inclination..... | 42 |
| 3.4.3 The mass ratio..... | 43 |
| 3.4.4 Semi-major axis..... | 43 |
| 3.4.5 Effective temperature..... | 43 |
| 3.4.6 Modified omega potential..... | 44 |
| 3.4.7 Limb darkening..... | 44 |
| 3.4.8 Reflection effect..... | 44 |
| 3.4.9 Gravity darkening..... | 45 |
| 3.4.10 Third light..... | 45 |
| 3.4.11 Surface brightness ratio..... | 45 |
| 3.5 Software for modeling binary star..... | 45 |
| 3.5.1 JKTEBOP code..... | 46 |
| 3.5.2 PHOEBE..... | 47 |
| 3.5.3 Binary Maker 3.0..... | 50 |
| 3.6 Roche lobe of SDSS J1021+1744..... | 52 |
| IV RESULTS..... | 61 |
| 4.1 Light curve model fitting..... | 64 |
| 4.1.1 The modeling using JKTEBOP code..... | 64 |
| 4.1.2 The O-C diagram..... | 68 |

CONTENTS (Continued)

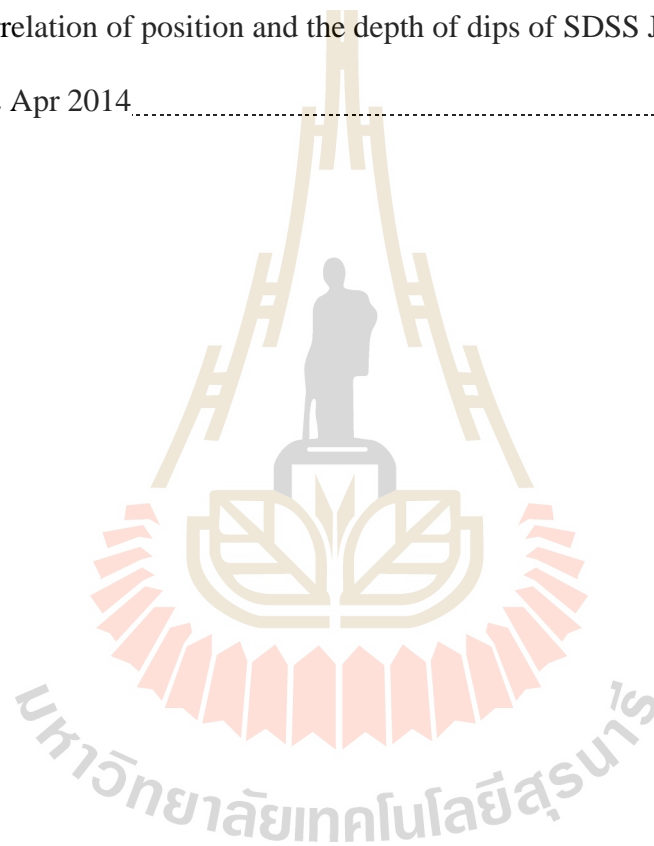
| | Page |
|---|-------------|
| 4.1.3 The modeling using PHOEBE..... | 69 |
| 4.1.4 The modeling using Binary Maker 3.0..... | 74 |
| 4.2 Dips in SDSS J1021+1744..... | 78 |
| V DISCUSSION AND CONCLUSIONS..... | 85 |
| 5.1 Discussions..... | 85 |
| 5.2 Conclusions..... | 94 |
| 5.3 Future pan..... | 98 |
| REFERENCES..... | 100 |
| APPENDIXCES..... | 104 |
| APPENDIX A MORPHOLOGIES AND ROCHE LOBES OF CLOSE BINARY STARS..... | 105 |
| APPENDIX B LIGHT CURVE OF SDSS J1021+1744..... | 125 |
| CURRICULUM VITE..... | 143 |

LIST OF TABLES

| Table | | Page |
|--------------|--|-------------|
| 3.1 | ULTRASPEC filters..... | 30 |
| 3.2 | Database for observation from Aladin Sky Atlas..... | 33 |
| 3.3 | Time of observation of SDSS J1021+1744 sine 2014 to 2016..... | 35 |
| 3.4 | The initial parameters inputting in JKTEBOP..... | 47 |
| 3.5 | The initial parameters inputting in PHOEBE..... | 48 |
| 3.6 | The initial parameters inputting in BM3..... | 51 |
| 3.7 | The result from calculation of r_{L1} and L_1 | 53 |
| 3.8 | The result from calculation of r_{L2} and L_2 | 55 |
| 3.9 | T The result from calculation of r_{L3} .and L_3 | 56 |
| 3.10 | Position of Lagrange point..... | 58 |
| 3.11 | The binary system parameter of SDSS J1021+1744 from the calculation..... | 59 |
| 4.1 | The time of mid-eclipse for SDSS J1021+1744 using JKTEBOP..... | 62 |
| 4.2 | Result parameters of SDSS J1021+1744 using JKTEBOP code..... | 65 |
| 4.3 | Results parameters of SDSS J1021+1744 using PHEOBE..... | 72 |
| 4.4 | The best fit model SDSS J1021+1744 from PHOEBE..... | 73 |
| 4.5 | The output result of SDSS J1021+1744 using BM3..... | 76 |
| 4.6 | The result parameter of SDSS J1021+1744 from calculation and modeling with BM3, PHOEBE and JKTEBOP code with r' filter..... | 82 |

LIST OF TABLES (Continued)

| Table | | Page |
|--------------|--|-------------|
| 4.7 | Compared result of our model of SDSS J1021+1744 with the parameters from Parsons et al., 2013, Irawati et al., 2016 and Parsons et al., 2017 | 84 |
| 5.1 | The correlation of position and the depth of dips of SDSS J1021+1744 on 28 Jan to 2 Apr 2014..... | 95 |



LIST OF FIGURES

| Figure | Page |
|--|-------------|
| 1.1 Light curve of SDSS J1021+1744 system from Parsons et al. (2013)..... | 2 |
| 1.2 The spectrum of SDSS J1021+1744..... | 3 |
| 2.1 Detached binary..... | 6 |
| 2.2 Semi-detached binary..... | 7 |
| 2.3 Contact binary star..... | 7 |
| 2.4 The coordinate of two mass system..... | 10 |
| 2.5 The surfaces of constant normalized potential with mass ratio 0.4..... | 12 |
| 2.6 The contact point of the Roche lobe..... | 15 |
| 2.7 Lagrangian points in a rotating of two-body system..... | 17 |
| 2.8 The Trojan asteroids in the Sun-Jupiter system..... | 18 |
| 2.9 The evolution of post-common envelope binary (PCEB)..... | 20 |
| 2.10 The light curve variation of a detached binary due to ellipsoidal variations..... | 28 |
| 3.1 The Transmission profile of ULTRASPEC SDSS filter..... | 30 |
| 3.2 The visibility of SDSS J1021+1744 on 7 Jan 2014..... | 31 |
| 3.3 ULTRASPEC Finding Chart..... | 32 |
| 3.4 The process of combine bias..... | 37 |
| 3.5 The process of flat subtraction..... | 38 |
| 3.6 The process of data reduction..... | 39 |
| 3.7 The first observation light curve of SDSS J1021+1744 and reference..... | 40 |

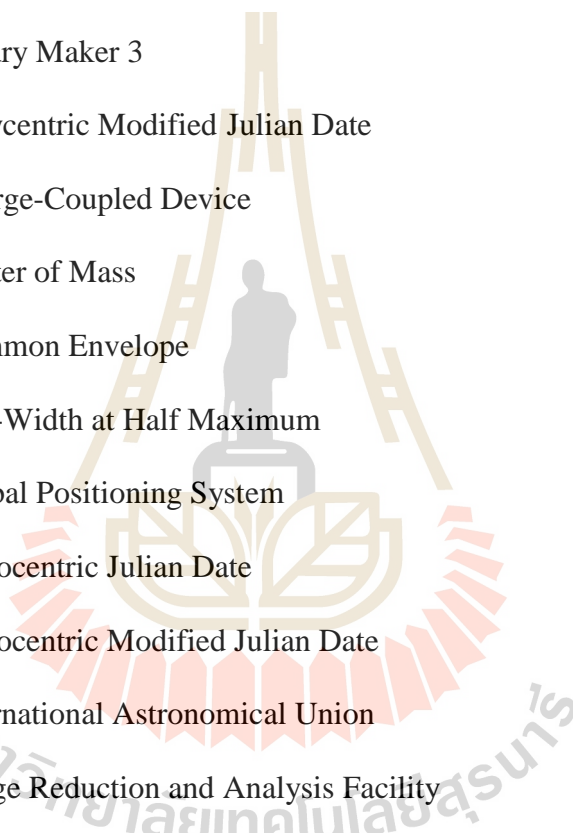
LIST OF FIGURES (Continued)

| Figure | Page |
|--|-------------|
| 3.8 The light curve of SDSS J1021+1744 in g' filter (7 Jan 2014)..... | 40 |
| 3.9 The light curve of SDSS J1021+1744 in SDSS $i'+z'$ filter (11 Jan 2014)..... | 41 |
| 3.10 The light curve of SDSS J1021+1744 in SDSS KG5 filter (28 Jan 2014)..... | 41 |
| 3.11 The light curve of SDSS J1021+1744 in SDSS r' filter (29 MAR 2014)..... | 42 |
| 3.12 The display of PHOEBE, shows the initial input parameters..... | 49 |
| 3.13 The display for the result of the observational data using PHOEBE..... | 49 |
| 3.14 The BM3 display..... | 51 |
| 3.15 The results of the analysis solution of r | 54 |
| 3.16 The Roche lobe inner potential of SDSS J1021+1744..... | 57 |
| 3.17 The Lagrange L_4 and L_5 | 58 |
| 3.18 The position of the Lagrange points L_1 to L_5 of this binary system..... | 60 |
| 4.1 Model with JKTEBOP code on 29 Mar 2014 (Filter r')..... | 66 |
| 4.2 Model with JKTEBOP code on 17 Jan 2015 (filter g')..... | 66 |
| 4.3 Model with JKTEBOP code on 24 Feb 2015 (filter KG5)..... | 67 |
| 4.4 Model with JKTEBOP code on 15 Mar 2015 (filter i')..... | 67 |
| 4.5 Model with JKTEBOP code on 12 Jan 2014 (filter $i'+z'$)..... | 68 |
| 4.6 The O-C diagram of SDSS J1021+1744 using JKTEBOP code..... | 69 |
| 4.7 The best fit model of light curves and residuals using PHOEBE..... | 70 |
| 4.8 Show phase orientations of SDSS J1021+1744 using PHOBE..... | 71 |
| 4.9 The result of the best fit light curve model of SDSS J1021+1744..... | 75 |

LIST OF FIGURES (Continued)

| Figure | Page |
|--|-------------|
| 4.10 Show phase orientations of SDSS J1021+1744 using BM3 | 77 |
| 4.11 The light curve close up the dips in 2014 | 79 |
| 4.12 The light curve close up the dips in 2015 and 2016 | 80 |
| 4.13 The light curve show the position of two dips in 7 Jan 2014 | 81 |
| 4.14 The position of two dips in 7 Jan 2014 on the top view | 81 |
| 5.1 Show two pre-eclipse dips in light curve of QS Virinis | 86 |
| 5.2 Show dips in soft X-ray flux in light curve of V471 Tauri | 87 |
| 5.3 Shows the schematic of V471 Tauri binary system | 88 |
| 5.4 The close up light curve in 2014 with number of dips | 89 |
| 5.5 The close up light curve in 2015 to 2016 with number of dips | 90 |
| 5.6 The model of dips position in 1 April 2014 with g' filter | 91 |
| 5.7 The model of dips position in 19 February 2015 with g' filter | 92 |
| 5.8 The correlation of flux versus time and position of dips versus time | 93 |
| 5.9 The dip number 3 was diffusing in 2014 | 96 |
| 5.10 The ellipsoidal light curves in i' filter on 30 Jan 2014 | 97 |
| 5.11 The large flare on SDSS J1021+1744 in r' filter on 31 Mar 2014 | 98 |
| 5.12 The dip of SDSS J1021+1744 come back on 26 Jan 2017 in KG5 filter | 99 |

LIST OF ABBREVIATIONS



| | |
|--------|---------------------------------------|
| AU | Astronomical Unit |
| BJD | Barycentric Julian Date |
| BM3 | Binary Maker 3 |
| BMJD | Barycentric Modified Julian Date |
| CCD | Charge-Coupled Device |
| CoM | Center of Mass |
| CE | Common Envelope |
| FWHM | Full-Width at Half Maximum |
| GPS | Global Positioning System |
| HJD | Heliocentric Julian Date |
| HMJD | Heliocentric Modified Julian Date |
| IAU | International Astronomical Union |
| IRAF | Image Reduction and Analysis Facility |
| JD | Julian Date |
| MJD | Modified Julian Date |
| PCEB | Post Common Envelope Binary |
| SDSS | Sloan Digital Sky Survey |
| PHOEBE | Physics of Eclipsing Binaries program |
| SI | International System of Units |
| TAI | International Atomic Time |

LIST OF ABBREVIATIONS (Continued)

| | |
|------|-------------------------------|
| TDB | Barycentric Dynamical Time |
| TDT | Terrestrial Dynamical Time |
| TNO | Thai National Observatory |
| TNT | Thai National Telescope |
| TT | Terrestrial Time |
| UTC | Coordinated Universal Time |
| UT | Universal Time |
| WD | White Dwarf |
| WHT | William Herschel Telescope |
| WDMS | White Dwarf and Main-Sequence |

CHAPTER I

INTRODUCTION

The point of light in the night time sky that we call stars can be divided into two categories. There are the truly single stars, like the Sun, which may happen to have a retinue of planets in orbit around them, with the total planetary masses less than one thousandth of their host star mass. There is also binary star moving in bound orbits about their common center of mass (Hilditch, 2001). Binary stars are important because they allow for direct measurement of the stellar masses, radii, and luminosities. We can easily classify them into four types according to their method of detection: visual binaries, spectroscopic binaries, astrometric binaries and eclipsing binaries.

1.1 Post-common envelope binaries evolution

Most stars in the sky are more generally in binary systems or multiple systems. These systems, especially when more distance, often appear to the unaided eye as a single point of light and are then revealed as double (or more) by other means. Research over the last two centuries suggests that half or more of visible stars are part of multiples star systems.

The binary system consists of two main sequence stars in which the more massive star evolved through the giant phase and fills the Roche lobe where the star's envelope expands considerably. If the system fulfills the requirements of an

unstable mass transfer, the secondary star will fall into the envelope of the primary where the two stars share a common envelope.

1.2 Motivation

In the paper by Parsons et al. (2013) shows unusual dips in the light curve of SDSS J102102.25+174439.9 (SDSS J1021+1744) in Figure 1.1. The unusual dips are our main motivation to study this system further. Dips in WDMS systems were observed only one occasion in the light curve of QS Vir prior to the eclipse of the white dwarf (O'Donoghue et al., 2003). If this is the case, then a large amount of material must have been ejected therefore almost half of the white dwarf flux is blocked. Their spectrum data is also presented in Figure 1.2. The hydrogen Balmer lines are indicated by solid lines (absorption features come from the white dwarf, emission features indicate an active or irradiated main-sequence star, spectrum type M4) and the Na I lines are indicated by the dashed lines absorption from the main-sequence star (Parsons et al., 2013 and Rebassa-Mansergas et al., 2012).

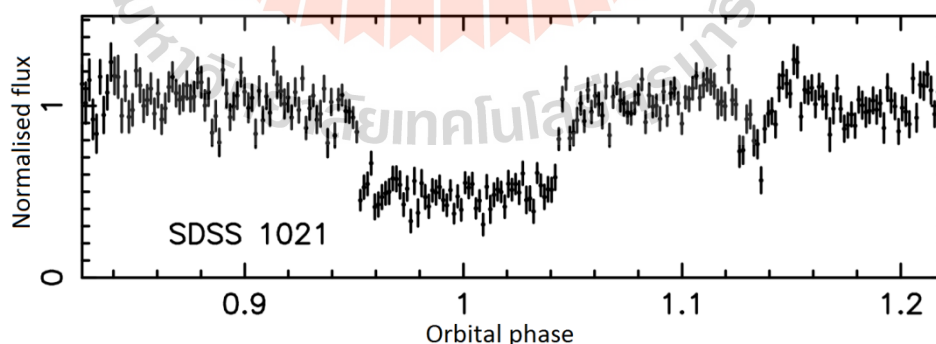


Figure 1.1 Shows the dip around orbital phase 1.1-1.2 after primary eclipse about 15 minutes of SDSS J1021+1744 system (taken from Parsons et al., 2013).

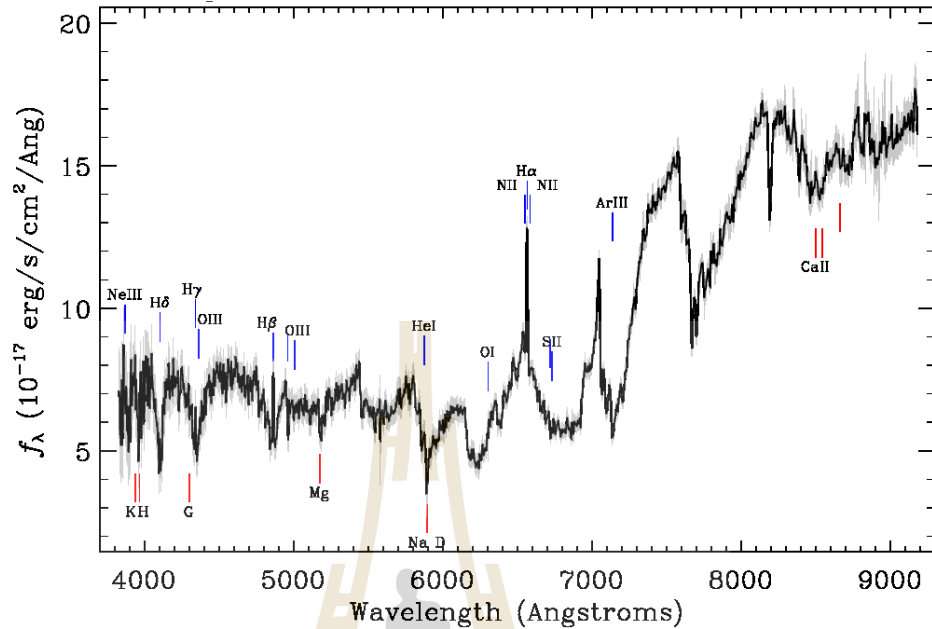


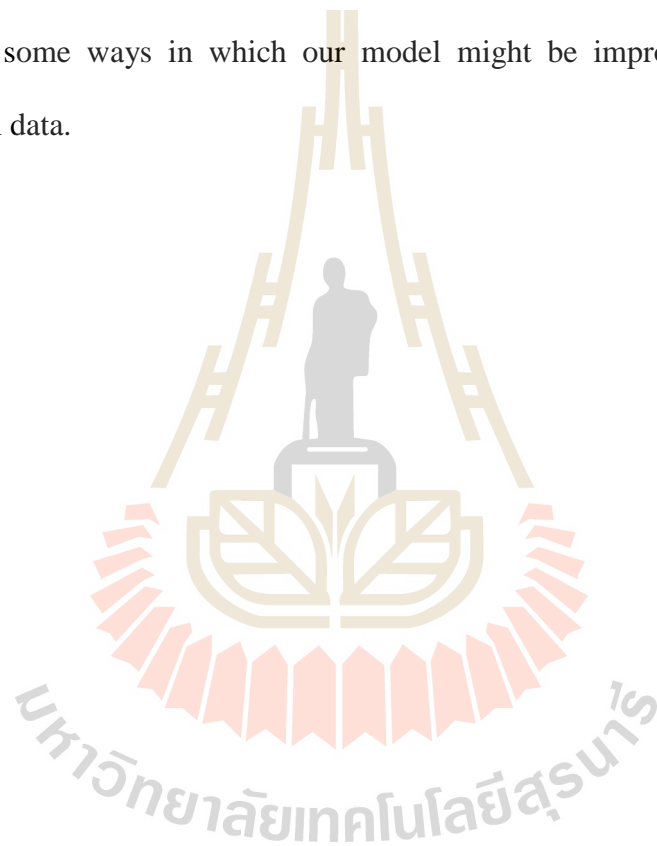
Figure 1.2 The spectrum of SDSS J1021+1744 obtained from Quick Look of SkyServer DR9 of Sloan Digital Sky Survey, where x-axis is the wavelength (angstroms) and y-axis is Intensity of light. The emission lines are marked in blue, while the absorption lines are marked in red.

1.3 Thesis objectives

1. To study the eclipsing white dwarf plus main-sequence binary system, SDSS J1021+1744 with distinctive and long lasting dips.
2. To understand the possible causes of unusual dips.

In the next chapter, we will introduce the post common envelope binaries white dwarf plus main-sequence M-type star and cause of mass ejection. In the third chapter, we will present the ULTRASPEC instrument installed on the 2.4-meter

telescope at the Thai National Observatory (TNO) and persistent drop in brightness after the primary eclipse in multi-wavelength. These dips, which appear to show variations in amplitude, also have a complex shape that change within days. An expected result, light curve fitting and dips feature changed with time in SDSS J1021+1744 are presented in chapter four. Finally in the last chapter, we discuss how the dips position and amplitude change with time, draw the conclusion of the model and suggest some ways in which our model might be improved following more observational data.



CHAPTER II

THEORY

2.1 Binary stars

Two stars rotate around their common center of mass; their individual evolution may be affected by their companion. The combination of the gravitational potential of each star and the centrifugal potential create the potential of the system, known as the Roche geometry. Close to a star the equipotential surface are spherical and material is bound to the star. Further out, the influence of its companion distorts the shape of its surfaces. The largest closed equipotential surface of each star is known as its Roche lobe. The lines of Roche equipotential depend only upon the mass ratio with the scale being set by the orbital separation (Warner, 1995).

2.1.1 Classification of close binaries

Classification of binary stars is very important because it strongly influences both the evolution and observed appearance of the system. The shapes of stars in a binary system depend solely on the value of potentials (Kopal, 1959). Close binaries are classified into three distinct groups.

2.1.1.1 Detached binaries

Detached binaries are systems in which both stars are bound within separate equipotential surfaces as seen in Figure 2.1. The stars have no major effect on each other and essentially evolve separately. Most binaries are belonged to this class. Their evolution is more or less independent from one another, that is

why detached binaries may be used as ideal physical laboratories for studying the properties of individual stars.

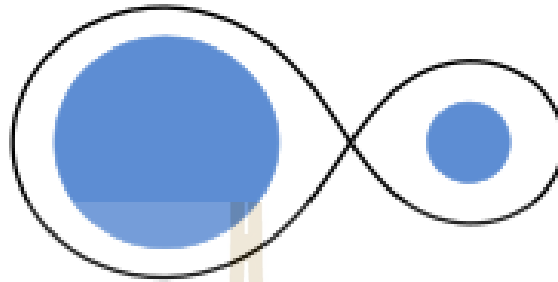


Figure 2.1 Detached binary, two main-sequence stars, the blue area represents the surface, (from https://en.wikipedia.org/wiki/Binary_star).

2.1.1.2 Semidetached binaries

Semi-detached binaries are systems in which one star become a red giant and fills its Roche lobe and the other is bound within a separate equipotential surface as shown in Figure 2.2. They frequently exhibit mass transfer, magnetic coupling of both stars and circumstellar clouds.

The larger star surface is closer to the companion star. If this occurs, the red giant overflows its Roche lobe; the mass will be lost from the red giant and accreted onto the secondary. The mass transfer dominates the evolution of the system.

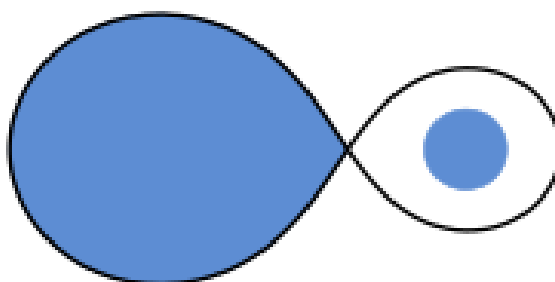


Figure 2.2 Semi-detached binary star, the blue area represents the surface, a massive star is close to filling its Roche lobe, (from https://en.wikipedia.org/wiki/Binary_star).

2.1.1.3 Contact binaries

Contact binaries are systems in which both stars overflow the Roche lobe and share a common envelope shown in Figure 2.3. They may or may not be in a thermal equilibrium. The uppermost part of the stellar atmospheres forms a common envelope that surrounds both stars. As the friction of the envelope brakes the orbital motion, the stars may eventually merge.

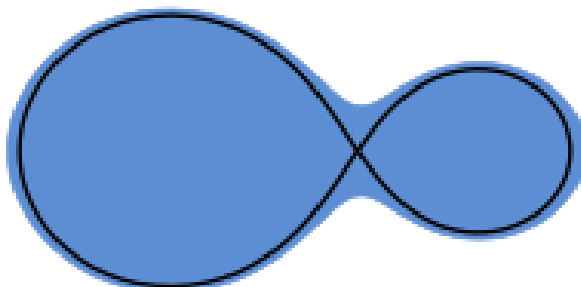


Figure 2.3 Contact binary star, the blue area represents the surface; two stars are filling its Roche lobe already, (from https://en.wikipedia.org/wiki/Binary_star).

2.1.2 Orbital properties of close binaries

In a binary system, where a white dwarf primary and a main sequence companion, with masses M_{WD} and M_{MS} , respectively, orbit with an orbital period P_{orb} around their common center of mass at a separation $a = a_{WD} + a_{MS}$ where a_{WD} and a_{MS} are the distance of white dwarf and main-sequence from their common center of mass and $M_{WD} a_{WD} = M_{MS} a_{MS}$, the orbital velocity K of both star, as observed at an inclination i , is the angle between the orbital plane and plane of sky.

$$K_{WD} = \frac{2\pi a_{WD}}{P_{orb}} \sin i, \quad K_{MS} = \frac{2\pi a_{MS}}{P_{orb}} \sin i \quad (2.1)$$

The orbital inclination, i , measures the tilt of an object's orbit around a celestial body. It is expressed as the angle between a reference plane and the orbital plane or axis of direction of the orbiting object ($0^\circ \leq i \leq 90^\circ$).

Assuming circular orbits, given Kepler's law, the gravitational constant, $G = 6.674 \times 10^{-11} \text{N m}^2/\text{kg}^2$.

$$a^3 = \frac{G(M_{WD} + M_{MS})P_{orb}^2}{4\pi^2} \quad (2.2)$$

And

$$a = a_{WD} \frac{M_{WD} + M_{MS}}{M_{MS}} \quad (2.3)$$

We can obtain the mass functions of main-sequence and white dwarf as followed:

$$f(M_{MS}) = \frac{(M_{MS} \sin i)^3}{(M_{WD} + M_{MS})^2} = \frac{P_{orb} K_{WD}^3}{2\pi G},$$

$$f(M_{WD}) = \frac{(M_{WD} \sin i)^3}{(M_{WD} + M_{MS})^2} = \frac{P_{orb} K_{MS}^3}{2\pi G}, \quad (2.4)$$

From the result of Equation (2.4), we can obtain the mass ratio as:

$$q = \frac{M_{MS}}{M_{WD}} = \frac{K_{WD}}{K_{MS}} \quad (2.5)$$

In this study, since we do not have a value of the white dwarf radial velocity, K_{WD} , an indirect method is needed by rearranging Equation (2.4) for $\sin i$ and we get

$$\sin i = \left[\frac{P_{orb} K_{MS}^3 (M_{WD} + M_{MS})^2}{P_{orb} M_{MS}^3} \right]^{1/3} \quad (2.6)$$

And we substitute $\sin i$ into Equation 2.1, then we can obtain.

$$K_{MS} = \left[\frac{2\pi G \sin^3 i^3 M_{WD}^3}{P_{orb} (M_{WD} + M_{MS})^2} \right]^{1/3} \quad (2.7)$$

2.2 Roche geometry

The region of space around a star in a binary system in which orbiting material is gravitationally bound to the star called Roche lobe. If the star fills its Roche lobe, then the material will flow onto its companion star. Where follows the motion of a massless test particle in the gravitational field of two orbiting masses M_1 and M_2 , considering the restricted three-body problem, this assume that the orbit is circular. The angular velocity, ω of the orbit from Kepler's third law can be written as

$$\omega^2 = \left[\frac{G(M_1 + M_2)}{a^3} \right] \quad (2.8)$$

We choose a Cartesian coordinate system (x, y, z) with origin at the center of mass and which rotate with angular speed ω about the Z-axis. Without loss of generality we may then place masses M_1 and M_2 on the X-axis with coordinates

$$X_{M_1} = -\frac{M_2}{M_1 + M_2} a, \quad X_{M_2} = +\frac{M_1}{M_1 + M_2} a, \quad (2.9)$$

The effective gravitational potential in the rotating frame of reference, including the centrifugal potential, then reads at an arbitrary point (x, y, z)

$$\Psi = -\frac{GM_1}{r_1} - \frac{GM_2}{r_{21}} - \frac{1}{2} \omega^2 \rho'^2 \quad (2.10)$$

$$\Psi = -\frac{GM_1}{[(X-X_{M_1})^2+Y^2+Z^2]^{1/2}} - \frac{GM_2}{[(X-X_{M_2})^2+Y^2+Z^2]^{1/2}} - \frac{1}{2}\omega^2(X^2 + Y^2) \quad (2.11)$$

Close to each stellar center the equipotential surfaces are approximately spherical and concentric with the nearer star. Far from the stellar system, the equipotential are approximately ellipsoidal and elongated parallel to the axis connection the stellar centers. A critical equipotential intersects itself at the center of mass of the system. It is this equipotential which defines the Roche lobes, shown in Figure 2.4.

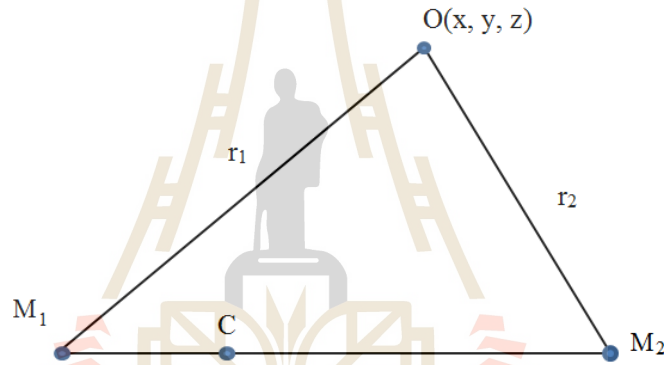


Figure 2.4 The two masses M_1 and M_2 , C is common center of mass, are separated by unit distance. The point $O(x, y, z)$ is at a distance r_1 from M_1 and r_2 from M_2 . The coordinate system is originated at the mass M_1 .

The gravity potential, Ψ experienced at the position $O(x, y, z)$ is the sum of two point masses potentials and the rotational potential, If we find shapes corresponding to constant Ψ , then we have found the possible shapes of the stars of a binary system.

$$\Psi = -\frac{GM_1}{r_1} - \frac{GM_2}{r_2} - \frac{\omega^2}{2} \left[\left(x - \frac{M_2}{(M_1+M_2)} \right)^2 + y^2 \right] \quad (2.12)$$

$$\omega^2 = \left(\frac{2\pi}{P} \right)^2 = \frac{G(M_1+M_2)}{R^3} \quad (2.13)$$

If we define the values $\Psi_n = -2\Psi/G(M_1 + M_2)$ and the mass ratio, $q = M_2/M_1$ ($0 < q \leq 1$), then

$$\Psi_n = \frac{2}{(1+q)r_1} + \frac{2q}{(1+q)r_2} + \left(x - \frac{q}{(1+q)}\right)^2 + y^2 \quad (2.14)$$

The quantity Ψ_n is a normalized potential, and it can be calculated for any location (x, y, z) around the two mass points. Hence, the surface of constant potential or the equipotential surface within the rotation frame can be found in term of the separation in the unit of distance which depends on the mass ratio, q . In Figure 2.5 the potential contour lines of two mass points M_1 and M_2 with the mass ratio of 0.4 are shown (Hilditch, 2001).

The coordinates of the small element can be expressed in Cartesian coordinate which related to spherical coordinate as following,

$$x = r \sin \theta \cos \phi$$

$$y = r \sin \theta \sin \phi$$

$$z = r \cos \theta$$

$$\rho = r \sin \theta = \sqrt{x^2 + y^2} \quad (2.15)$$

The center of mass lies on the x-axis and its distance from M_1 is

$$\bar{x} = \frac{\sum m_i x_i}{\sum m} = \frac{M_2 R}{M_1 + M_2} = \frac{q}{(1+q)} R \quad (2.16)$$

Where mass ratio $q = M_2/M_1$

Now we can find r_1 , r_2 and ρ' in terms of the coordinates relative to our origin in the center of M_1

$$r_1 = r$$

$$r_2 = \sqrt{(x - R)^2 + y^2 + z^2} = \sqrt{r^2 - 2xR + R^2}$$

$$\rho' = \sqrt{(x - \bar{x})^2 + y^2} = \sqrt{\rho^2 - 2\bar{x}x + \bar{x}^2} \quad (2.17)$$

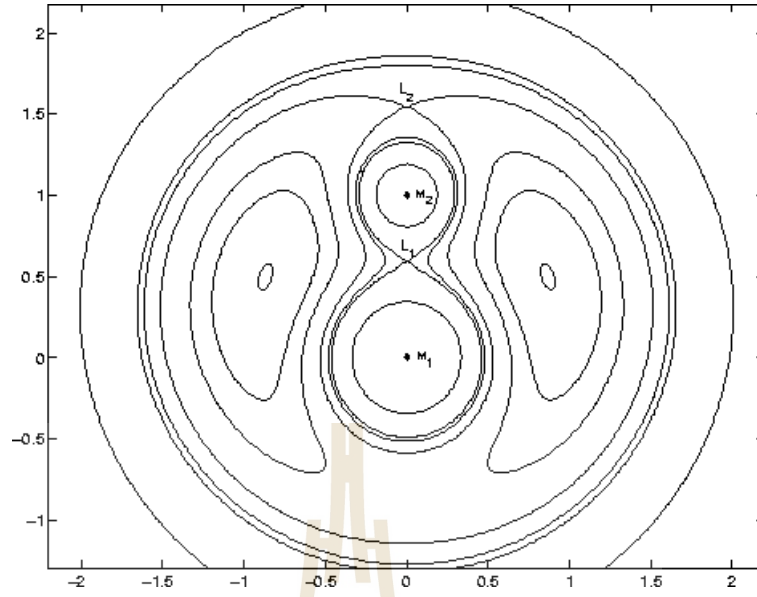


Figure 2.5 The cross-section in orbital Ψ_n for a binary system with mass ratio 0.4, the center of mass is at Lagrange L_1 and L_2 is lined on the line equipotential position opposite L_1 of M_2 , equipotential in the same contour line.

Substitutes Equations (2.10), (2.15), and (2.17), then we get,

$$\Psi(r, \theta, \phi) = -\frac{GM_1}{r} - \frac{GM_2}{\sqrt{r^2 - 2rR \sin \theta \cos \phi + R^2}} - \frac{1}{2} \omega^2 (\rho^2 - 2\bar{x}r \sin \theta \cos \phi + \bar{x}^2). \quad (2.18)$$

From Kepler's third law, if we replace ω^2 and change $\lambda = \sin \theta \cos \phi$, $\mu = \sin \theta \sin \phi$, and $\nu = \cos \theta$. Using Equation (2.13), (2.16) and (2.18) then we have

$$\Psi(r, \lambda, \nu) = -\frac{GM_1}{R} \left[\frac{R}{r} + q \left(\frac{R}{\sqrt{r^2 - 2rR\lambda + R^2}} - \frac{r\lambda}{R} \right) + \frac{1}{2} (1+q) \frac{r^2}{R^2} (1-\nu^2) + \frac{1}{2} \frac{q^2}{(1+q)} \right] \quad (2.19)$$

From *Kopal* (1959), a new potential function was define as

$$\Omega = -\frac{R\Psi}{GM_1} - \frac{1}{2} \frac{q^2}{1+q} \quad (2.20)$$

We also notice that r can be expressed as a fraction of R which is the separation between two stars in the unit less term

$$\tilde{r} = \frac{r}{R} \quad (2.21)$$

Using Equations (2.19), (2.20), and (2.21) we get

$$\Omega = \frac{R\Psi}{GM_1} - \frac{1}{2} \frac{q^2}{(1+q)} = \frac{1}{\tilde{r}} + q \left(\frac{1}{\sqrt{\tilde{r}^2 - 2\tilde{r}\lambda + 1}} - \tilde{r}\lambda \right) + \frac{1}{2}(1+q)(1-\nu^2)\tilde{r}^2 \quad (2.22)$$

At the pole of M_1 , $\theta = 0$, $\lambda = 0$, $\nu = 1$, then we can obtain

$$\Omega = \frac{1}{\tilde{r}_{pole}} + q \left[\frac{1}{\sqrt{\tilde{r}_{pole}^2 + 1}} \right] = \text{constant}. \quad (2.23)$$

And at any position we can also obtain in a function of Ω as

$$\tilde{r} = \frac{1}{\left(\Omega - \frac{q}{\sqrt{\tilde{r}^2 - 2\tilde{r}\sin\theta \cos\phi + 1}} + q\tilde{r}\sin\theta \cos\phi - \frac{1}{2}(1+q)(1-\cos\theta^2)\tilde{r}^2 \right)} \quad (2.24)$$

There is clearly not a simple analytical solution of \tilde{r} as a function of θ and ϕ . However, there are ways that we can obtain the values of \tilde{r} to an arbitrary accuracy by setting.

$$\Omega = \frac{1}{\tilde{r}} + q \left[\frac{1}{\sqrt{\tilde{r}^2 - 2\tilde{r}\lambda + 1}} - \tilde{r}\lambda \right] + \frac{1}{2}(1+q)(1-\nu^2)\tilde{r}^2 \quad (2.25)$$

Because Ω is constant then we get

$$\Omega = \frac{1}{\tilde{r}_{pole}} + q \left[\frac{1}{\sqrt{\tilde{r}_{pole}^2 + 1}} \right] = \frac{1}{\tilde{r}} + q \left[\frac{1}{\sqrt{\tilde{r}^2 - 2\tilde{r}\lambda + 1}} - \tilde{r}\lambda \right] + \frac{1}{2}(1+q)(1-\nu^2)\tilde{r}^2 \quad (2.26)$$

From Equation 2.22, we can apply the Newton-Raphson method to obtain \tilde{r} as a function of θ and ϕ . Where the polynomial of Newton-Raphson method can be written as

$$f(r) = \frac{\tilde{r}}{\tilde{r}_{pole}} + q \left[\frac{\tilde{r}}{\sqrt{\tilde{r}_{pole}^2 + 1}} \right] - q \left[\frac{\tilde{r}}{\sqrt{\tilde{r}^2 - 2\tilde{r}\lambda + 1}} - \tilde{r}^2\lambda \right] + \frac{1}{2}(1+q)(1-\nu^2)\tilde{r}^3 - 1 = 0 \quad (2.27)$$

For an initial of the root's position, Newton-Raphson algorithm can be applied iteratively to obtain an improved value \tilde{r}_{n+1} from \tilde{r}_n as follows

$$\tilde{r}_{n+1} = \tilde{r}_n - \frac{f(\tilde{r}_n)}{f'(\tilde{r}_n)} \quad (2.28)$$

Where

$$f'(r) = \frac{\tilde{r}}{\tilde{r}_{pole}} + q \left[\frac{1}{\sqrt{\tilde{r}_{pole}^2 + 1}} \right] - q \left[\frac{1}{\sqrt{\tilde{r}^2 - 2\tilde{r}\lambda + 1}} - \tilde{r}(\tilde{r} - \lambda)(\tilde{r}^2 - 2\tilde{r}\lambda + 1)^{-\frac{3}{2}} - 2\tilde{r}\lambda \right] + \frac{3}{2}(1+q)(1-\nu^2)\tilde{r}^2 = 0 \quad (2.29)$$

which gives us

$$r_{n+1} = r_n - \frac{\frac{\tilde{r}_n}{\tilde{r}_{pole}} + q \left[\frac{\tilde{r}_n}{\sqrt{\tilde{r}_{pole}^2 + 1}} \right] - q \left[\frac{\tilde{r}_n}{\sqrt{\tilde{r}_n^2 - 2\tilde{r}_n\lambda + 1}} - \tilde{r}_n^2\lambda \right] + \frac{1}{2}(1+q)(1-\nu^2)\tilde{r}_n^3 - 1}{\frac{1}{\tilde{r}_{pole}} + q \left[\frac{1}{\sqrt{\tilde{r}_{pole}^2 + 1}} \right] - q \left[\frac{1}{\sqrt{\tilde{r}_n^2 - 2\tilde{r}_n\lambda + 1}} - \tilde{r}_n(\tilde{r}_n - \lambda)(\tilde{r}_n^2 - 2\tilde{r}_n\lambda + 1)^{-\frac{3}{2}} - 2\tilde{r}_n\lambda \right] + \frac{3}{2}(1+q)(1-\nu^2)\tilde{r}_n^2} \quad (2.30)$$

2.3 Lagrangian points

Lagrangian points are those points in a rotating two-body system where the net force exerted on a particle mass is 0. There are 5 such points, shown on Figure 2.6, L_1 , L_2 and L_3 are located on the x-axis and are always unstable; L_4 and L_5 are displaced in $\pm y$ -direction and may be either stable or unstable, depending on the mass ratio of the binary. These points are obtained by demanding that a gradient of Equation 2.23 is 0. There are five equilibrium points to be found in the vicinity of two orbiting masses. The Roche lobe is thus the limiting equipotential surface that

distinguishes between different morphologies of close binary stars, shown in Figure 2.7.

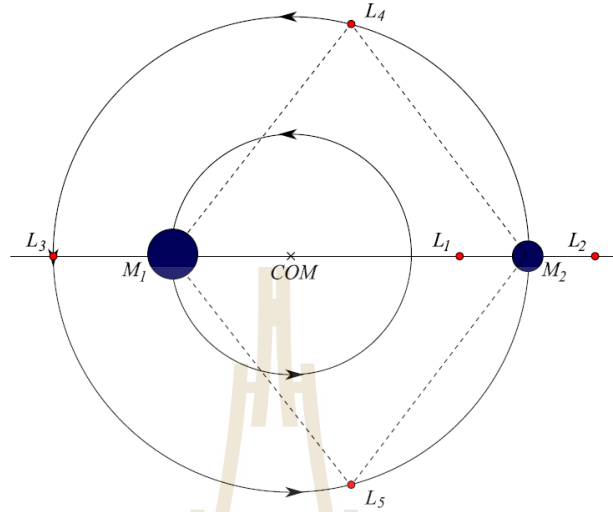


Figure 2.6 Lagrangian points in a rotating of two-body system. The three points (L_1 , L_2 and L_3) lie on the straight line that passes through the center of the two stars, COM is the center of mass of this system. The two points L_4 and L_5 form equilateral triangles with the two stars, the angle are 60 degree (Prsa, 2010).

Form equilaterals triangles with the centers of M_1 and M_2 . To locate the other three Lagrange points we can again use Equation (2.25)

For L_1 , $\theta = 90^\circ$, $\phi = 0^\circ$, so $\nu = 0$ and $\lambda = 1$. So along the positive x-axis,

$$\Omega_{x+} = \frac{1}{\tilde{r}_n} + q \frac{1}{\sqrt{\tilde{r}_n^2 - 2\tilde{r}_n + 1}} - q\tilde{r}_n + \frac{1}{2}(1 + q)\tilde{r}_n^2 \quad (2.31)$$

To find the position of L_1 , we set the first derivative of this function equal to zero

$$g(\tilde{r}) = \frac{d\Omega_{x+}}{d\tilde{r}} = \frac{1}{\tilde{r}^2} + q \left(\frac{\tilde{r}-1}{(\sqrt{\tilde{r}^2 - 2\tilde{r} + 1})^{\frac{3}{2}}} + 1 \right) - (1 + q)\tilde{r}^2 = 0 \quad (2.32)$$

We can employ the Newton Raphson method to find the solution to this polynomial

$$\tilde{r}_{n+1} = \tilde{r}_n - \frac{g(\tilde{r}_n)}{g'(\tilde{r}_n)} \quad (2.33)$$

$$g'(\tilde{r}) = \frac{d^2\Omega_{x+}}{d\tilde{r}^2} = \frac{2}{\tilde{r}^3} + \frac{2q}{(\tilde{r}^2 - 2\tilde{r} + 1)^{\frac{3}{2}}} - (1 + q) = 0 \quad (2.34)$$

The L_1 point is located at the line between two large masses of M_1 and M_2 . It is the most intuitively understood of the Lagrangian points: the one where the gravitational attraction of M_2 partially cancels M_1 gravitational attraction

The L_2 point is located on the line which behind the mass of M_2 . Here, the gravitational forces of the two large masses balance the centrifugal effect on a body at L_2 .

In similarly, the L_3 point is located on the line which opposite the Lagrange point L_2 .

For L_3 , $\theta = 90^\circ$, $\phi = 180^\circ$, so $v = 0$ and $\lambda = -1$. The functions to be used in the Newton-Raphson method for L_3 are then

$$\Omega_{x-} = \frac{1}{\tilde{r}_n} + q \frac{1}{\sqrt{\tilde{r}_n^2 - 2\tilde{r}_n + 1}} + q\tilde{r}_n + \frac{1}{2}(1 + q)\tilde{r}_n^2 \quad (2.35)$$

$$g(\tilde{r}) = \frac{d\Omega_{x-}}{d\tilde{r}} = \frac{1}{\tilde{r}^2} - q \left(\frac{\tilde{r} + 1}{(\sqrt{\tilde{r}^2 + 2\tilde{r} + 1})^{\frac{3}{2}}} - 1 \right) + (1 + q)\tilde{r}^2 = 0 \quad (2.36)$$

$$g'(\tilde{r}) = \frac{d^2\Omega_{x-}}{d\tilde{r}^2} = \frac{2}{\tilde{r}^3} + \frac{2q}{(\tilde{r}^2 + 2\tilde{r} + 1)^{\frac{3}{2}}} + (1 + q) \quad (2.37)$$

The parallel component of the force is disappear leading to the condition that the equilibrium points are a distance R from each mass. The L_4 and L_5 points are located on the orbital line of M_2 . The Lagrange of L_4 and L_5 can be written as

$$L_4 = \left(\frac{R}{2} \left(\frac{M_1 - M_2}{M_1 + M_2} \right), \frac{\sqrt{3}}{2} R \right) \text{ or } \left(\frac{R}{2}, \sin(60^\circ) R \right) \quad (2.38)$$

$$L_5 = \left(\frac{R}{2} \left(\frac{M_1 - M_2}{M_1 + M_2} \right), -\frac{\sqrt{3}}{2} R \right) \text{ or } \left(\frac{R}{2}, -\sin(60^\circ) R \right) \quad (2.39)$$

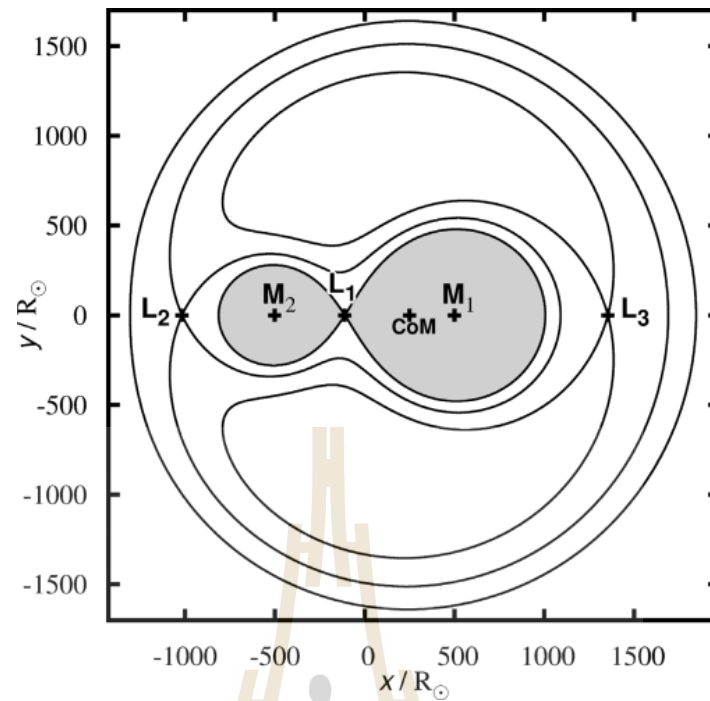


Figure 2.7 The contact point of the Roche lobe, component masses $M_1 = M_\odot$ and $M_2 = 1/3M_\odot$ and scale in x, y orbital plane of a binary system with separation $1000R_\odot$. The primary star (M_1) fill its Roche lobe; it transfers material to the companion star through the inner Lagrange point 1. The secondary star, M_2 cannot accept the material and also fills its Roche lobe (Roche lobe fill in gray) L_2 and L_3 are the Lagrangian points and CoM is the center of mass of the binary system (Izzard et al., 2011).

2.4 Trojans

Trojans are asteroids or some of material that share an orbit near stable points in front of or behind the star or planet. Such as in our Solar system, trojans also share orbits with Neptune, Mars and Jupiter. They derive their names from the trojan asteroids in the Sun-Jupiter system. Trojan asteroids orbit around the sun in Jupiter's orbit at its Lagrangian equilibrium points L_4 and L_5 , where they are phase-locked and protected from collision with each other, shown in Figure 2.8 (Carroll and Ostlie, 1996). When two bodies are much more massive than the third, the smaller object can be locked into an orbit such that the three objects always form an equilateral triangle as seen in Figure 2.8.

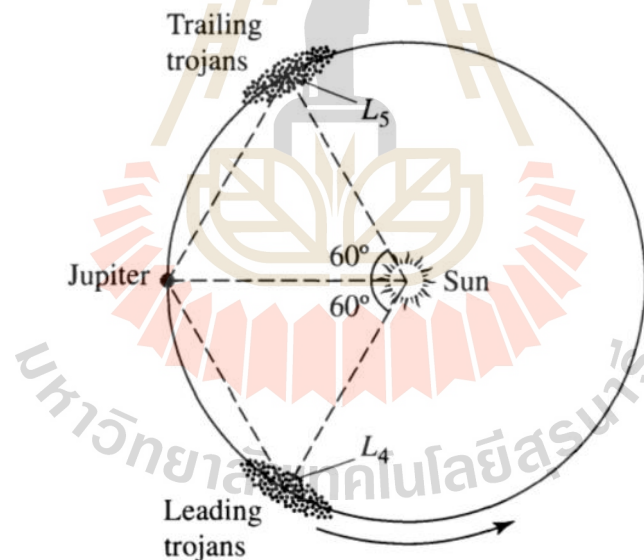


Figure 2.8 The Trojan asteroids in the Sun-Jupiter system, they are located in Jupiter's orbit, trailing the planet by angle 60 degree. The occupied positions are two of the five Lagrangian points in the Sun-Jupiter system (Carroll and Ostlie, 1996).

2.5 Common envelope evolution

2.5.1 The formation of the common envelope

Main-sequence binaries are considered to be the progenitors of close compact binaries. Population synthesis model predict that about 25% of the main sequence binary population suffer mass transfer interactions (Williems and Kob, 2004). The stellar components of remaining about 75% population evolve as if they were single stars. Even though the majority of interacting binaries are expected to undergo a common envelope (CE) phase and become close compact binaries, the details of their evolution crucially depends on the conditions of mass transfer, and consequently on the initial masses of both stars.

2.5.2 The common envelope phase

A CE is gas that contains a binary star system. The gas does not rotate at the same rate as the embedded binary system. A system with such a configuration is called CE phase or undergoing CE evolution. A star appears as a single point of light to an observer but based on its brightness variation and spectroscopic observation we may be able to say that the single point of light is actually two stars in close orbit around one another. The variations in light intensity from eclipsing binary stars are caused by one star passing in front of the other relative to an observer.

The eclipsing binary is initially consisting of two main sequence stars in which a more massive star evolved through the giant phase and fills its Roche Lobe. It typically involves the spiral in of a companion star inside the envelope of a giant donor star and, in many cases, the ejection of the envelope, transforming an initially binary into a very close binary (Paczýnski, 1976). When the mass-losing star envelope expands more rapidly than the radius of its Roche lobe, leading to an

unstable mass transfer then the secondary star will fall into the envelope of the primary where the two stars share a CE phase. The evolution of an eclipsing binary system is described in Figure 2.9.

The system can lose significant amounts of mass, due to the movement of the secondary inside the primary's envelope, which will reduce the angular momentum, the orbital radius and the period. After the greater mass has degenerated into a white dwarf, the companion or secondary star later evolves into a main-sequence and the stage is set for mass accretion onto the white dwarf primary star. During this final shared-envelope phase, the two stars spiral in closer together as the angular momentum is lost. The resulting orbit can have a period as short as a few hours, known as the post common envelope binary (PCEB). The resulting systems are white dwarf plus main-sequence (WDMS) systems.

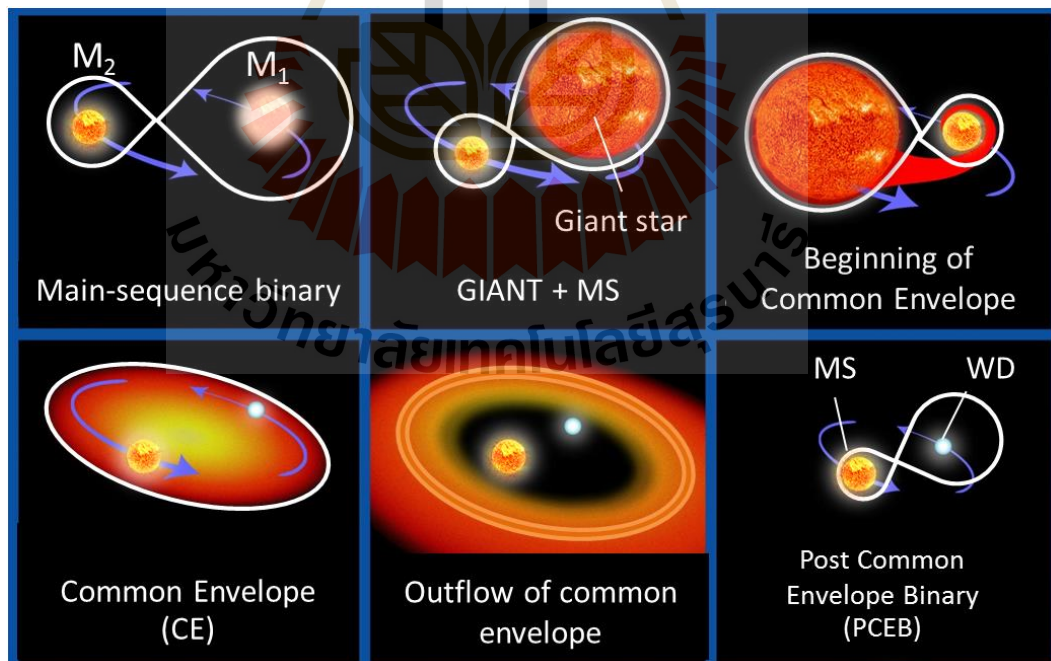


Figure 2.9 The evolution of post-common envelope binary (PCEB) chart. Two normal stars are in binary pairs or main-sequence binary and M_1 have more massive

than M_2 , the more massive star becomes a giant star and where the leakage of gas on the secondary star caused the expansion and became encompassing. Light-weight stars and the core of the giant star are within the envelope or common envelope (CE). Envelopes will be removed as the separation between the core and the secondary stars will be reduced, it means outflow of a common envelope. And then the remaining core of the giant collapses and become a white dwarf, the main-sequence and white dwarf binary system is called post-common envelope binary (taken from http://en.wikipedia.org/wiki/Supernova#mediaviewer/File:Progenitor_IA_supernova.svg).

2.6 White dwarf

A white dwarf, also called a degenerate dwarf, is a stellar remnant composed mostly of electron-degenerate matter. A white dwarf is very dense. Its mass is comparable to that of the Sun, while its volume is comparable to that of Earth. A white dwarf luminosity comes from the emission of stored thermal energy (no fusion takes place in a white dwarf).

2.7 M-type star

The M-type star or red dwarf is a small and relatively cool star on the main sequence, either late K or M spectral type. Red dwarfs range in mass from $0.075M_{\odot}$ to about $0.50M_{\odot}$ and have a surface temperature of less than 4000K. Therefore, red dwarfs develop very slowly and have a constant luminosity, until their fuel is depleted. Because of the comparatively short age of the universe, no red dwarfs of advanced evolutionary stages exist.

Of all the stars, flares are most frequently observed on a certain class of M-type stars. The stellar activity is depend on (I) Later stars are more active because they have a larger convection zone. (II) Fast rotators are more active. (III) Younger stars are more active, a possible simple explanation is because they are rotating faster. Ultimately, the magnetic field is responsible for activity (Mitra-Kraev, 2007).

2.8 Mass ejection

The M-type stars, magnetic fields start in the convective zone inside the star, where ionized gas or plasma rises toward the surface. The magnetic fields are created by moving charged particles in these columns of plasma. Unlike our Sun which the convection zone is only a small fraction of the star's radius, but the M-type stars are entirely convective from their cores to their surface. Together with the star's rotation, allows magnetic fields to strongly build up and become huge. When these cells magnetized plasma reaches the surface they can tangle up, and prevent the cooling gas from sinking again. The gas cools and becomes what we call a spot. So far, there was only two evidence of mass ejection that has been observed in QS Virginis and V471 Tauri.

2.9 Time scale for periodic of eclipses

Due to the finite speed of light, as the Earth travels in its orbit, measuring times from observations concerning other targets outside our Solar system has to be approached with caution. The Light from a particular object may be early or delayed by as much as 8.3 minutes ($1 \text{ AU}/c$), c is speed of light. The exact time that a certain event is observed, depends on the changing position of the observer in the Solar

system as well as the particular clock used to express the time. To be able to compare observations from different epochs, the observed time can be converted to a number of time stamps. The Modified Julian Date (*MJD*) starts counting at midnight 17 November 1858, so that is related to the Julian date (*JD*) as

$$MJD = JD - 2400000.5, \quad (2.40)$$

and *JD* is the Julian Date to adjust to the reference frame of the Sun, rather than using the variable reference of Earth, one can also use Heliocentric Julian Date (*HJD*). The solution to this problem is to calculate the time the light from a given object would have arrived at a non-accelerating reference frame. Generally, we have used the *HJD*, referenced to the center of the Sun because it is easy to compute. To be even more precise, one can correct for the motion of the Sun around the barycenter of the Solar system, which introduces errors as large as 8 seconds, and use Barycentric Julian Dates (*BJD*), both of these latter two can be expressed with respect to the more recent zero point, to obtain *HMJD* and *BMJD* (Eastman et al., 2010).

Another important aspect about time stamping is the time standard used, which refers to the way particular clock ticks. As a time standard Coordinated Universal Time (*UTC*) is most commonly used (Bours, 2015). However, this time system includes leap seconds, which accumulate over the years, lead to jumps in the time scale, so it can make time comparisons to complicate. When heliocentric and barycentric reference frames are used, a higher precision is often required (Eastman et al., 2010). There are several alternatives to *UTC*, including, in order increasing accuracy of time, International Atomic Time (*TAI*), Terrestrial Time (*TT*) and Barycentric Dynamical Time (*TDB*). *TAI* runs at nearly the same rate as *UTC*, but does not include leap seconds, *N*, now until June 2015, $N = 35 \text{ seconds}$.

$$UTC = TAI - (\text{number of leap seconds}, N) \quad (2.41)$$

International Atomic Time, *TAI*:

$$TAI = UTC + N \quad (2.42)$$

when the next leap second will be introduced. TT includes an offset from TAI, which was introduced to retain continuity with its predecessor Ephemeris Time, so that

$$TT = TAI + 32.184 \text{ seconds}, \quad (2.43)$$

TDB is a relativistic time standard in the reference frame of the Solar system barycenter, and is the same as *TT* relativistic for time dilation and gravitational redshift caused by bodies in the solar system. *TDB* is different from *TT* by at most 3.4 *ms*, as the following

$$TDB - TT = 0.001658 \sin(M_A) + 0.000014 \sin(2M_A) \quad (2.44)$$

where the epoch is expressed in terms of *TT*, with an equivalent *JD*. One of the basics is independent of any particular coordinate system: M_A is mean anomaly (degree). The standard epoch in use today is Julian epoch on 2000 Jan 1.5 (start at 12^h on January 1) in term of *TT*, it is $JD_0 = 2451545.0$.

Where T is the time of number Julian centuries since 1st January, 2000.0, 12 *UT*, form of the Julian century, notices 36,525 days in one Julian century (Meeus, 1998).

$$T = (JD - 2451545.0) / 365.25 \quad (2.45)$$

Mean anomaly is an angle used in calculating the position of a body in an elliptical orbit in the two-body problem of classical. This is the angular distance from the pericenter. The pericenter is a mean point of closest approach of an astronomical object in an elliptical orbit to its center of attraction. A fictitious body would have if

mean anomaly moved in a circular orbit, with constant speed, in the same orbital period as the actual body in its elliptical orbit. Which we can be written as

$$M_A = 357.52910 + 35999.05030 * T - 0.0001559 * T^2 - 0.00000048 * T^3 \quad (2.46)$$

If we replace T from Equation 2.38, then we get

$$M_A = 357.52910 + 0.9856003(JD - 2451545.0) \quad (2.47)$$

2.10 Ephemeris parameters and O-C diagram

Orbital phase is a fraction of the orbital period that has passed since the last completed revolution cycle. It changes linearly in time on the (0, 1) interval and is connected to the mean anomaly by the following relation. Phase 0 is the center of the ellipse on the orbital plane and the ellipse itself. Phase 0 is the conjunction phase when the argument of periastron is phase 0.5.

The primary star is the one at superior conjunction near orbital phase 0. It will be the one eclipsed near orbital phase 0 if there are eclipses. Secondary star is the one at inferior conjunction near orbital phase 0. It will be the one eclipsing near orbital phase 0 if there are eclipses.

Following photometric measurements given a function of time constitute a photometric light curve. Checking light curves reveal variability of the source, be it intrinsic or aspect-dependent. If variability is periodic, it is customary to fold the observed data to the phase interval (0, 1):

$$Epoch = \left[\frac{T_{now} - T_0}{P_{orb}} \right] \quad (2.48)$$

Where *Epoch* (E) is a number of period cycle and P_{orb} is the orbital period of the binary. T_{now} is a current primary eclipse time and T_0 is a reference time or ephemeris. The time that we use is in Barycentric Julian date (BJD). Because BJD is JD corrected for differences in the Earth's position with respect to the barycenter of the Solar System. Due to the finite speed of light, the time an astronomical event is observed depends on the changing position of the observer in the Solar System. Before multiple observations can be combined, they must be reduced to a common, fixed, reference location. This correction also depends on the direction to the object or event being timed. In 1991, the BJD replaced the HJD , which reduced times to the center of the Sun. The difference between HJD and BJD is up to ± 4 s. Such a transformation constitutes a phased light curve. Zero point, BJD_0 is a unique point in time that sets the origin of the ephemeris. Following to the same convention as the orbital phase, BJD_0 not in general correspond to superior conjunction of the primary star. Orbital period P_{orb} is the sidereal time of revolution of both components in a binary system around the center of mass. Rate of period change, dP/dt is the first time derivative of the orbital period.

$$Period(BJD) = P_{orb} + \frac{dP}{dt}(BJD_{now} - BJD_0) \quad (2.49)$$

$$Phase = \frac{1}{Cycle} \left[\frac{BJD_{now} - BJD_0}{P_{orb} + \frac{dP}{dt}(BJD_{now} - BJD_0)} \right] \quad (2.50)$$

Therefore we can find the time of minimum (Min I) of the mid-eclipse or a peak period from

$$Min I = T_0 + P_{orb} \times E \quad (2.51)$$

We know that variable stars change their brightness over a cycle of the period all the time. The different between the actual timing of the mid eclipse (O) and the

calculated time (C) is called O-C. The O-C diagram is a plot of the observed times of minimum light (O) minus calculated allowing to adopted ephemeris (C) as a function of time. The vertical axis of the O-C diagram most often represent time, usually expressed in days or seconds and the horizontal axis is epoch (cycles of a period). O-C can be obtaining from:

$$O - C = \text{Min } I - (T_0 + P_{orb} \times E), \quad (2.52)$$

O-C diagram is a tool that use for finding a period of stellar variability. The basic mechanisms of the periodic or nearly periodic stellar variability are the rotation of an anisotropically radiating star, the orbital motions of components in stellar systems, and pulsations or oscillations of various kinds.

For a star with no measurable change in the period or in a case of constant period, points on the O-C diagram will scatter about a straight horizontal straight line across the graph. The size of the scatter is an indication of the accuracy of the observed times of maximum.

2.11 Ellipsoidal variations

The other of important effect due to the stellar surface distortion dependent, called ellipsoidal variation. The ellipsoidal variation is caused by the variation of flux which depends on the shape of star. Since the star oblate due to tidal forces and rotation, we see a large surface cross section when the stars oriented side-ways, hence around quarter phase. On the other hand, we see a smaller surface cross section when we are looking along the semi-major axis, hence around phases 0.0 and 0.5. This effect is referred to as ellipsoidal variation of the light curve (Psra, 2011). Shape distortion of the Roche lobe is filling component star causes the total surface that is

visible to the observer to change with phase. Stellar shapes are shown in phases -0.5 , -0.25 , 0.0 , 0.25 and 0.5 , that correspond to minima and maxima of the light curve.

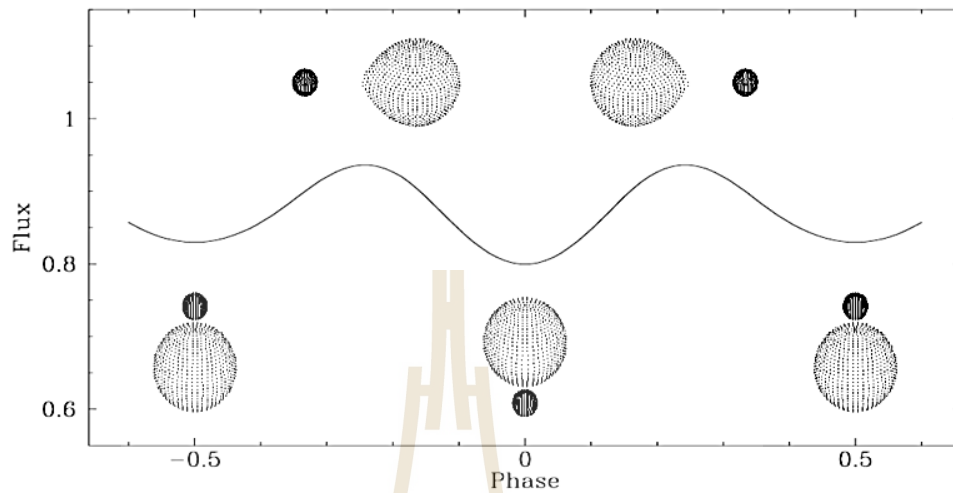


Figure 2.10 Show the light curve variation of a detached binary due to ellipsoidal variations, a position of the ellipsoidal system, at phase 0.0 that is point position, a side at phase 0.25 (or -0.25) and back side at phase 0.5 (or -0.5), (Psra, 2011).



CHAPTER III

METHODOLOGY

In this research of SDSS J1021+1744, we obtained the data from the Thai National Observatory with 2.4-meter telescope and ULTRASPEC. It is located near the summit of the highest point in Chiang Mai, Thailand, at 2,457 meters above sea level. The drive system of the 2.4-meter telescope has been enabled to have automatic control of the dome structure. The data reduction and data analysis have been done using the ULTRASPEC pipeline to obtain light curve for SDSS J1021+1744. JKTEBOP, PHOEBE and Binary Maker 3.0 were used to obtain the binary parameters of this system which we will discuss in the next section.

3.1 Observation

The data of SDSS J1021+1744 had been collected during January 2014 to January 2016. The ULTRASPEC is chosen because it is very sensitive to observe faint objects with larger than 19 magnitudes. ULTRASPEC on the 2.4-meters TNT provides an imaging photometry over a field of view of $7.7' \times 7.7'$ with a pixel scale of 0.45" pixel⁻¹. Zero readout noise is available via the avalanche output. The detector is cooled down with liquid nitrogen, providing almost zero dark currents (Dhillon et al., 2014). The transmission profile of ULTRASPEC SDSS filter is shown in Figure 3.1 and Table 3.1 is shown ULTRASPEC filter with the central wavelength and the full width at half maximum, FWHM (Dhillon et al., 2014).

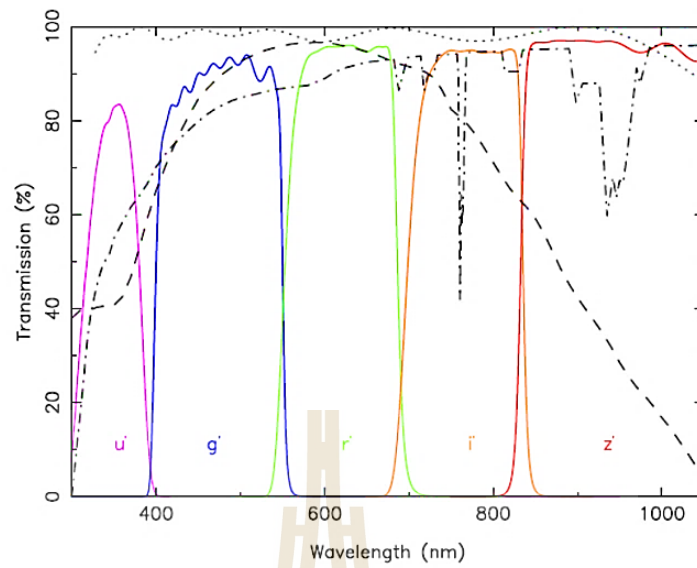


Figure 3.1 The Transmission profile of ULTRASPEC SDSS filter set (purple, blue, green, orange and red solid lines correspond to u' , g' , r' , i' and z' respectively), (Dhillon et al., 2014).

Table 3.1 In our observation, we used ULTRASPEC filters. λ_c is the central wavelength and $\Delta\lambda$ is the FWHM.

| Filter | λ_c (nm) | $\Delta\lambda$ (nm) |
|------------|------------------|----------------------|
| g' | 482.5 | 59.9 |
| r' | 626.1 | 138.2 |
| i' | 767.2 | 153.5 |
| z' | 909.7 | 137.0 |
| Clear | - | - |
| Schott KG5 | 507.5 | 360.5 |
| $i'+z'$ | 838.5 | 290.5 |

Notice, the clear filter is approximately $u'+g'+r'+i'+z'$ and the Schott KG5 filter is approximately $u'+g'+r'$ (Dhillon et al., 2014).

Staralt program was used for the visibility chart of SDSS J0745+2631 in each observation night. An example of object visibility of SDSS J0745+2631 is shown in Figure 3.2. (STARALT from <http://catserver.ing.iac.es/staralt/index.php>).

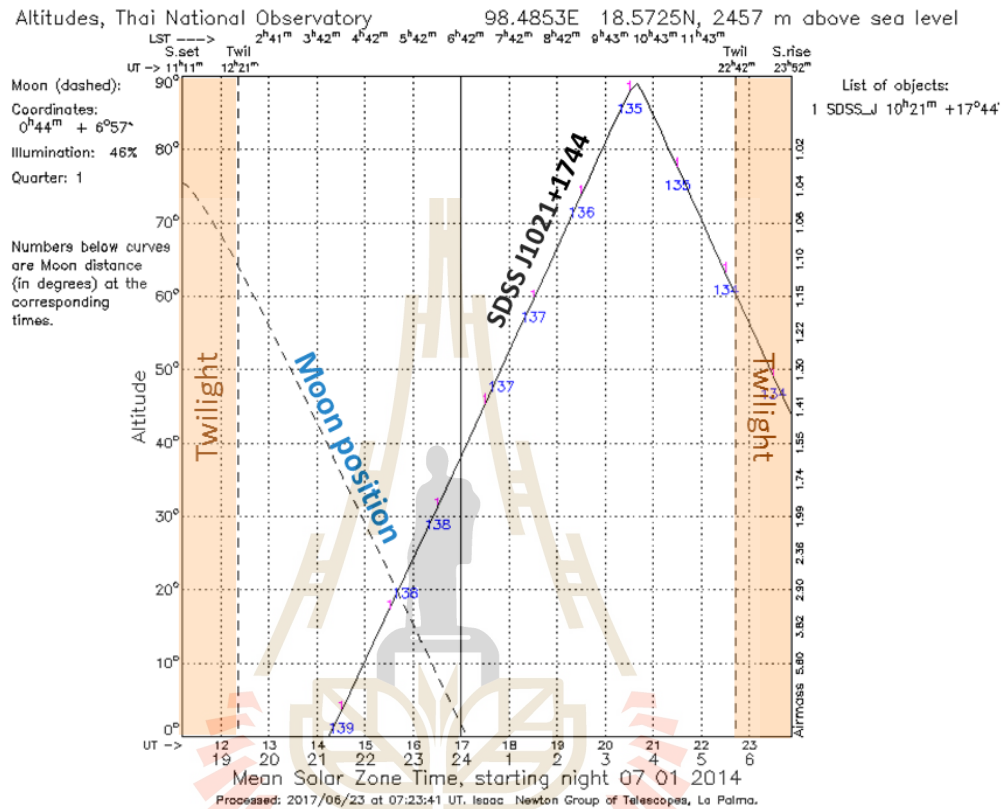


Figure 3.2 The visibility of SDSS J1021+1744 on 7 Jan 2014. Orange bands are the time between evening and morning twilight, blue numbers show the distance from the Moon in degree and the dashed line shows the position of the moon at the corresponding time.

After that we used ULTRASPEC to make a finding chart for planning a reference star and check stars (shown in Figure 3.5) because acquisition tool is designed so that ULTRASPEC observers can plan their observations, select comparison stars and choose suitable window sizes, whilst checking that the

ULTRASPEC frame rate and signal-to-noise ratio in common filters satisfy their requirements.

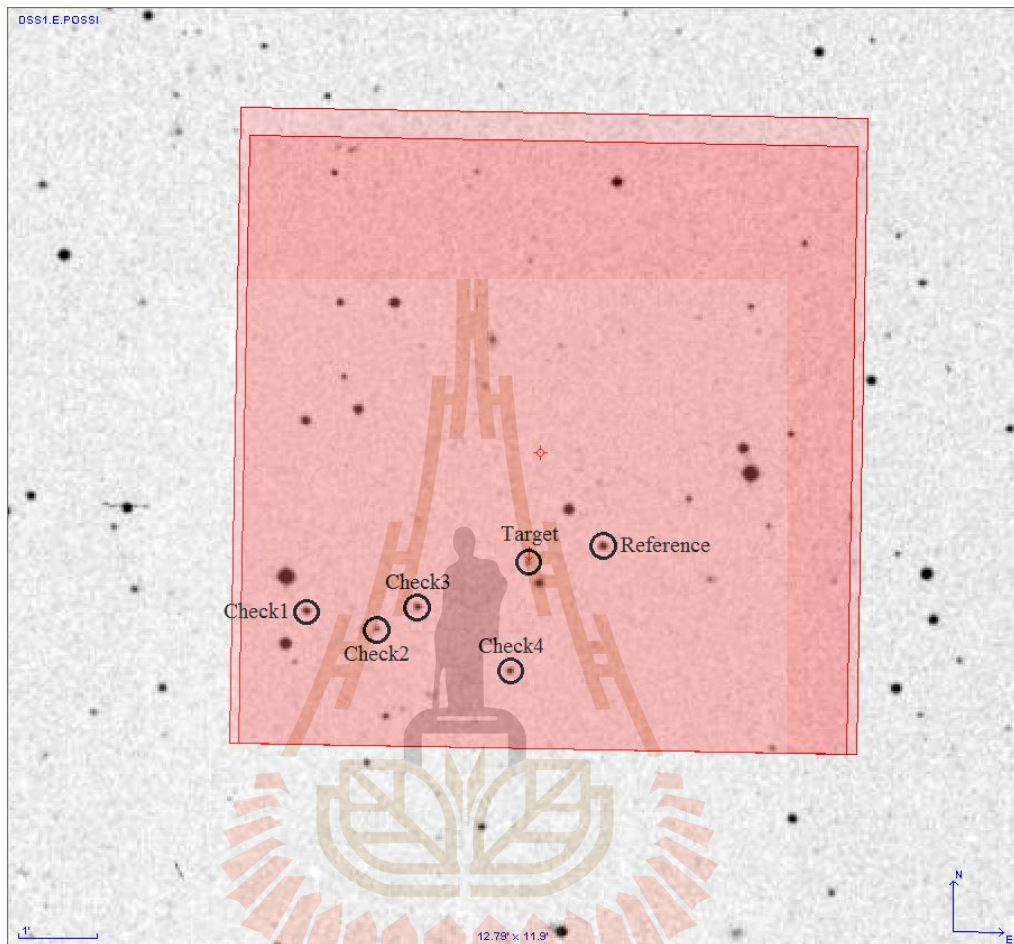


Figure 3.3 ULTRASPEC Finding Chart of target SDSS J1021+1744 (red arrow), reference star and comparisons mark in check1, check2, check3 and check4 stars (in the black circle) from ULTRASPEC Finding Chart, as shown in Table 3.1.

In Figure 3.3, we selected the reference and check star, which must be a non-variable star. In Table 3.2, the data for observation from Aladin Sky Atlas database are presented. And we use several filters for the observation of SDSS J1021+1744 as in Figure 3.1 and the central wavelength and FWHM of each filter are illustrated in Table 3.1.

Table 3.2 Database for observation from Aladin Sky Atlas.

| Label | Proper Names | DEC. | | | |
|-----------|---------------------|--|---------------|--------|--------|
| Stars | SDSS | RA. (J2000) | (J2000) | g mag | r mag |
| Target | J102102.25+174439.9 | 10 ^h 21 ^m 02.25 ^s | +17°44'39.9'' | - | - |
| Reference | J102106.30+174452.2 | 10 ^h 21 ^m 06.30 ^s | +17°44'52.2'' | 16.724 | 16.254 |
| Check 1 | J102050.63+174400.4 | 10 ^h 20 ^m 50.63 ^s | +17°44'00.4'' | 17.070 | 16.668 |
| Check 2 | J102054.42+174347.1 | 10 ^h 20 ^m 54.42 ^s | +17°43'47.1'' | 19.860 | 18.538 |
| Check 3 | J102056.42+174405.5 | 10 ^h 20 ^m 56.42 ^s | +17°44'05.5'' | 18.424 | 17.129 |
| Check 4 | J102101.53+174317.7 | 10 ^h 21 ^m 01.53 ^s | +17°43'17.7'' | 18.666 | 17.303 |

ULTRASPEC flats are normally taken as a long sequence at the start in evening and morning twilight. In the evening, we take sky flats by pointing the telescope about 1 hour east of the zenith. The following are very rough estimates. We should start taking 1 sec test exposures. We should do the bluest filter first when the sky is brightest, and the reddest filter last when the sky is darkest. In the morning, we take a dawn sky flats. We point the telescope about 1 hour west of the zenith. We should do the reddest filter first when the sky is darkest, and the bluest filter at the last when the sky starts too bright in the morning. For good flat field, the counts should be between 10,000 to 30,000 counts.

In the list of ucm file from flat frames, we should subtract bias before running *makeflat* using *grab*. In the last frames of a run, we must remove the last frame of flat frame because sky flats are terminated by stopping the run in the middle of an exposure, so the last exposure is not a good data (Dhillon et al., 2007).

After setting apertures, we have an ASCII file. We open the reduce file to set up a data of specifying the reduction that we want, before plotting a light curve. This consists of an ASCII file with many options, for instance, the names of the calibration files, the method of extraction to use (optimal or normal), whether to vary the aperture radii or hold them fixed, etc. (Dhillon et al., 2007).

We obtained the data on 30 nights (38 light curves) in filters u' , g' , r' , i' , $i'+z'$, z' and KG5 where some data were from Dr. Puji Irawati and we would also like to thank Dr. J.J. Hermes for the observational data with 4.2-meter William Herschel Telescope (WHT) with ULTRACAM in u' , g' and r' filters. Our observation log in each night is presented in Table 3.3.

3.2 Data Reduction

ULTRACAM data reduction pipeline software is to do reduction and analysis of ULTRACAM/ULTRASPEC multi-CCD data. This pipeline has been designed to serve two apparently conflicting purposes. First, whilst observing, it acts as a quick-look data reduction facility, with the ability to display images and generate light curves in real time and second, to enable quick-look reduction at the same time of observation (Dhillon et al, 2007). We will go through the reduction step to obtain the light curve. In the observations, we got raw images, bias frames and flat frames from ULTRASPEC.

Table 3.3 Observation of SDSS J1021+1744 obtained from TNT using ULTRASPEC and WHF using ULTRACAM. The first column shows observation date, column 2 and 3 show time of observation start and end of exposure in Universal Time, column 4 show SDSS filters, telescope in column 5 and exposure time in the last column.

| Date | UT start | UT end | Filter | Telescope | Exp. time (sec) |
|-------------|----------|----------|---------|-----------|--------------------|
| 2014 Jan 07 | 20:27:49 | 22:10:17 | g' | TNT | 59.670 |
| 2014 Jan 08 | 16:56:17 | 18:14:52 | clear | TNT | 59.670 |
| 2014 Jan 08 | 20:02:05 | 21:23:39 | clear | TNT | 59.670 |
| 2014 Jan 10 | 16:01:33 | 20:16:02 | r' | TNT | 55.667 |
| 2014 Jan 11 | 15:47:19 | 23:23:08 | z' | TNT | 43.667 |
| 2014 Jan 11 | 18:58:30 | 19:45:29 | $i'+z'$ | TNT | 24.777 |
| 2014 Jan 11 | 21:53:02 | 23:23:08 | r' | TNT | 34.777 |
| 2014 Jan 12 | 18:14:40 | 19:45:29 | $i'+z'$ | TNT | 12.772 |
| 2014 Jan 12 | 22:03:15 | 23:10:48 | KG5 | TNT | 49.777 |
| 2014 Jan 15 | 20:21:41 | 22:22:30 | r' | TNT | 58.777 |
| 2014 Jan 28 | 15:04:48 | 16:37:17 | KG5 | TNT | 9.852 |
| 2014 Jan 31 | 16:54:42 | 20:29:19 | i' | TNT | 3.352 |
| 2014 Feb 11 | 19:35:39 | 21:00:47 | g' | TNT | 12.777 |
| 2014 Feb 28 | 18:38:05 | 20:31:30 | g' | TNT | 3.352 |
| 2014 Mar 26 | 14:56:13 | 16:47:43 | g' | TNT | 9.872 |
| 2014 Mar 29 | 13:10:23 | 15:11:32 | r' | TNT | 9.852 |

Table 3.3 Observation of SDSS J1021+1744 obtained from TNT using ULTRASPEC and WHF using ULTRACAM. The first column shows observation date, column 2 and 3 show time of observation start and end of exposure in Universal Time, column 4 show SDSS filters, telescope in column 5 and exposure time in the last column (Continued).

| Date | UT start | UT end | Filter | Telescope | Exp. time (sec) |
|-------------|----------|----------|------------|-----------|-----------------|
| 2014 Mar 30 | 12:50:12 | 15:02:53 | g' | TNT | 3.352 |
| 2014 Mar 31 | 12:32:27 | 17:26:53 | r' | TNT | 3.352 |
| 2014 Apr 01 | 12:23:07 | 17:09:11 | g' | TNT | 3.352 |
| 2014 Apr 02 | 14:04:14 | 18:14:38 | g' | TNT | 4.852 |
| 2014 Apr 03 | 16:58:35 | 19:32:28 | r' | TNT | 3.352 |
| 2014 Dec 22 | 17:09:37 | 20:29:12 | g' | TNT | 4.852 |
| 2015 Jan 01 | 20:44:18 | 23:06:57 | KG5 | TNT | 10.352 |
| 2015 Jan 12 | 20:32:47 | 21:33:49 | g' | TNT | 9.876 |
| 2015 Jan 17 | 01:12:31 | 02:55:59 | $u' g' r'$ | WHF | 12;4;4 |
| 2015 Feb 19 | 16:44:53 | 19:28:52 | g' | TNT | 9.352 |
| 2015 Feb 19 | 19:31:20 | 22:52:28 | r' | TNT | 9.352 |
| 2015 Feb 24 | 15:47:19 | 17:08:34 | KG5 | TNT | 9.862 |
| 2015 Mar 18 | 12:57:49 | 16:06:24 | r' | TNT | 9.352 |
| 2015 Mar 18 | 16:09:00 | 19:16:25 | g' | TNT | 9.352 |
| 2015 Mar 19 | 12:28:51 | 14:11:28 | i' | TNT | 6.000 |
| 2015 Mar 19 | 15:38:22 | 17:44:46 | g' | TNT | 9.352 |
| 2015 Mar 19 | 18:47:17 | 20:51:36 | KG5 | TNT | 7.352 |

Table 3.3 Observation of SDSS J1021+1744 obtained from TNT using ULTRASPEC and WHF using ULTRACAM. The first column shows observation date, column 2 and 3 show time of observation start and end of exposure in Universal Time, column 4 show SDSS filters, telescope in column 5 and exposure time in the last column (Continued).

| Date | UT start | UT end | Filter | Telescope | Exp. time (sec) |
|-------------|----------|----------|--------|-----------|--------------------|
| 2015 Mar 20 | 12:16:12 | 13:36:15 | g' | TNT | 9.352 |
| 2015 May 12 | 12:45:53 | 15:03:51 | g' | TNT | 9.352 |
| 2016 Jan 08 | 20:44:12 | 22:55:41 | g' | TNT | 6.600 |
| 2016 Jan 09 | 19:14:10 | 21:13:16 | g' | TNT | 11.600 |
| 2016 Jan 10 | 16:12:31 | 22:37:41 | g' | TNT | 6.600 |

3.2.1 Bias frames

A bias frame is an image obtained from an electronic image sensor. For observation, we used the 2.4 meter with ULTRASPEC instrument, the first thing we should to create a mean bias frame and check the bias level, zero exposure time (without light). The size of bias frames is equal to observe images size. After that we agree on bias level, find a bias run, write the comments and then select run of bias to combine bias frame for making master bias as shown in Figure 3.4.



Figure 3.4 The process of combine bias.

3.2.2 Flat frames

Flat field calibration is to remove image sensor pixel differences and to remove optical effects such as dust spots, etc. For flat fields with TNT, we take twilight flat fields. Flat-fields are obtained by observing the sky during the evening and/or the morning twilight, a stable of a uniform light source, e.g. twilight clear sky. Flat frames are subtracted with a master bias then we get master flat. The chart of making master flat frame is seen in Figure 3.5.

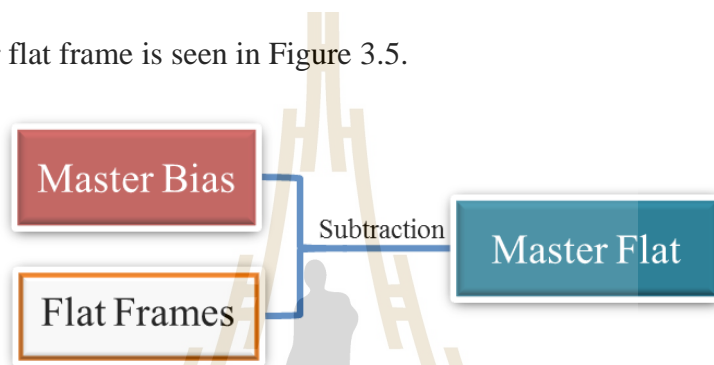


Figure 3.5 The process of flat subtraction.

3.2.3 Reduction of data

In order to obtain the clean images, we have to subtract master bias from raw images and then correct with the master flat. For Equation (3.1) shows process of clean image. After the reduction process, the clean images are ready to do photometry.

$$Clean\ image = \frac{Debiassing}{flatfielding} = \frac{(Raw\ image)-(Master\ Bias)}{Master\ flat} \quad (3.1)$$

And the chart of clean image as shown as in Figure 3.6

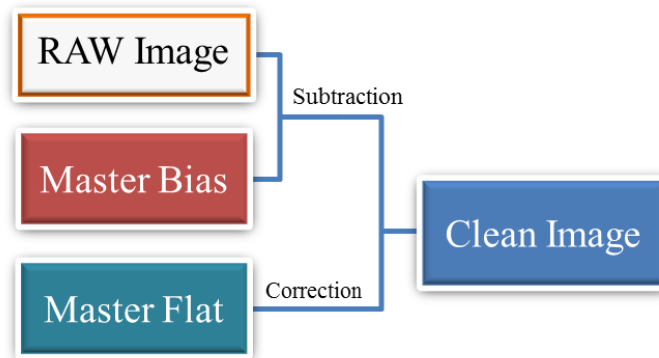


Figure 3.6 The process of data reduction.

3.3 Light curve analysis

In order to perform the light curve for each observational data, the light curve of SDSS J1021+1744 and reference star have been plotted between the normalized flux versus observation time in modified Julian date time (MJD) as shown in Figure 3.7. Then MJD was converted into the orbital phase in all of the light curves and set the primary eclipse at orbital phase 1 (shown in Figure 3.8, 3.9, 3.10 and 3.11).

The variability of SDSS J1021+1744 is periodic by using the period; 0.1403587436 days. The orbital phase can be found by using Equation 2.35 and also use the orbital period, P_{orb} , from Parsons et al., 2013.

$$Cycle\ of\ Phase = \left[\frac{BJD_{now} - BJD_{TDB0}}{0.1403587436} \right] \quad (3.1)$$

From Figure 3.8 to Figure 3.11, the system was observed in filter g' , $i'+z'$, KG5 and r' with ULTRASPEC. We can see that the unusual dips are changing in relative flux and filters. The dips in filter g' is deeper than r' filter because WD is apparently dominated in the filter g' .

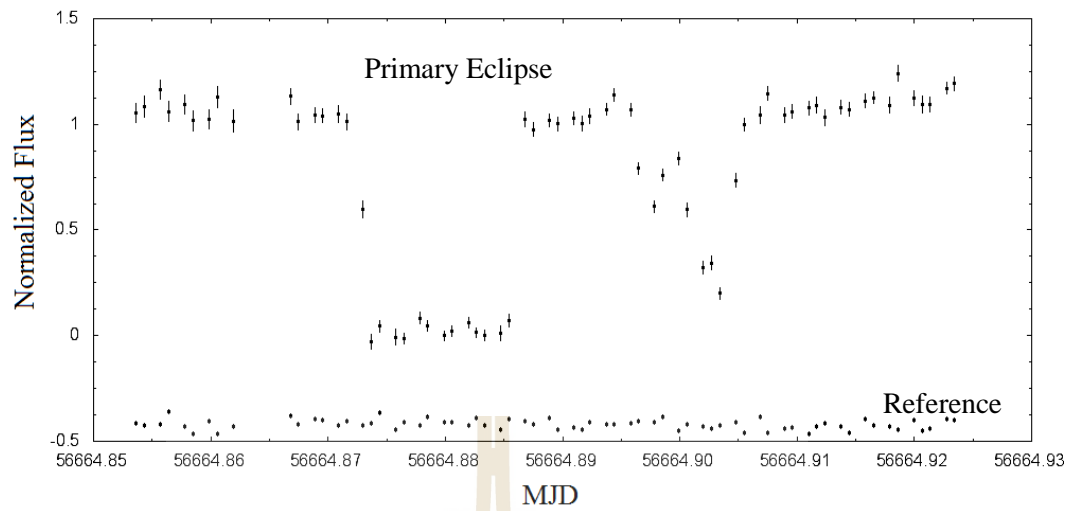


Figure 3.7 The first observation at TNT 2.4 meter on 7 January 2014, light curve of SDSS J1021+1744 and reference star with ULTRASPEC (g' filter). Before the primary eclipse around MJD of 56664.86, shows a little gap due to the rotation limited of the TNT telescope.

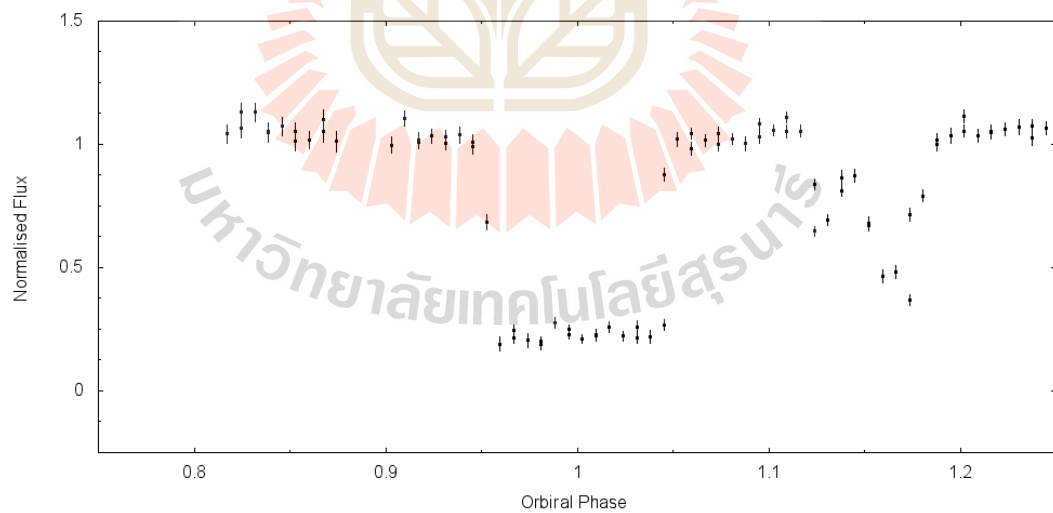


Figure 3.8 The light curve of SDSS J1021+1744 in g' filter (7 Jan 2014).

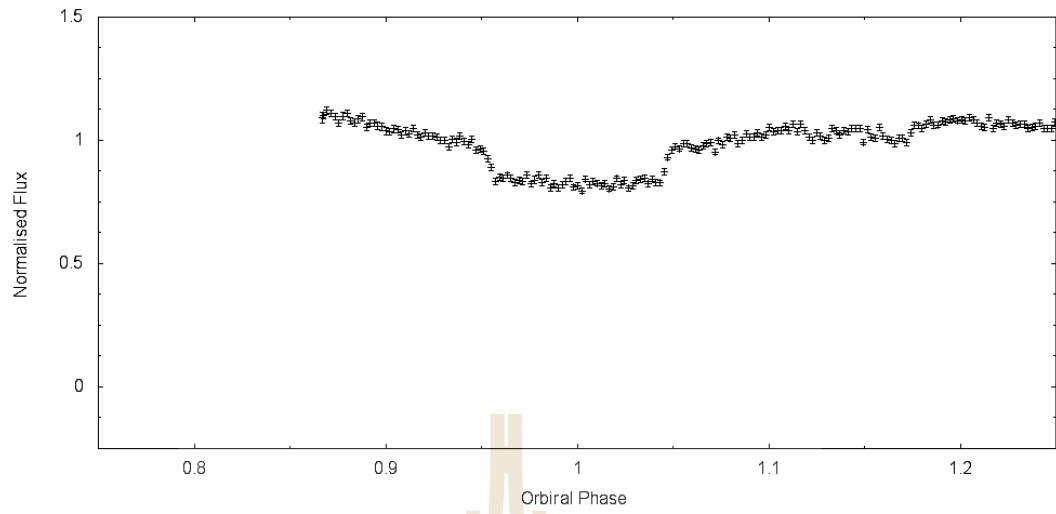


Figure 3.9 The light curve of SDSS J1021+1744 in SDSS $i'+z'$ filter (11 Jan 2014).

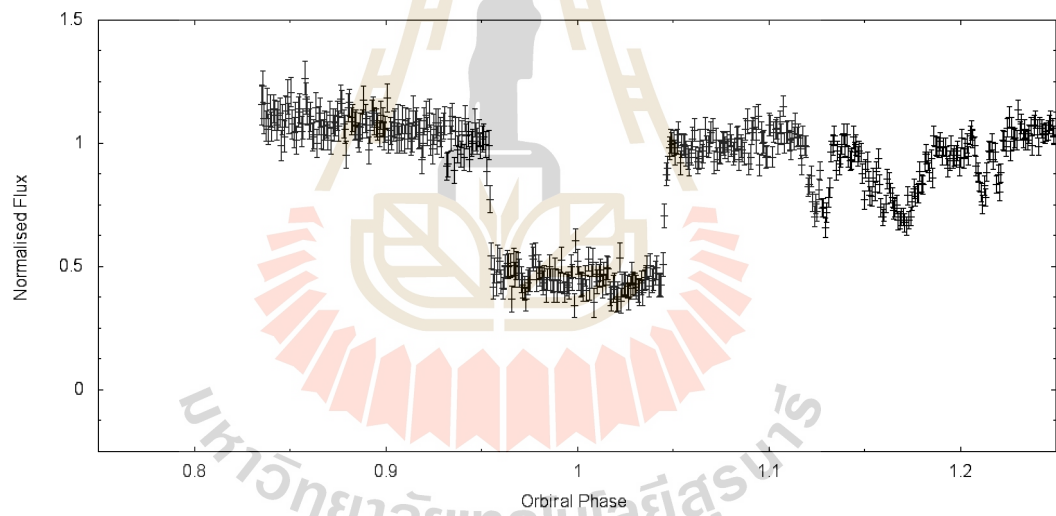


Figure 3.10 The light curve of SDSS J1021+1744 in SDSS KG5 filter (28 Jan 2014).

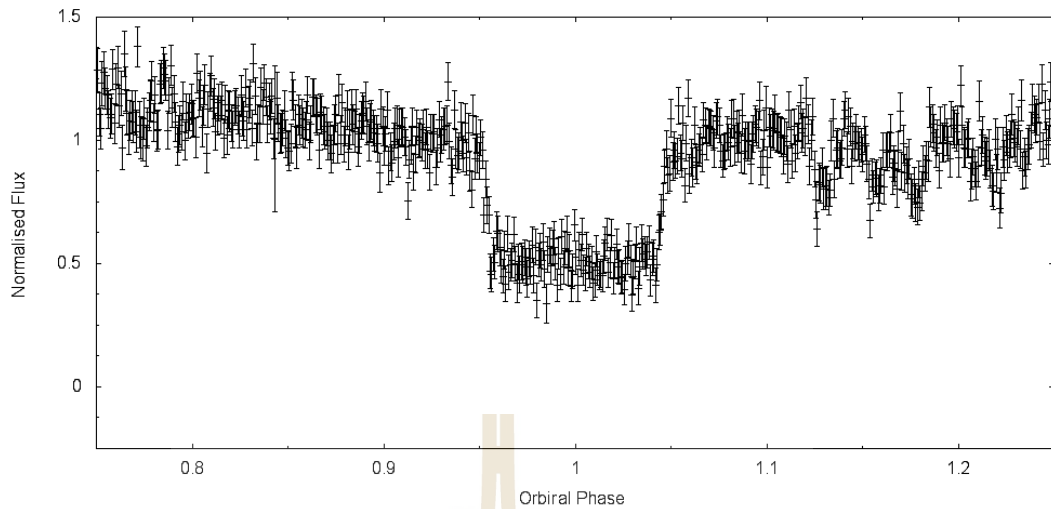


Figure 3.11 The light curve of SDSS J1021+1744 in SDSS r' filter (29 MAR 2014).

3.4 The initial parameters

We obtained the initial parameters from Parson et al., 2013, the orbital period of SDSS J1021+1744 is $0.140359073(1)$ days and the mass of white dwarf is $0.50 \pm 0.05M_{\odot}$.

3.4.1 Orbital separation

According to Parsons et al., 2013, the radial velocity amplitude of main sequence star is $K_{MS} = 235 \pm 9 \text{ kms}^{-1}$ with a systemic velocity of $V_0 = -20 \pm 6 \text{ kms}^{-1}$. With this information, and the orbital period, we can constrain the mass of the white dwarf, using the mass function Equation (2.4) for given inclination.

3.4.2 Inclination

The inclination of a binary is a description in degrees of the tilt of the orbital plane with respect to an Earth observer. SDSS J1021+1744 system has a high inclination as mentioned in Parsons et al., 2013. For our model, we varied the value of

the inclination from 75° to 90° until we get the best fit parameter by considering the Chi-square value.

3.4.3 The mass ratio

We used the mass functions Equation (2.4), when the mass of secondary star less than primary star. For SDSS J1021+1744, we constrain the mass of white dwarf as $0.5M_\odot$ and we assumed this system is in a circular orbit then we can obtain mass of the main-sequence as

$$M_{MS} = 0.300558M_\odot$$

From Equation (2.5), the mass ratio q is usually defined as the mass of the less massive star divided by that of the more massive star:

$$q = \frac{0.3005M_\odot}{0.5000M_\odot} = 0.6011$$

3.4.4 Semi-major axis

In every binary system, the two stars move in elliptical orbits around the center of mass which the semi-major axis a is one-half of the ellipse long axis. From Equation (2.2), we can get the semi-major axis as

$$a = 734,278.4034 \text{ km} = 1.0554R_\odot$$

3.4.5 Effective temperature

The temperature parameter in our model is the effective temperature of the star, T_{eff} . From Parson et al., 2013, the white dwarf effective temperature is 32595 ± 928 K. The spectral type of the main-sequence is M4 which the effective temperature ranges is between 3170 and 3400 K. Therefore in this model, the effective temperature of the main-sequence star is varied in the range 3170 to 3840 K. For a white dwarf effective temperature can be obtained by fixing the effective

temperature of the main-sequence and adjust the effective temperature of the white dwarf until we have the best fitting values by considering from the Chi-square.

3.4.6 Modified omega potential

The gravitational equipotential demarcates the surface along with the constant gravitational potential energy. As the value of the equipotential is increased, the size of the star decreases. The gravitational potential increases as one approach the mass center. Ω_{inner} is the value of the inner critical Roche equipotential and represents the point at which the stars just come into contact. Ω_{outer} is the value of the outer critical Roche equipotential and represents the limit to stability to any over contact system since the outer potential has a hole in it gravitational acceleration equal to 0 and gas will leave the system (Bradstreet, 2005).

3.4.7 Limb darkening

Limb darkening is an optical effect in the stars, where the center of the star appears brighter than the edge, including the Sun. If we look at the surface of the Sun from an angle rather than from directly above then the surface brightness is lower compared with the center of the Sun. In the same way, if we observe a star, the edge of a star is fainter than the center of a star.

3.4.8 Reflection effect

Reflection effect or bolometric albedo or surface albedo is a phenomenon when flux from the radiative star strikes the surface of the other; its energy will heat up the receiving surface and generate more flux. For radiative stars, the effective temperature is higher than 7200 K the albedo effect will be approximate to be 1.00 and convective stars the effective temperature are less than 7200 K the albedo will be approximately 0.50 (Bradstreet, 2005).

3.4.9 Gravity darkening

Gravity darkening is an astronomical phenomenon when the star rotates rapidly, its shape will be an oblate spheroid or teardrop. When a star is oblate, it has a radius at its equator larger than its poles of a star. As a result, the poles have a higher surface gravity, and thus higher temperature and brightness. Therefore, the poles are gravity brighter, and the equator gravity is darker.

3.4.10 Third light

Third light or wavelength dependent, this parameter takes into account any contamination in the data due to sources other than the binary stars themselves. This can be a third star that is part of the binary or even a field star that could not be excluded from the diaphragm when observing at the telescope because of its coincidental proximity to the binary. Third light is in the same units as the input or output flux and is not a luminosity fraction like L_1 and L_2 .

3.4.11 Surface brightness ratio

Surface brightness ratio is the ratio of effective temperature of two stars.

$$J = \left[\frac{T_{eff}(MS)}{T_{eff}(WD)} \right]^4 = \left[\frac{3170}{32595} \right]^4 = 8.946 \times 10^{-5}$$

3.5 Software for modeling binary star

In this work, we used JKTEBOP code, PHOEBE and Binary Maker 3.0 for modeling the binary system of SDSS J1021+1744. We obtained the input parameters from Parsons et al., 2013, such as mass of white dwarf, the orbital period of SDSS J1021+1744 and the radial velocity of main-sequence star for SDSS J1021+1744, etc. We have to find the mass of the main-sequence star, the semi-major axis, the new orbital period, potential energy Ω_1 and Ω_2 . These are the initial parameters.

Then, each software will give the best fitting model and also the best fitting parameters. First, we used JKTEBOP code to obtain the time of mid-eclipse. Secondly, PHOEBE is used for obtaining the best fitting parameters. Lastly, we use the Binary Maker to construct the 3D model.

3.5.1 JKTEBOP code

JKTEBOP code is used for analyzing and modelling of the light curves of the detached eclipsing binary. This software is very stable and has a lot of additional goodies, including extensive Monte Carlo or bootstrapping error analysis algorithms (Rebassa-Mansergas et al, 2014). JKTEBOP will give best parameters of fitting from the light curve and residual. To obtain the binary parameters for SDSS J1021+1744, we should know some parameters of the binary system such as the mass ratio of the binary system, inclination of orbital, ratio of radii, sum of radii, gravity darkening, limb darkening, surface brightness, reflection effect, the orbital period of eclipsing binary system and the reference time of primary minimum as shown in Table 3.4.

First, we have to input the initial parameter of SDSS J1021+1744 which we use the mass ratio from the calculation, the reference time of primary minimum (MJD) can be found from the observations and the orbital period (in day) and the orbital inclination were from Parsons's estimation (Parson et al., 2013). Thus, we can obtain other parameters such as surface brightness ratio, limb darkening, reflection effect, gravity darkening etc.

Table 3.4 The initial parameters of SDSS J1021+1744 for inputting in JKTEBOP.

| Initial value of the parameters | | | |
|---------------------------------|-----------|--|---------------------------------|
| 3 | 1 | Task to do (from 2 to 9) | Integ. ring size (deg) |
| 0.363474 | 31.01568 | Sum of the radii | Ratio of the radii |
| 81.5 | 0.6012 | Orbital inclination (deg) | Mass ratio of system |
| 0.062595 | 0.146517 | $ecos\omega$ or eccentricity | $esin\omega$ or periastron long |
| 1 | 1 | Gravity darkening (star A) | Gravity darkening (star B) |
| 0.000089 | 0.25 | Surface brightness ratio | Amount of third light |
| sqrt | lin | LD law type for star A | LD law type for star B |
| 0 | 0 | LD star A (linear coeff) | LD star B (linear coeff) |
| 0.5 | 0.3 | LD star A (nonlin coeff) | LD star B (nonlin coeff) |
| 0.26 | 0.28 | Reflection effect star A | Reflection effect star B |
| 1 | 4 | Phase of primary eclipse | Light scale factor (mag) |
| 0.140359 | Orbital | Orbital period of eclipsing binary system (days) | |
| 56742.64 | Reference | Reference time of primary minimum (HJD) | |

3.5.2 PHOEBE

PHysics Of Eclipsing BinariEs (PHOEBE) is a tool for the modeling of eclipsing binary based on the real photometric and spectroscopic data together with the Wilson-Devinney (WD) code. PHOEBE is divided into several tabs screen page with selected content that fit into a specific category (Prsa, 2010). PHOEBE can give the best fitting model for the light curve. We can modify and change the input parameters appropriately until we get the best fit parameters of light curve.

The output parameters from JKTEBOP were used as the input parameters for PHOEBE such as the mass ratio 0.60112, the inclination $i = 81.5^\circ$, etc. PHOEBE software consists of several displays (as seen in Figure 3.12 and 3.13) for obtaining the stellar and binary parameters such as mass ratio, ephemeris HJD_0 , semi-major axis, the mass ratio, systemic velocity, inclination and stellar surface potential, etc. The initial parameters for PHOEBE are shown in Table 3.5. PHOEBE gives output files which contain the output parameters after several iterative for the best fitting of the light curve model as shown in Figure 3.13.

Table 3.5 Initial input parameters of SDSS J1021+1744 into PHOEBE.

| Parameter | g' | KG5 | r' | i' |
|---------------|------|-------------------|------|------|
| Mass ratio | | 0.60112 | | |
| Semi-major | | $1.05421R_\odot$ | | |
| Inclination | | 81.5 degree | | |
| Ω_{WD} | | 88.68052 | | |
| Ω_{MS} | | 3.08979 | | |
| WD T_{eff} | | 17000 K | | |
| MS T_{eff} | | 3185 K | | |
| P_{orb} | | 0.1403587357 days | | |

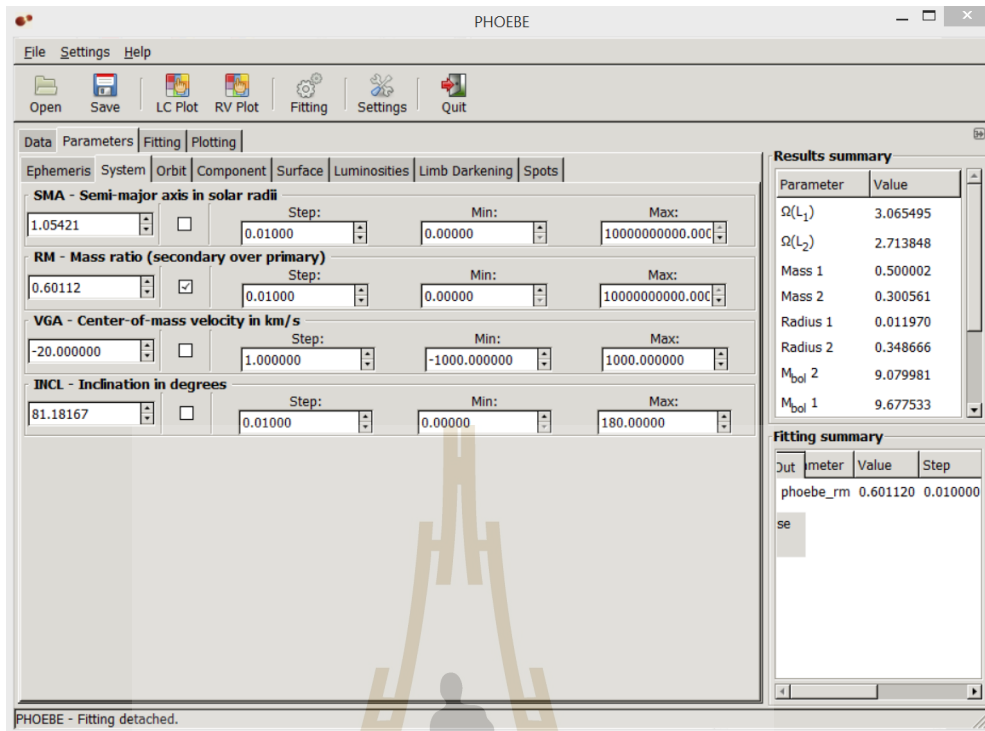


Figure 3.12 The display of PHOEBE, shows the initial input parameters.

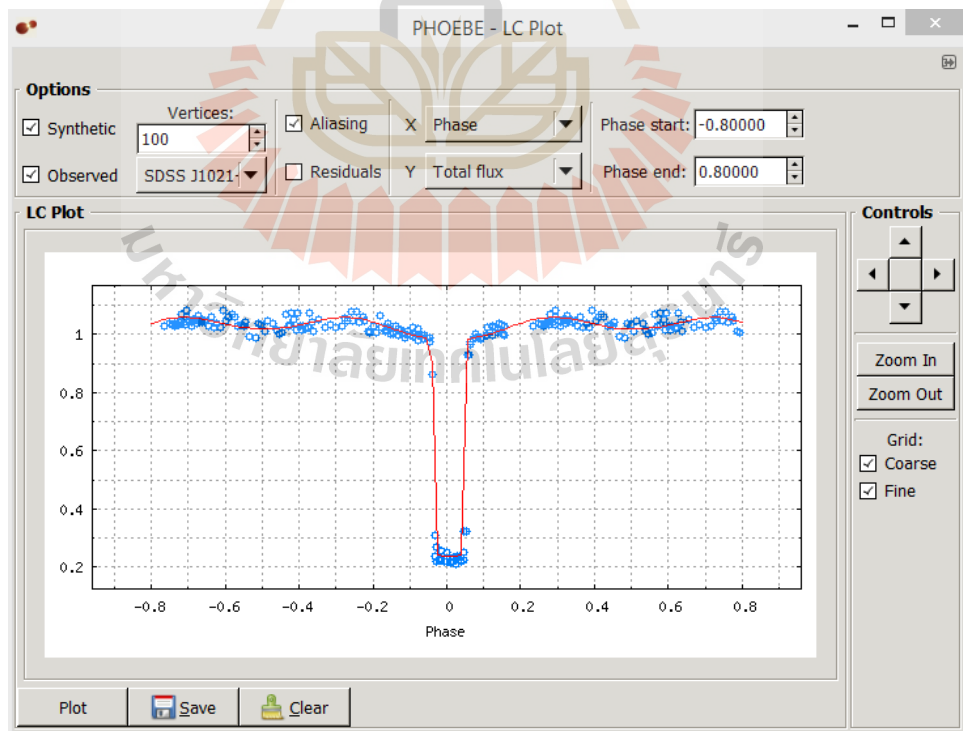


Figure 3.13 The example display for the result of the observational data using PHOEBE.

3.5.3 Binary Maker 3.0

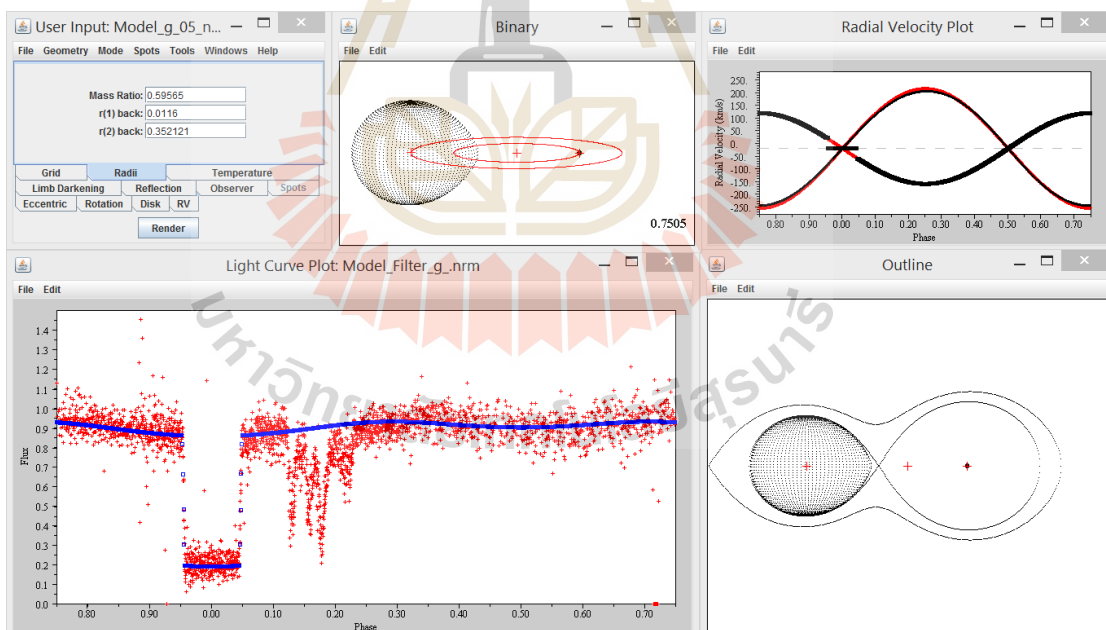
Binary Maker 3.0 (BM3) is a software for modeling any type of binary star system. The display shows the theoretical and observational data as well as a 3D model of the star system. This software can generate professional quality postscript output and created on window display. BM3 can add the spot of stars, spot radius, temperature factor of spot, stars potential, the effective temperature of star, wavelength, velocity of system, radial velocity, eccentricity and orbital period. From the foregoing, we need first of these parameters. The expected result of BM3 will give the proper synthetic of light curve and also in the 3D model of the eclipsing binary star.

The output of parameters from PHOEBE were used as the input parameters for BM3 such as the mass ratio, $r(1)$ back and $r(2)$ back are the radii of WD and MS stars, the wavelength which is used for observation, temperature 1 and 2 are the effective temperature of WD and MS stars and orbital inclination in degree as shown in Table 3.6.

The display of BM3 software in Figure 3.14 shows the input parameters (Table 3.6) in the top right hand side, on the bottom shows the observation light curve in red dot, model fitting in blue line and in the top middle window shows the 3D model of eclipsing binary and on the bottom shows the potential outline surface.

Table 3.6 The initial input parameters of BM3 for SDSS J1021+1744.

| Parameters | |
|---------------|---------------------|
| Mass ratio | 0.600112 |
| r(1) back | $0.011353R_{\odot}$ |
| r(2) back | $0.352117R_{\odot}$ |
| Wavelength | 5025 \AA |
| Temperature 1 | 18800K |
| Temperature 2 | 3174K |
| Inclination | 81.5° |

**Figure 3.14** The BM3 display shows an example light curve from observation and modeling.

3.6 Roche lobe of SDSS J1021+1744

After we obtained the initial parameters from modeling binary star, we can find Roche lobe shapes corresponding to constant Ψ from Equation (2.10), and then we have found the possible shapes of the stars of a binary system from Equation (2.21) and (2.28).

We then obtain r_{pole} of the white dwarf and the main-sequence of SDSS J1021+1744 from BM3 for r point and r back.

$$r_{1_pole} = \tilde{r}_{pole_WD} = 0.011353R_{\odot}$$

$$r_{2_pole} = \tilde{r}_{pole_MS} = 0.309411R_{\odot}$$

Using Newton-Raphson from Equations (2.28), we can obtain r_1 point = 0.011353 and r_1 back = 0.011353 of white dwarf. And we can also obtain r_2 point = 0.399435 R_{\odot} and r_2 back = 0.352117 R_{\odot} for the main-sequence.

After obtaining \tilde{r}_{pole} at the pole of white dwarf and main-sequence from a model, we can define a potential function from Equation (2.26) at the pole of M_{WD} as follow;

$$\Omega_1 = \frac{1}{0.011353} + q \left[\frac{1}{\sqrt{(0.011353)^2 + 1}} \right] = 88.68357$$

Potential function Ω_2 from M_{MS} ,

$$\Omega_2 = \frac{1}{0.309411} + \frac{1}{q} \left[\frac{1}{\sqrt{(0.309411)^2 + 1}} \right] = 4.82107$$

Using Equation (2.33) the polynomial can be written as shown in Table 3.7, 3.8 and 3.9 for \tilde{r}_{L1} , \tilde{r}_{L2} and \tilde{r}_{L3} respectively.

Table 3.7 The result from the calculation of \tilde{r}_{L_1} , the Lagrange point L_1 and Roche lobe potential of SDSS J1021+1744.

| r_0 | Lagrange point, L_1 | | | |
|-------|-----------------------|----------------|---------------------------|------------------|
| | 0.5 | Ω_{L_1} | Ω_{L_1}' | Ω_{L_1}'' |
| r_1 | 0.55129121 | 3.1018135 | -1.396094 | 27.218972 |
| r_2 | 0.552154297 | 3.065497859 | -0.023169871 | 26.84532613 |
| r_3 | 0.552153959 | 3.065487863 | 9.08001×10^{-06} | 26.86652412 |
| r_4 | 0.552153959 | 3.065487863 | 1.43496×10^{-12} | 26.86651563 |
| r_5 | 0.552153959 | 3.065487863 | 0 | 26.86651563 |

From Equation (2.25) for L_1 , $\theta = 90^\circ$, $\phi = 0^\circ$, so $\nu = 0$ and $\lambda = 1$. So along the positive x-axis and mass ratio, $q = 0.601116$. The Roche potential inner and L_1 of SDSS J1021+1744 is obtained from Equation (2.31).

$$\Omega_{inner} = \frac{1}{(0.552153959)} + q \frac{1}{\sqrt{0.552153959^2 - 2(0.552153959) + 1}}$$

$$- q(0.552153959) + \frac{1}{2}(1 + q)(0.552153959)^2$$

We define Lagrange point L_1 from Equation (2.33)

$$\tilde{r}_{L_1 5} = \tilde{r}_{L_1 4} - \frac{\Omega_{L_1}'}{\Omega_{L_1}''} = 0.552153959 - \frac{0}{26.86651563} = 0.552153959$$

$$L_1 = 0.77725549$$

The result of \tilde{r}_1 and \tilde{r}_2 are shown in the Appendices Table A.1 and A2 respectively and in Figure 3.18.

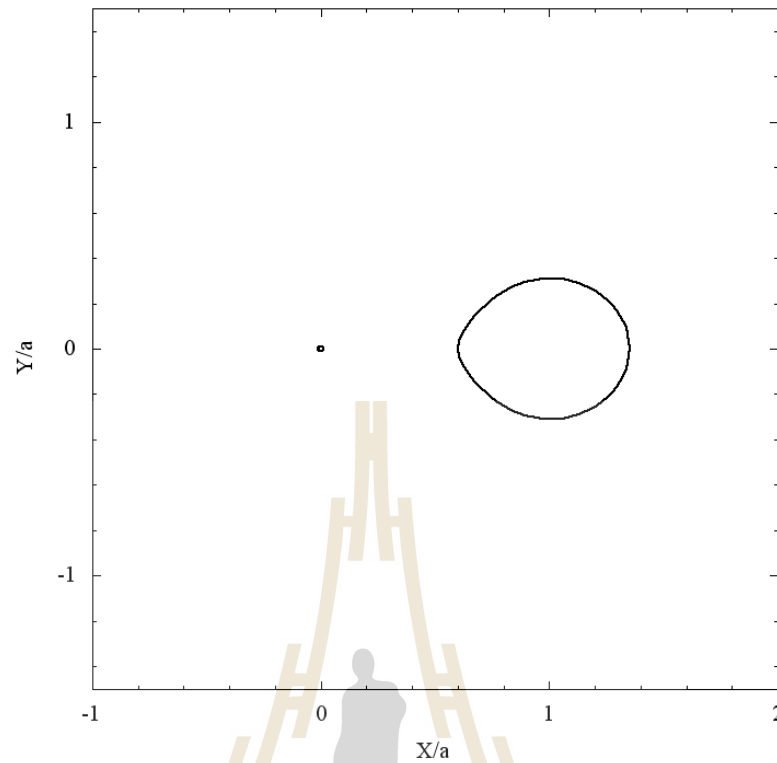


Figure 3.15 Shows the results of the analysis solution of \tilde{r} , the horizontal and vertical scale by the separation of two stars (a , is semi-major axis). The black solid line shown the main-sequence star, a small circle is a white dwarf.

The series converges quickly to find the value of \tilde{r} for L_1 (in Table 3.7) using an initial guess of 0.5. Notice that for L_2 , the values (in Table 3.8) of θ , ϕ , ν and λ at the same as those for L_1 . However, if we use an initial guess of 1.5 we instead find to find the value of \tilde{r} for L_3 (in Table 3.9) from Equation (2.40) and (2.41).

Table 3.8 The result from the calculation of \tilde{r}_{L_2} , the Lagrange point L_2 and Roche lobe potential of outer point of SDSS J1021+1744.

| Lagrange point, L_2 | | | | |
|-----------------------|-------------|----------------|----------------------------|------------------|
| r_0 | 1.5 | Ω_{L_2} | Ω_{L_2}' | Ω_{L_2}'' |
| r_1 | 1.588756272 | 2.768480167 | -1.048350444 | 11.81156459 |
| r_2 | 1.612240783 | 2.716114961 | -0.187658562 | 7.990737472 |
| r_3 | 1.613349552 | 2.713847111 | -0.008112899 | 7.317035503 |
| r_4 | 1.613351787 | 2.713842607 | -1.62861×10^{-05} | 7.287693268 |
| r_5 | 1.613351787 | 2.713842607 | -6.58456×10^{-11} | 7.287634338 |
| r_6 | 1.613351787 | 2.713842607 | 0 | 7.287634338 |

Using Equation (2.25),

$$\tilde{r}_{L_{2_6}} = \tilde{r}_{L_{2_5}} - \frac{\Omega_{L_2}'}{\Omega_{L_2}''} = 1.613351787 - \frac{0}{7.287634338} = 1.613351787$$

Using Equation (2.35),

$$\Omega_{outer} = \frac{1}{(1.613351787)} + q \frac{1}{\sqrt{1.613351787^2 - 2(0.1613351787) + 1 - q(1.613351787) + \frac{1}{2}(1+q)(1.613351787)^2}}$$

$$\Omega_{Roche\ outer} = 3.065487863$$

And

$$L_2 = 1.613351787$$

For L_3 , $\theta = 90^\circ$, $\phi = 180^\circ$, so $v = 0$ and $\lambda = -1$. The functions to be used in the Newton Raphson method for Lagrangian L_3 are shown in Table 3.9.

Table 3.9 The result from the calculation of \tilde{r}_{L_3} , the Lagrange point L_3 of SDSS J1021+1744.

| Lagrange point, L_3 | | | | |
|-----------------------|-------------|----------------|-----------------|------------------|
| r_0 | 0.5 | Ω_{L_3} | Ω_{L_3}' | Ω_{L_3}'' |
| r_1 | 0.659572064 | 2.9014415 | -2.865488667 | 17.95733289 |
| r_2 | 0.756891774 | 2.623096323 | -0.85975255 | 8.834310627 |
| r_3 | 0.776674896 | 2.576947829 | -0.127308894 | 6.435227458 |
| r_4 | 0.777255028 | 2.575665072 | -0.003529725 | 6.084348929 |
| r_5 | 0.777255495 | 2.575664047 | -2.83284E-06 | 6.074587553 |
| r_6 | 0.777255495 | 2.575664047 | -1.82654E-12 | 6.074579718 |
| r_7 | 0.777255495 | 2.575664047 | 0 | 6.074579718 |

We use Equation (2.33) for finding L_3

$$\tilde{r}_{L_{37}} = \tilde{r}_{L_{36}} - \frac{\Omega_{L_3}'}{\Omega_{L_3}''} = 0.777255495 - \frac{0}{6.074579718} = 0.777255495$$

$$L_3 = 0.77725549,$$

Equation (2.45) to obtain Lagrange point L_4 :

$$L_4 = (0.5, 0.86603)$$

and using Equation (2.46) to get Lagrange point L_5 :

$$L_5 = (0.5, -0.86603)$$

Thus, the center of mass lies on the x-axis and its distance from M_1 is

$$\text{Central of mass} = 0.375436$$

The result of Roche lobe inner potential of SDSS J1021+1744 is shown in Appendices Table A.3 and Table A.4 and in Figure 3.16.

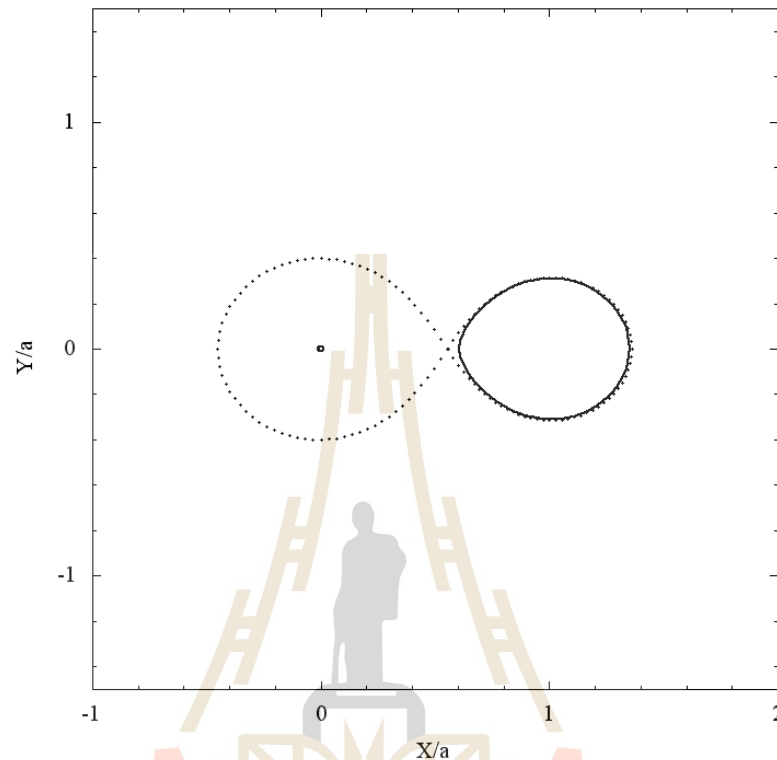


Figure 3.16 The Roche lobe inner potential of SDSS J1021+1744, scale separation of two stars. The dot lines indicate the Roche lobe and the main-sequence star, in black solid line is close to filling its Roche lobe.

The locations of L_4 and L_5 are easy to determine because they form equilateral triangles with the centers of m_1 and m_2 normalize distance from the center of M_1 to M_2 in x -axis of $R = 1$, so a half of distance from the center of mass $R/2$ as shown in Figure 3.17. We identified the position of the Lagrangian point in Table 3.10. And the result of the calculation show in Table 3.11.

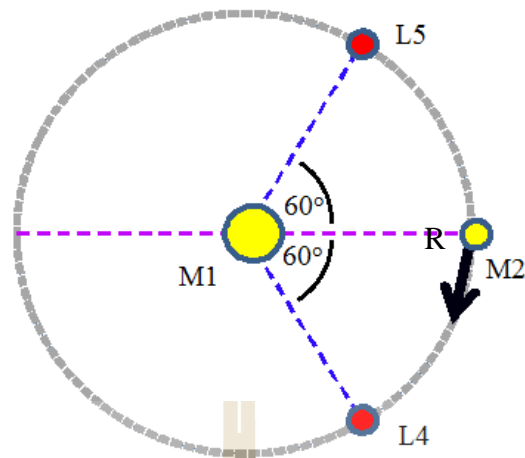


Figure 3.17 The Lagrange L_4 and L_5 (red circles) points 60 degrees ahead of and behind the position of M_2 in its orbit. M_1 is more massive than M_2 . The gray dashed circle is the orbital of M_2 , the blue and magenta dashed lines are the distance from M_1 to M_1 (Yellow circle).

Table 3.10 The position of Lagrange point L_1, L_2, L_3, L_4 and L_5 position of M_1, M_2 and center of mass x and y coordinates for SDSS J1021+1744 model.

| Position | x | y |
|----------------|----------|----------|
| L_1 | 0.55215 | 0 |
| L_2 | 1.61335 | 0 |
| L_3 | -0.77726 | 0 |
| L_4 | 0.50000 | 0.86603 |
| L_5 | 0.50000 | -0.86603 |
| M_1 | 0 | 0 |
| M_2 | 1 | 0 |
| Center of Mass | 0.375436 | 0 |

Table 3.11 The binary system parameter of SDSS J1021+1744 from the calculation.

| Parameter | Value |
|---------------------------------|------------------------------|
| Mass ratio [M_{MS}/M_{WD}] | 0.600112 |
| Omega 1 | 88.68357 |
| Omega 2 | 4.82107 |
| Omega inner | 3.0654876 |
| Omega outer | 2.7138426 |
| radius point WD | 0.011353 |
| radius back WD | 0.011353 |
| radius point MS | 0.399436 |
| radius back MS | 0.352117 |
| L_1 | 0.552154 |
| L_2 | 1.6133518 |
| L_3 | -0.7772555 |
| M_{WD} [M_{\odot}] | 0.500000 |
| M_{MS} [M_{\odot}] | 0.300558 |
| Semi-major axis [R_{\odot}] | 1.0554 |
| Period [days] | $0.140358735 \pm 0.00000001$ |

We show the position of Lagrangian points in Roche lobe model of SDSS J1021+1744 in Figure 3.18. This model of binary system is rotates in clockwise direction and scale by the separation of the two stars.

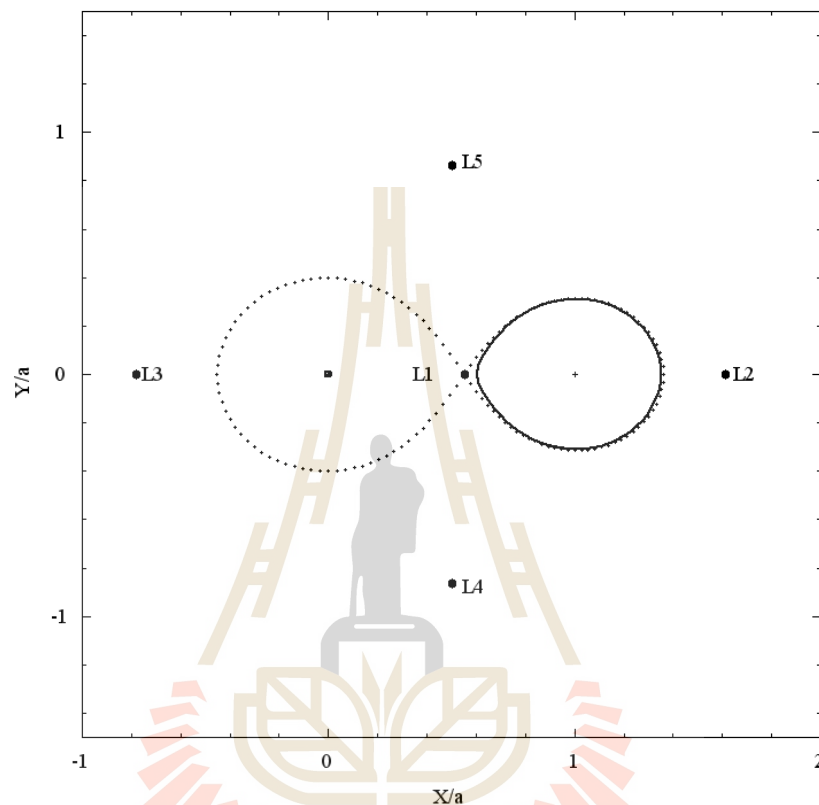


Figure 3.18 The position of the Lagrange points L_1 to L_5 of this binary system and Roche lobe potential inner of SDSS J1021+1744.

CHAPTER IV

RESULTS

4.1 Light curve model fitting

In a modeling of SDSS J1021+1744, we used the radial velocity amplitude of the main-sequence star as $K_{sec} = 235 \pm 9 \text{ kms}^{-1}$ with a systemic velocity of $v_0 = -20 \pm 6 \text{ kms}^{-1}$, the orbital period of 0.140359073. We can constrain the mass of the white dwarf and use the mass of white dwarf is $0.5M_{\odot}$ from Parsons et al. (2013) as input parameters. We get the orbital period 0.1403587435 days, from the mass function using Equation (2.4), we calculate mass ratio 0.600119, inclination 81.5 degree, radii of white dwarf $0.0119R_{\odot}$, radii of main-sequence $0.3444R_{\odot}$, effective temperature of white dwarf 18000K and effective temperature of main-sequence 3174K.

4.1.1 The modeling using JKTEBOP code

We can determine the mid-eclipse timing from 2014 to 2016 of observation to calculate O-C diagram and the new ephemeris of SDSS J1021+1744. The initial parameters are very important for modeling and calculation of the O-C diagram to study a variation of periodic this system. We show the time of mid-eclipse for O-C diagram in Table 4.1 and the output parameters from JKTEBOP are shown in Table 4.2.

Table 4.1 The time of mid-eclipse for SDSS J1021+1744 for the date of observation and list of the filter names, cycle number, the O-C and error from the calculation in seconds.

| Date | Filter | Cycle number | Mid-eclipse time BMJD | O-C (Sec) |
|-------------|---------|-----------------|--------------------------|-------------------|
| 2014 Jan 07 | g' | 0 | 56664.884453 | 0 ± 0.69 |
| 2014 Jan 08 | clear | 6 | 56665.726522 | -7.21 ± 0.60 |
| 2014 Jan 08 | clear | 7 | 56665.866767 | -17.04 ± 0.50 |
| 2014 Jan 10 | r' | 20 | 56667.691596 | -2.75 ± 1.84 |
| 2014 Jan 11 | $i'+z'$ | 28 | 56668.814542 | 3.82 ± 1.33 |
| 2014 Jan 11 | r' | 29 | 56668.954831 | -2.21 ± 0.88 |
| 2014 Jan 12 | $i'+z'$ | 35 | 56669.797234 | 19.44 ± 1.60 |
| 2014 Jan 12 | KG5 | 36 | 56669.937346 | -1.88 ± 0.37 |
| 2014 Jan 15 | r' | 57 | 56672.884969 | 5.84 ± 2.87 |
| 2014 Jan 28 | KG5 | 148 | 56685.657585 | 3.28 ± 1.00 |
| 2014 Jan 31 | i' | 170 | 56688.746022 | 50.34 ± 2.01 |
| 2014 Feb 11 | g' | 249 | 56699.833177 | 0.25 ± 0.03 |
| 2014 Feb 28 | g' | 370 | 56716.817148 | -3.46 ± 0.69 |
| 2014 Mar 26 | g' | 554 | 56742.643111 | -7.41 ± 1.04 |
| 2014 Mar 29 | r' | 575 | 56745.590680 | -4.35 ± 1.71 |
| 2014 Mar 30 | g' | 582 | 56746.573175 | -0.52 ± 2.33 |
| 2014 Mar 31 | r' | 589 | 56747.555820 | 5.80 ± 2.02 |
| 2014 Mar 31 | r' | 590 | 56747.696064 | -4.11 ± 1.37 |

Table 4.1 The time of mid-eclipse for SDSS J1021+1744 for the date of observation and list of the filter names, cycle number, the O-C and error from the calculation in seconds. (Continued)

| Date | Filter | Cycle number | Mid-eclipse time BMJD | O-C (Sec) |
|-------------|------------|--------------|--------------------------|-------------------|
| 2014 Mar 30 | g' | 582 | 56746.573175 | -0.52 ± 2.33 |
| 2014 Apr 01 | g' | 596 | 56748.538265 | 0.08 ± 1.63 |
| 2014 Apr 01 | g' | 597 | 56748.678535 | -7.58 ± 0.82 |
| 2014 Apr 02 | g' | 604 | 56749.661085 | -4.23 ± 1.46 |
| 2014 Dec 22 | g' | 2486 | 57013.816256 | -2.85 ± 0.86 |
| 2015 Jan 01 | KG5 | 2558 | 57023.922065 | -4.62 ± 0.03 |
| 2015 Jan 12 | g' | 2636 | 57034.870133 | 2.81 ± 1.32 |
| 2015 Jan 17 | $u' g' r'$ | 2666 | 57039.080920 | 4.95 ± 0.21 |
| 2015 Feb 19 | g' | 2906 | 57072.766943 | -1.57 ± 0.67 |
| 2015 Feb 19 | r' | 2907 | 57072.907278 | -3.62 ± 1.09 |
| 2015 Feb 24 | KG5 | 2941 | 57077.679470 | -4.07 ± 0.98 |
| 2015 Mar 18 | r' | 3097 | 57099.575478 | -0.27 ± 2.25 |
| 2015 Mar 18 | g' | 3098 | 57099.715804 | -3.10 ± 0.75 |
| 2015 Mar 19 | i' | 3104 | 57100.558106 | 9.82 ± 3.11 |
| 2015 Mar 19 | g' | 3105 | 57100.698346 | -0.44 ± 0.82 |
| 2015 Mar 19 | KG5 | 3106 | 57100.838708 | -0.16 ± 1.41 |
| 2015 Mar 20 | g' | 3111 | 57101.540280 | -19.31 ± 5.67 |
| 2015 May 12 | g' | 3489 | 57154.596187 | 9.15 ± 2.65 |

Table 4.1 The time of mid-eclipse for SDSS J1021+1744 for the date of observation and list of the filter names, cycle number, the O-C and error from the calculation in seconds. (Continued)

| Date | Filter | Cycle number | Mid-eclipse time BMJD | O-C (Sec) |
|-------------|--------|--------------|--------------------------|------------------|
| 2016 Jan 09 | g' | 5215 | 57396.855362 | 5.398 ± 3.06 |
| 2016 Jan 10 | g' | 5221 | 57397.697370 | -7.08 ± 1.97 |
| 2016 Jan 10 | g' | 5222 | 57397.837884 | 6.33 ± 1.04 |

We used JKTEBOP code to determine the time of minimum ($Min I$) of SDSS J1021+1744. The best fitting model of SDSS J1021 +1744 for filter r' , g' , KG5, i' and $i'+z'$ are shown in Figure 4.1 - 4.5. The red dots and green line are the observed data and the calculation, respectively while the blue dots are the residuals.

Table 4.2 Result parameter of SDSS J1021+1744 from JKTEBOP code, the brackets shows the fixed parameter.

| Parameter | Value | | | | |
|--------------------|--------------|--------------|---------------------------------|--------------|--------------|
| | g' | KG5 | r' | i' | $i'+z'$ |
| Sum of frac radii | 0.3305 | 0.3604 | (0.3635) | (0.3635) | (0.3635) |
| Ratio of the radii | | | (31.0157) | | |
| Orbital | 78.7836 | 82.3429 | 81.7088 | 72.9144 | 74.6883 |
| Inclination | ± 0.1316 | ± 1.759 | ± 3.1736 | ± 0.3666 | ± 0.4749 |
| ecc * cos(omega) | 0.0278 | 0.230 | 0.0230 | (0.0230) | (0.0230) |
| ecc * sin(omega) | 0.0651 | 0.0539 | 0.0539 | (0.0539) | (0.0539) |
| Grav darkening A | | | (1.0000) | | |
| Grav darkening B | 0.9378 | -1.6316 | 0.7546 | 1.3732 | 7.4591 |
| | ± 4.8285 | ± 0.4847 | ± 2.5631 | ± 0.9189 | ± 0.6285 |
| Reflected light A | | | (0.0000) | | |
| Reflected light B | 1.0445 | 1.6614 | 2.1991 | -0.0398 | 3.7211 |
| | ± 1.1163 | ± 0.6297 | ± 1.1951 | ± 2.2166 | ± 0.0543 |
| Phot mass ratio | | | (0.6012) | | |
| Light scale factor | 4.1325 | 4.1392 | 4.3618 | 3.1645 | 2.6819 |
| | ± 0.0267 | ± 0.0547 | ± 0.0034 | ± 0.0004 | ± 0.0331 |
| Integration ring | | | (1.00000) | | |
| Orbital period | | | 0.1403587 | | |
| Primary star | | | Limb darkening law: square-root | | |
| Secondary star | | | Limb darkening law: linear | | |

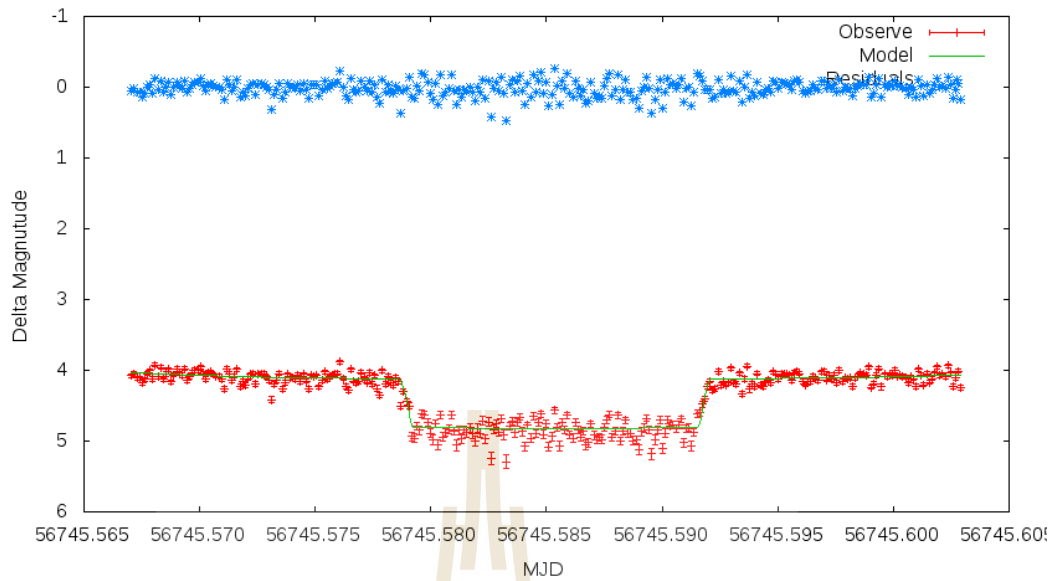


Figure 4.1 Model with JKTEBOP code on 29 Mar 2014 (Filter r').

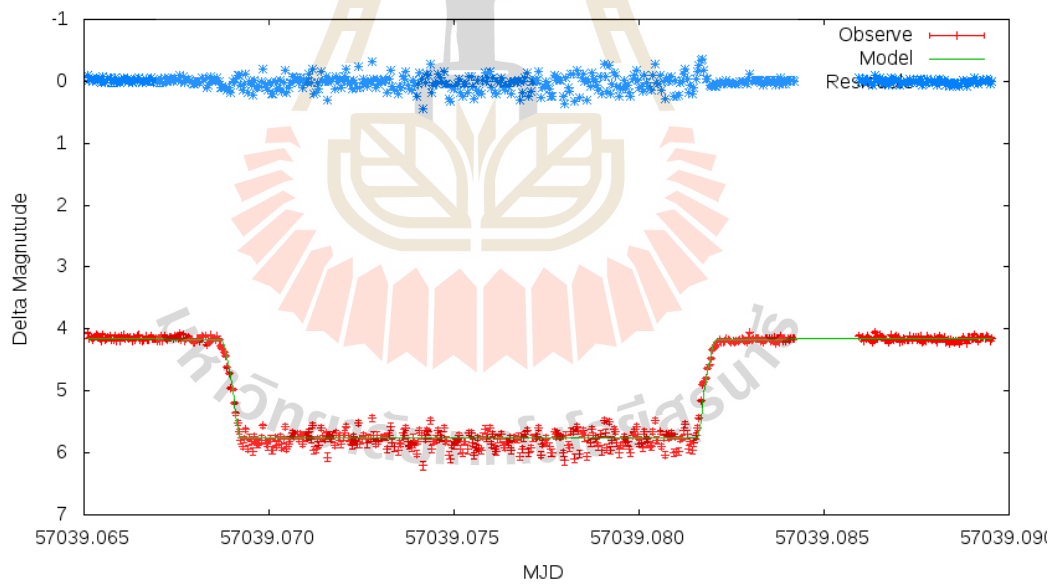


Figure 4.2 Model with JKTEBOP code on 17 Jan 2015 (filter g') from WHT. On that day one of the dip close to primary eclipse, so we have to cut around MJD 57039.085.

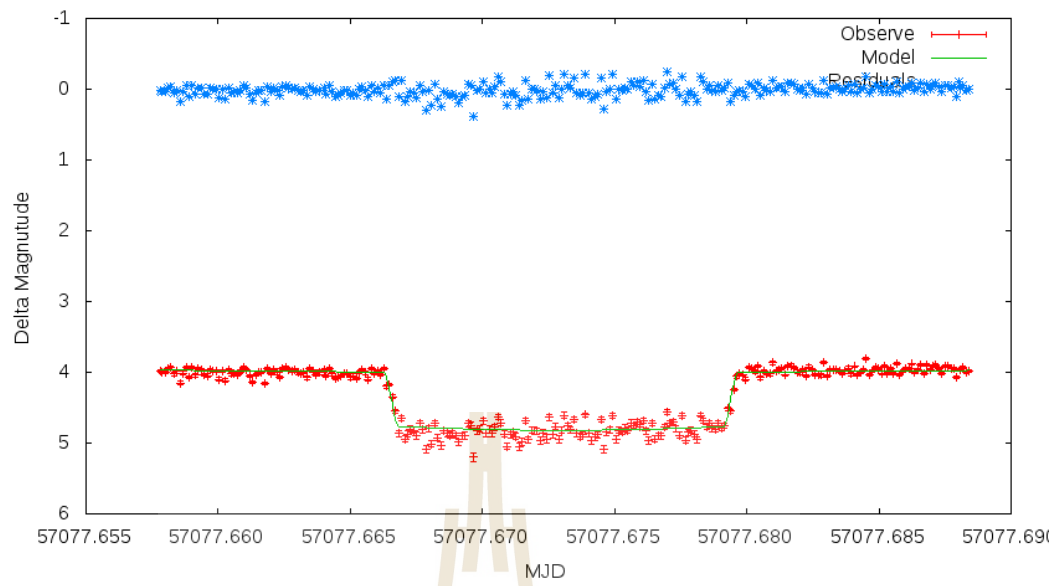


Figure 4.3 Model with JKTEBOP code on 24 Feb 2015 (filter KG5).

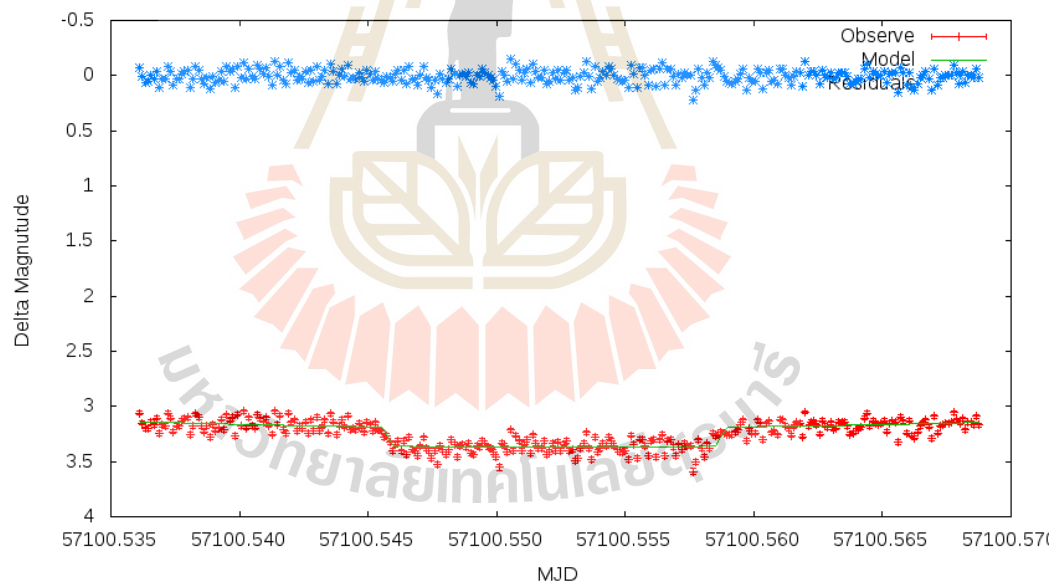


Figure 4.4 Model with JKTEBOP code on 15 Mar 2015 (filter i').

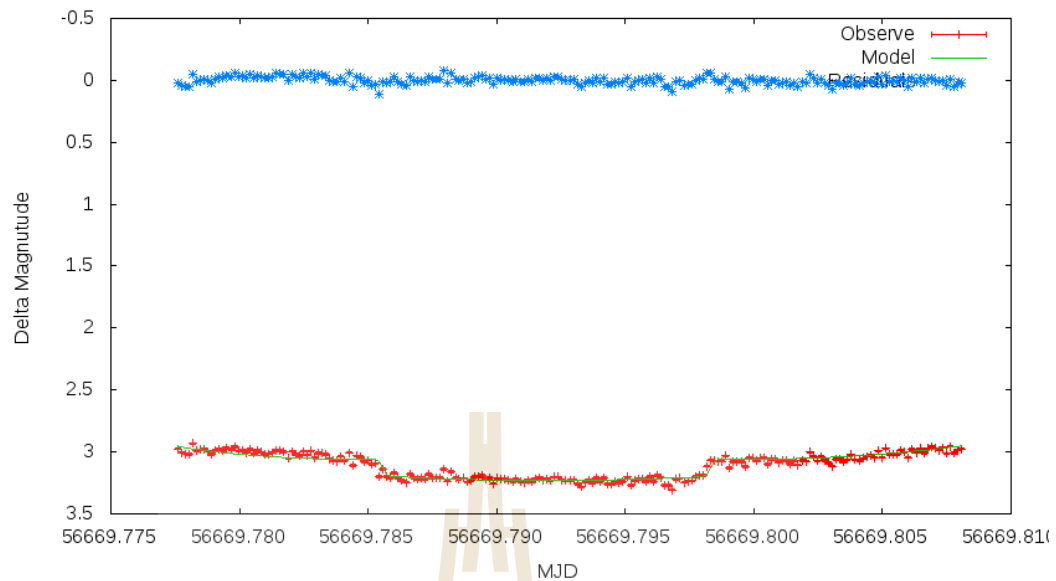


Figure 4.5 Model with JKTEBOP code on 12 Jan 2014 (filter $i'+z'$).

We show the time of mid-eclipse for O-C diagram in Table 4.1 and model fitting light curve and residuals in Figure 3.20.

4.1.2 The O-C diagram

We used JKTEBOP code to find the mid-eclipse time of observation (O), new ephemeris (T_0) and O-C have been calculated. We can determine the relation between O-C versus epoch as the following diagram in Figure 4.6. The appearance of the O-C diagram is strongly dependent on the ephemeris Equation (4.1) which is used for constructing it. The calculated time of the primary minimum is given by a linear relation:

$$C = 56664.88447 + 0.140358735 \times E \quad (4.1)$$

We can obtain the new orbital period of SDSS J1021+1744 is 0.140358735 days and in Figure 4.6, the O-C diagram is presented. Figure 4.6 shows the O-C diagram of SDSS J1021 +1744 compared between our calculation (black

dots) and Irawati's calculation (Irawati et al., 2016). We used the observed data since 7 January 2014 to 10 January 2016 with the orbital period of 0.140358735 days.

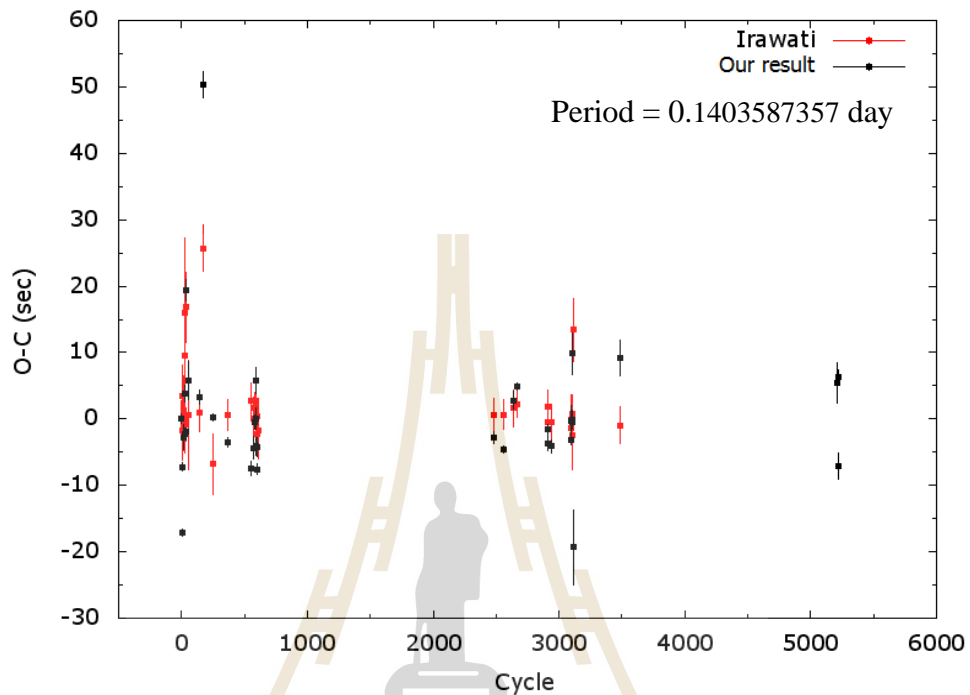


Figure 4.6 The O-C diagram of SDSS J1021+1744 using JKTEBOP code

4.1.3 The modeling using PHOEBE

The selected of the observational data in g' , $KG5$, r' and i' filters are used for modeling by using PHOEBE. The light curves with the best fitting and the residuals of SDSS J1021 +1744 are shown in Figure 4.7 and we presented the phase orientations of SDSS J1021+1744 in Figure 4.8. The parameter values from of SDSS J1021+1744 using PHEOBE are shown in Table 4.3 and Table 4.4 shows the result parameter and the best fit parameter respectively from PHOEBE.

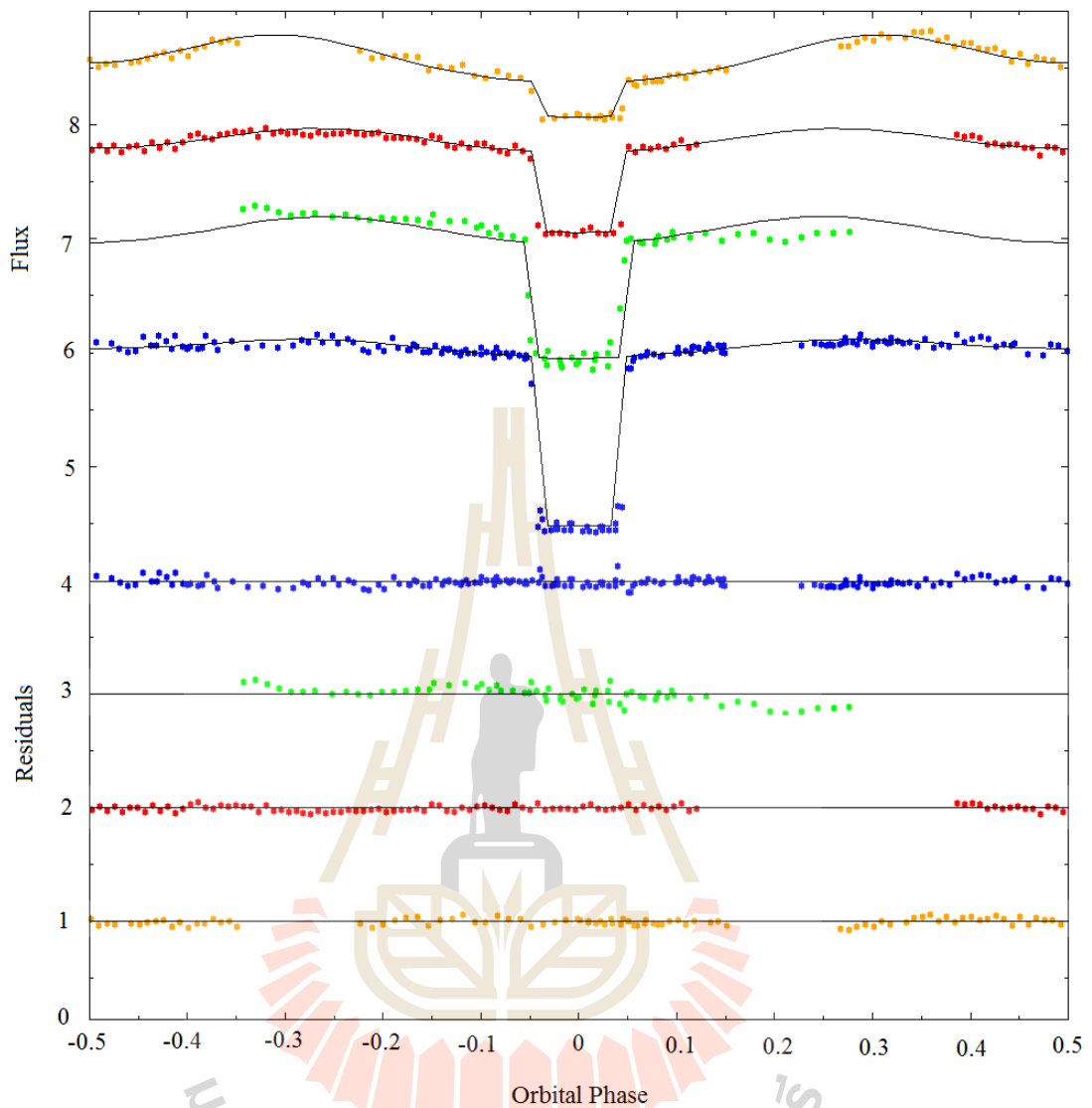


Figure 4.7 Top: The light curves of the eclipse of the white dwarf-main sequence star in SDSS J1021+1744, flux calibrated ULTRASPEC in g' , KG5, r' and i' filters (blue, green, red and orange points) with PHOEBE model fit over plotted (black lines).we can see the ellipsoid variation of the pattern of light curve. Bottom: The four panels show the residuals of the fit in g' filter (blue points). KG5 filter (green points), r' filter (red points) and i' filter (orange points).

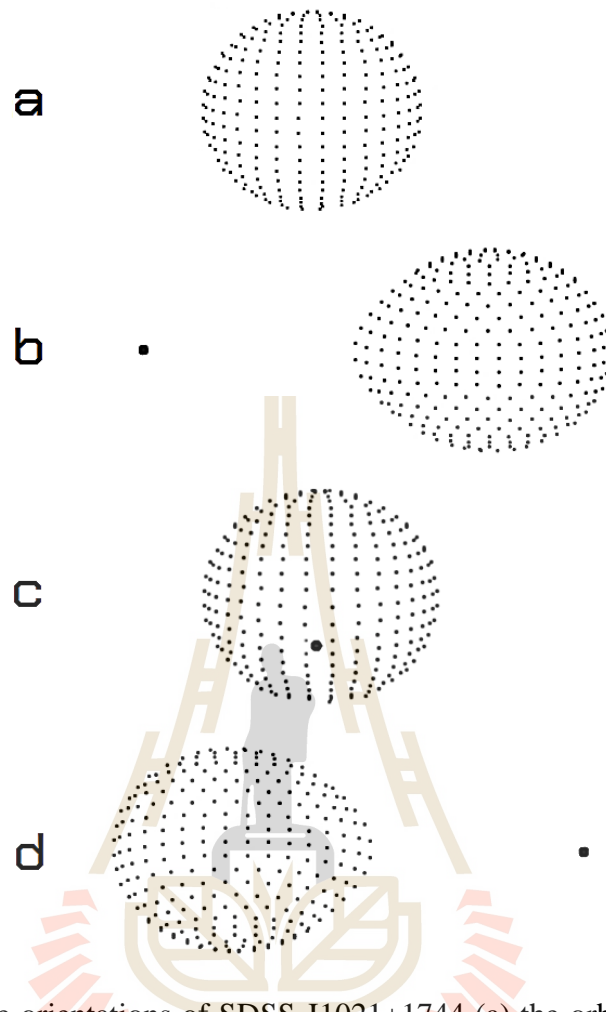


Figure 4.8 Phase orientations of SDSS J1021+1744 (a) the orbital phase 0.00 from the back side of the main-sequence star. (b) At the orbital phase, 0.25 show the bigger one is a main-sequence star from a side view. A shape of the main-sequence star looks like water drops; as a size of main-sequence is closer fill its Roche lobe. (c) At the orbital phase 0.50, from a front of the main-sequence star, a black tiny is the white dwarf star and this phase shows the white dwarf passes in front of the main-sequence. and (d) at the orbital phase 0.75, from another side of main-sequence star compare with the white dwarf star but opposite position of orbital phase 0.25.

Table 4.3 System parameter of SDSS J1021+1744 using PHOEBE.

| Parameter | g' | KG5 | r' | i' |
|----------------------|----------|----------|----------|----------|
| $\Omega (L_1)$ | 3.065399 | 3.064999 | 3.064306 | 3.062132 |
| $\Omega (L_2)$ | 2.713778 | 2.713491 | 2.712992 | 2.711429 |
| $M_{WD} [M_{\odot}]$ | 0.5001 | 0.5000 | 0.5000 | 0.5003 |
| $M_{MS} [M_{\odot}]$ | 0.3005 | 0.3006 | 0.3004 | 0.3005 |
| $R_{WD} [R_{\odot}]$ | | 0.01197 | | |
| $R_{MS} [R_{\odot}]$ | 0.348478 | 0.34867 | 0.34842 | 0.348177 |

Table 4.4 The best fit model from PHOEBE of SDSS J1021+1744.

| Parameter | g' | KG5 | r' | i' |
|--------------------------|------------------|------------------|------------------|------------------|
| Mass ratio | $0.6011 \pm$ | $0.6009 \pm$ | $0.6007 \pm$ | $0.599 \pm$ |
| | 0.0008 | 0.002 | 0.001 | 0.002 |
| Inclination | 81.19 ± 0.05 | 80.45 ± 0.08 | 81.41 ± 0.08 | 81.23 ± 0.18 |
| WD T_{eff} | 19545 ± 405 | 14137 ± 3978 | 17000 ± 283 | 20985 ± 110 |
| MS T_{eff} | 3180 ± 49 | 3202 ± 457 | 3180 ± 49 | 3185 ± 13 |
| WD surface | - | - | - | - |
| albedo | - | - | - | - |
| MS surface | 0.77870 | 0.7746 | 0.77253 | 0.82593 |
| albedo | 0.77870 | 0.7746 | 0.77253 | 0.82593 |
| R_{WD} [R_{\odot}] | 0.011970 | 0.011970 | 0.011970 | 0.011970 |
| R_{MS} [R_{\odot}] | 0.348666 | 0.348666 | 0.348666 | 0.348666 |
| WD T_{eff} [K] | 19651 ± 286 | 14056 ± 3870 | 17000 ± 273 | 21253 ± 111 |
| MS T_{eff} [K] | 3173 ± 54 | 3184 ± 414 | 3182 ± 48 | 3164 ± 13 |

4.1.4 Binary Maker software

The light curves of SDSS J1021 +1744 with the best fitting using BM3 in each filters is shown in Figure 4.9. From the light curve using Binary Maker 3.0, we can find the main sequence mass to be $0.301M_{\odot}$, mass ratio is 0.601, the temperature of the white dwarf is 17000 ± 2000 K, the main sequence's temperature is 3115 ± 200 K, and the system's inclination is 81.5 degree. The radial velocity measurements of the Na I 8200Å absorption doublet reported by Rebassa-Mansergas et al. 2012, allowed us to measure the radial velocity amplitude. The radial velocity of main-sequence star and a systemic velocity are $K_{\text{sec}} = 235 \pm 9$ kms-1 and $V_0 = -20 \pm 6$ kms-1, respectively. The mass of white dwarf is $0.5M_{\odot}$ as shown in Table 4.5.

In BM3, this software can input initial parameters such as the radial velocity and the systemic velocity. From Figure 4.9, the light curves of the whole period in g' and r' filters are shown. For model fitting, we have to block the dips between phase 1.15 to 1.25 in every filters because BM3 can not generate the light curve with dips. After that, we obtain the result from BM3 as shows as in Table 4.5.

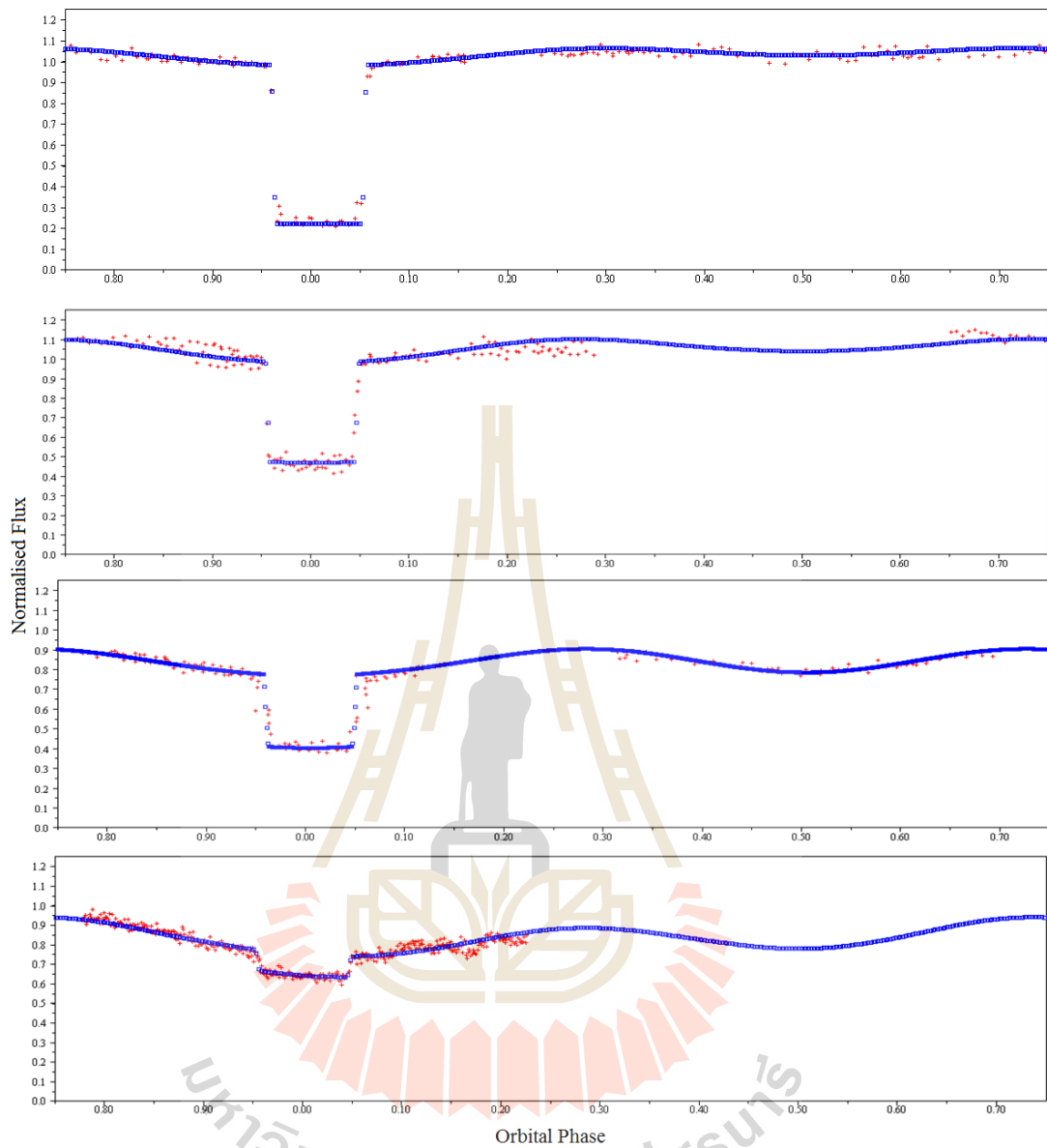


Figure 4.9 The result of the best fit light curve model of SDSS J1021+1744 in each filters, g' on the top, KG5, r' and the last one is $i'+z'$.

Table 4.5 SDSS J1021+1744 output from Binary Maker 3.0 with SDSS filters.

| Parameter | g' | r' | $i'+z'$ | KG5 |
|---------------------------------|--------|--------------|---------|--------|
| Mass ratio | | | | |
| | | 0.60112 | | |
| $[M_{MS}/M_{WD}]$ | | | | |
| Omega 1 | | 88.68052 | | |
| Omega 2 | | 3.089792 | | |
| Omega inner | | 3.065488 | | |
| Omega outer | | 2.713843 | | |
| Mean radius WD | | 0.011353 | | |
| Mean radius MS | | 0.329603 | | |
| Lagrangian L1 | | 0.552154 | | |
| Lagrangian L2 | | 1.613352 | | |
| Mass WD [M_{\odot}] | | 0.505673 | | |
| Mass MS, M_{\odot} | | 0.303968 | | |
| Eccentricity | | 0.00 | | |
| Semi-major axis [R_{\odot}] | | 1.057535 | | |
| Inclination[$^{\circ}$] | | 81.50 | | |
| R_{WD} [R_{\odot}] | 0.0122 | 0.0119 | 0.0122 | 0.0127 |
| R_{MS} [R_{\odot}] | 0.3447 | 0.3444 | 0.3447 | 0.3395 |
| WD T_{eff} [K] | 18800 | 18841 | 15000 | 17070 |
| MS T_{eff} [K] | 3174 | 3140 | 3000 | 3231 |
| P_{orb} [days] | | 0.1403587435 | | |

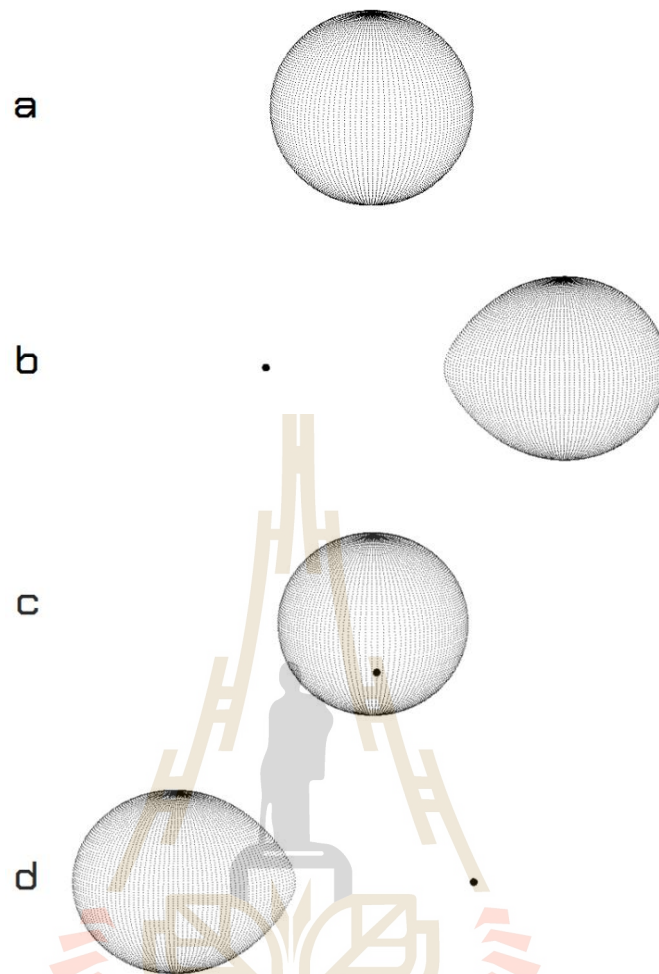


Figure 4.10 Phase orientations of SDSS J1021+1744 using BM3 value.

Figure 4.10 represents (a) the orbital phase 0.00 from the back side of the main-sequence star. (b) At the orbital phase, 0.25 show the bigger one is a main-sequence star from a side view. A shape of the main-sequence star looks like water drops; as a size of main-sequence is closer fill its Roche lobe. (c) At the orbital phase 0.50, from a front of the main-sequence star, a black tiny is the white dwarf star and this phase shows the white dwarf passes in front of the main-sequence. and (d) at the orbital phase 0.75, from another side of main-sequence star compare with the white dwarf star but opposite position of orbital phase 0.25.

4.2 Dips in SDSS J1021+1744

The light curve shows the relation between orbital phase and normalized flux which we used the new ephemeris, orbital period and normalized flux scale. The baseline of all light curves around orbital phase 0.05 to 0.105 are set at 1 because all the light curves have that phase and set 0 from the middle of primary eclipse for normalized scale. In order to see the depth change of the dips, we compared the data based on the brightness of mid-eclipse. In 2014, we had observed SDSS J1021+1744 start from 7 January to 2 April in Figure 4.11. We had obtained the light curve in 17 cycles and found the maximum of dips During May and April. In Figure 4.12, we had obtained the light curve in 15 cycle starts from 22 December 2014 to 10 January 2016.

For the example of the model, the position of two dips in 7 Jan 2014 which is determined at orbital phase of 1.13 to 1.17 is shown in Figure 4.13 and we have changed the coordinates from orbital phase to angle in order to represent the Roche geometry model of SDSS J1021+1744 as shown in Figure 4.14.

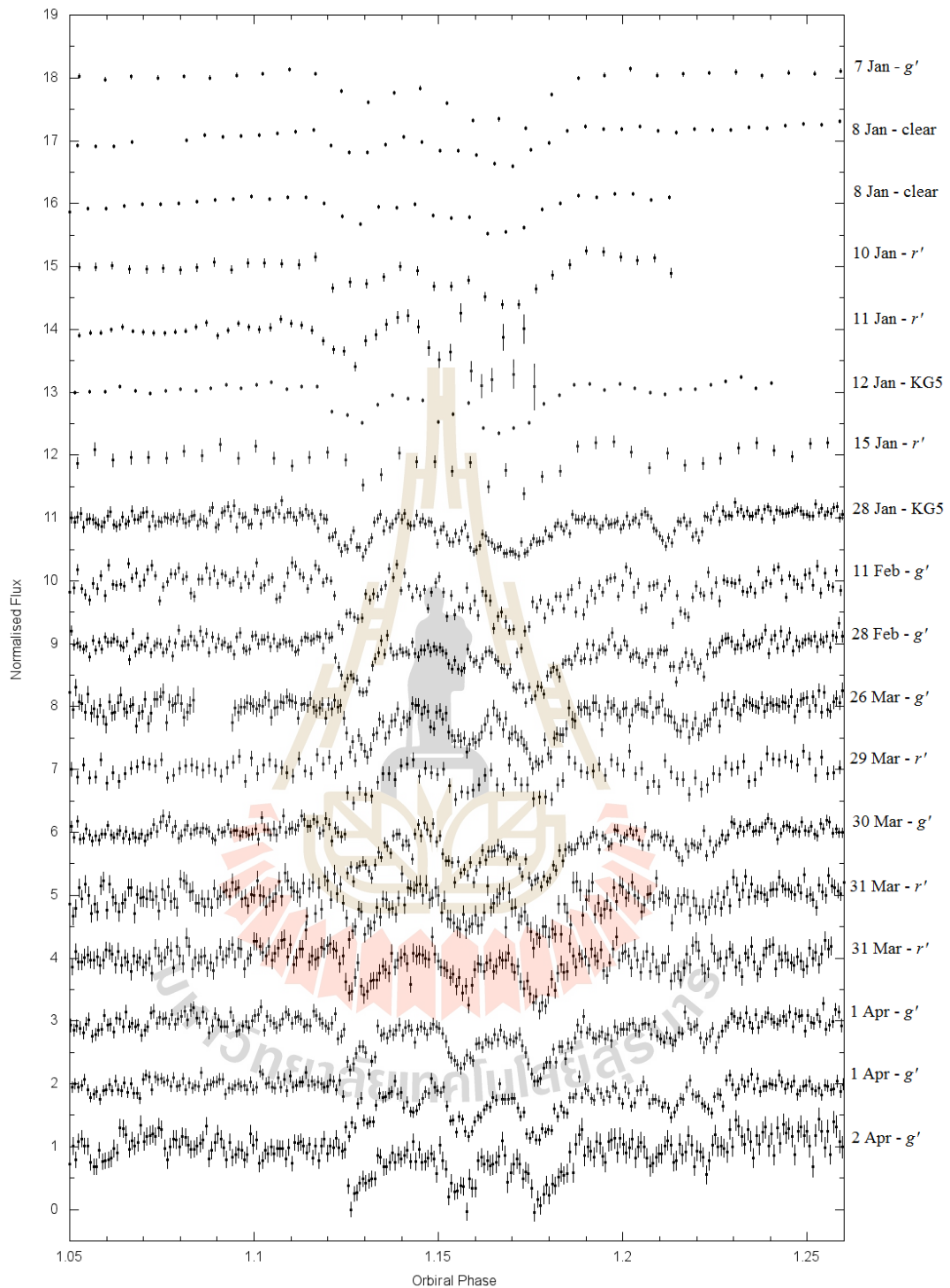


Figure 4.11 The light curve of SDSS J1021+1744 in 2014 with close up between orbital phases 1.05 to 1.26. This light curves are set the oldest light curve on the top and the newest on bottom.

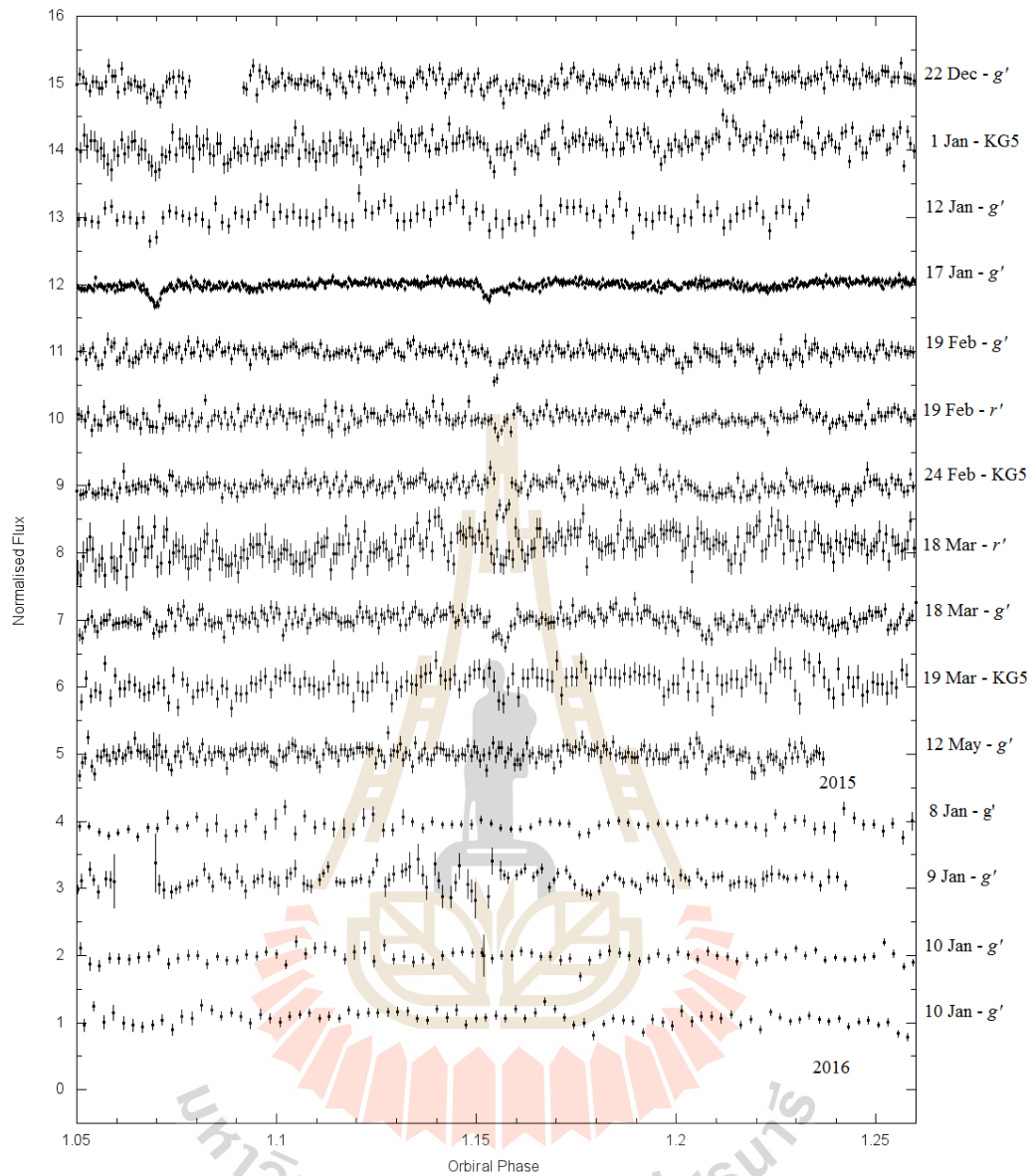


Figure 4.12 The data obtained in 2015 and 2016. We can see only one or two dips in light curves.

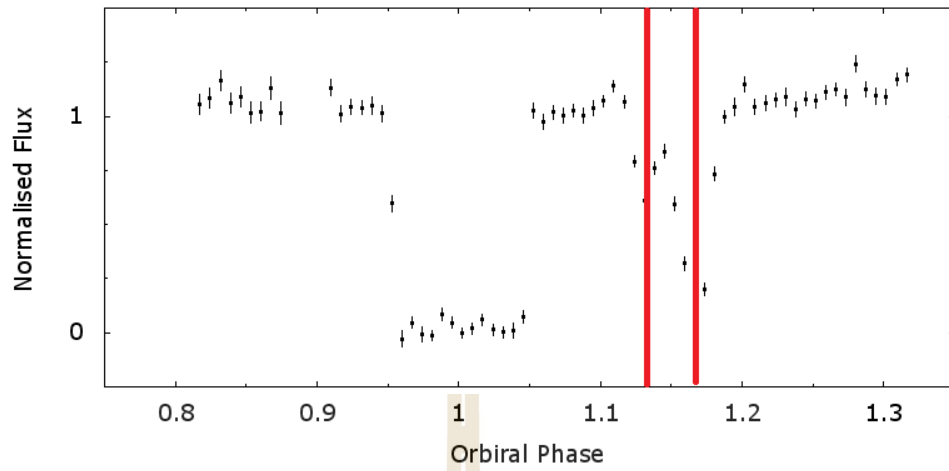


Figure 4.13 The position of two dips at orbital phase 1.13 and 1.17.

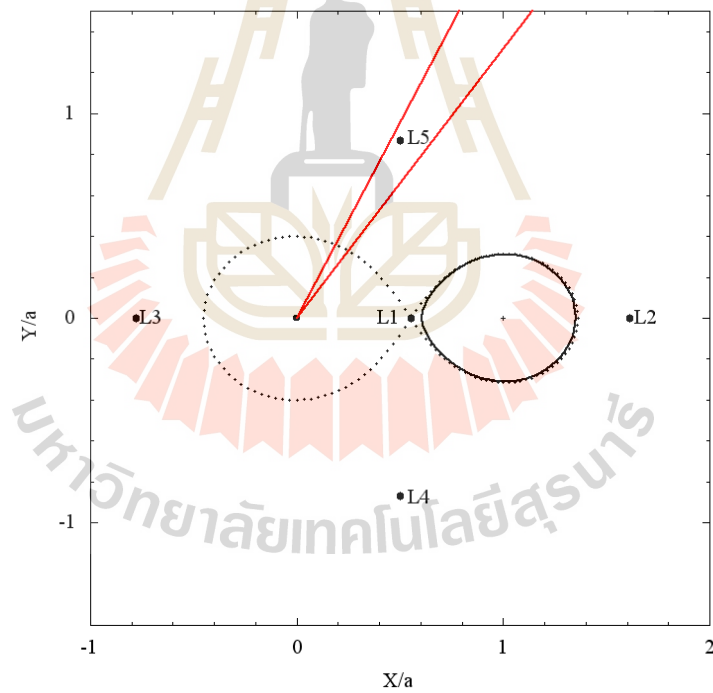


Figure 4.14 On 7 January 2014, the Roche geometry of SDSS J1021+1744 with two dips position on the orbital phase of this system. The straight lines are indicated by the line of sight from the white dwarf.

Finally, we compared all the parameters of SDSS J1021 +1744 which are obtained from the calculation, BM 3, PHOEBE and JKTEBOP code as shown in Table 4.6. And compared our results with Parsons et al., 2013, Irawati et al., 2016 and Parsons et al., 2017 as presented in Table 4.7. Our results are quite similar to Irawati's calculation.

Table 4.6 Result parameter of SDSS J1021+1744 from calculation and modeling with BM3 and PHOEBE and JKTEBOP code in r' filter.

| Parameter | Value | | | |
|-----------------|---------------------|---------------------|---------------------|----------|
| | Calculation | BM3 | PHOEBE | JKTEBOP |
| Mass ratio | 0.600112 | 0.60112 | 0.6005 ± 0.07 | 0.060112 |
| Omega 1 | 88.6836 | 88.680530 | 88.68052 | 88.68052 |
| Omega 2 | 4.82107 | 3.089790 | 3.08979 | 3.08979 |
| Omega inner | 3.0654876 | 3.065488 | - | - |
| Omega outer | 2.7138426 | 2.713843 | - | - |
| Radius back WD | $0.011353R_{\odot}$ | $0.011353R_{\odot}$ | - | - |
| Radius side WD | - | $0.011353R_{\odot}$ | $0.011970R_{\odot}$ | - |
| Radius pole WD | $0.011353R_{\odot}$ | - | - | - |
| Radius point WD | $0.011353R_{\odot}$ | - | - | - |
| Radius back MS | $0.352117R_{\odot}$ | $0.354160R_{\odot}$ | $0.348666R_{\odot}$ | - |
| Radius side MS | - | $0.324056R_{\odot}$ | - | - |
| Radius pole MS | $0.310599R_{\odot}$ | $0.310599R_{\odot}$ | - | - |
| Radius point MS | $0.399436R_{\odot}$ | $0.405744R_{\odot}$ | - | - |
| Mean radius WD | $0.011353R_{\odot}$ | $0.011353R_{\odot}$ | - | - |

Table 4.6 Result parameter of SDSS J1021+1744 from calculation and modeling with BM3 and PHOEBE and JKTEBOP code in r' filter (Continued).

| Parameter | Value | | | |
|-----------------|------------------------|---------------------|----------------------------------|--------------------------------|
| | Calculation | BM3 | PHOEBE | JKTEBOP |
| Mean radius MS | $0.331618R_{\odot}$ | $0.329605R_{\odot}$ | - | - |
| Lagrangian, L1 | 0.552154 | 0.552154 | - | - |
| Lagrangian, L2 | 1.613352 | 1.613352 | - | - |
| Lagrangian, L3 | -0.7772555 | - | - | - |
| Lagrangian, L4 | 0.500, 0.866 | - | - | - |
| Lagrangian, L5 | 0.500, -0.866 | - | - | - |
| Center of Mass | 0.3754356 | - | - | - |
| Mass WD | $0.5000 M_{\odot}$ | - | - | - |
| Mass MS | $0.3006M_{\odot}$ | $0.3039M_{\odot}$ | - | - |
| Semi-major axis | $1.0554R_{\odot}$ | $1.0575R_{\odot}$ | $1.0542R_{\odot}$ | - |
| Inclination | 81.5° | 81.5° | $81.07^{\circ} \pm 0.55^{\circ}$ | $80.0^{\circ} \pm 6.9^{\circ}$ |
| Period (days) | 0.140358 ± 0.00001 | | | |

From Table 4.6, we can see that the results parameters of SDSS J1021+1744 are the good best fitting in r' filter with the chi-square of 0.0193 by using PHOEBE.

Table 4.7 The compared result of our model of SDSS J1021+1744 with the parameters from Parsons et al., 2013, Irawati et al., 2016 and Parsons et al., 2017.

| Parameter | Our result | Parsons (2013) | Irawati (2016) | Parsons (2017) |
|---------------------------------|----------------------------------|---------------------------|-------------------|---------------------|
| Observation | | Optical | | Spectral |
| $T_{0(BMJD)}$ | 56664.884453 ± 0.00001 | 56093.90558 | 56664.8843262 | - |
| Period (days) | 0.140358735 | 0.140359073 | 0.140358755 | 0.1403575 |
| MassWD (M_{\odot}) | 0.50 | 0.50 ± 0.05 | - | 0.534 ± 0.004 |
| Mass ratio, q | 0.60 | - | 0.5 | - |
| WD T_{eff} (K) | 17000 ± 273 | 32595 ± 928 | 17505 | 10644 ± 1721 |
| MS T_{eff} (K) | 3182 ± 48 | - | 3160 | - |
| Inclination, i | $81.07^{\circ} \pm 0.21^{\circ}$ | $75^{\circ} - 90^{\circ}$ | 85° | - |
| R_{WD} (R_{\odot}) | 0.0112 | - | 0.0116 | 0.0140 ± 0.0003 |
| R_{MS} (R_{\odot}) | 0.3488 | 0.320 ± 0.05 | 0.3572 | - |
| Chi-square | 0.012 | 0.289 | 0.117 | 0.142 |

CHAPTER V

DISCUSSIONS AND CONCLUSIONS

5.1 Discussions

We present our recent observations on SDSS J102102.25+174439.9, a new eclipsing white dwarf main sequence (WDMS) binary with an orbital period of 0.14 days. This system belongs to the post common-envelope binary group as shown by the spectrum from the Sloan Digital Sky Survey. SDSS J1021+1744 system are known to be the only WDMS to show this kind of dips in their light curve. It is possible that these dips are caused by the ejected materials from an active companion star, such as in QS Vir. On the Sun, the spots are generally not much bigger than Jupiter, and most of spots are far smaller. However on the M-type star, spots can be a much bigger fraction of the star's surface. The effect from gravitational darkening in closed binaries and the magnetic fields can be incredibly strong, which means that lots of energy be stored. Therefore, that energy can be dull vast when their stored energy is released. This might explain why the companion star in SDSS J1021+1744 system can produce such a huge and long lasting flare.

For studying the variations of unusual dips, we select the position of the light curves with the orbital phase between orbital phases 1.05 to 1.26. Then we counted the number of dips in each light curves.

This kind of dips have been reported before in QS Virginis light curve (O'Donoghue et al., 2003) as seen in Figure 5.1, the dip minima are at the same level

of the eclipse and they are certainly not the background noise so the effect cannot be explained (O'Donoghue et al., 2003). The system comprises an eclipsing white dwarf and red dwarf that orbit each other every 3.37 hours. QS Virginis or EC 13471-1258 is the eclipsing white dwarf and M dwarf binary system, discovered in the Edinburgh-Cape Blue Object Survey and O'Donoghue et al. (2003) provided an extensive study of the system. The system became detached as the result of an eruption, possibly caused by activity on the secondary M type star. A number of optical flares were observed which confirmed that the M star is magnetically active. There were two peculiar dips before the primary eclipse of QS Virginis.

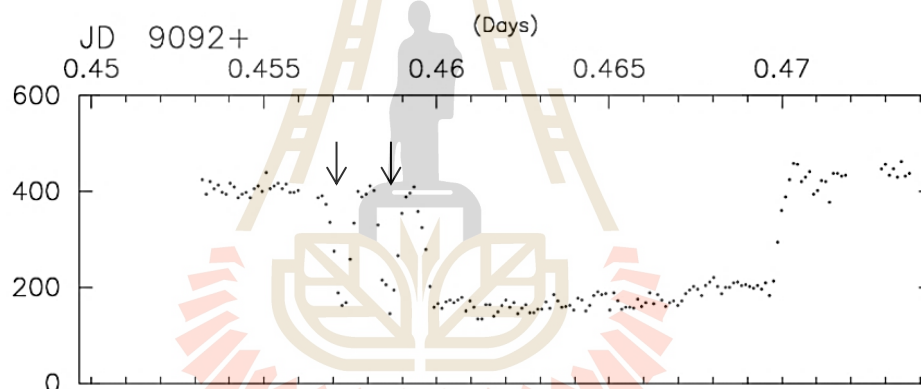


Figure 5.1 Shows two dips before the eclipse of QS Virginis.

The spectral type of QS Virginis is M3.5 that means the M dwarf (M-type star) is completely convective. It will certainly pass through a common envelope formation and may have undergone substantial mass loss through Roche lobe overflow. However, it might still be expected to find flares of the kind seen in chromospherically active M dwarfs (O'Donoghue et al., 2003). In 2011, the prominace in QS Virginis was detected and located close to L5 point (Parsons et al., 2011).

In 1986, Jensen et al. had observed the detached binary V471 Tauri using EXOSAT X-ray observatory, the dips were also reported to be at the similar location close to the L_4 and L_5 as shown in Figure 5.2.

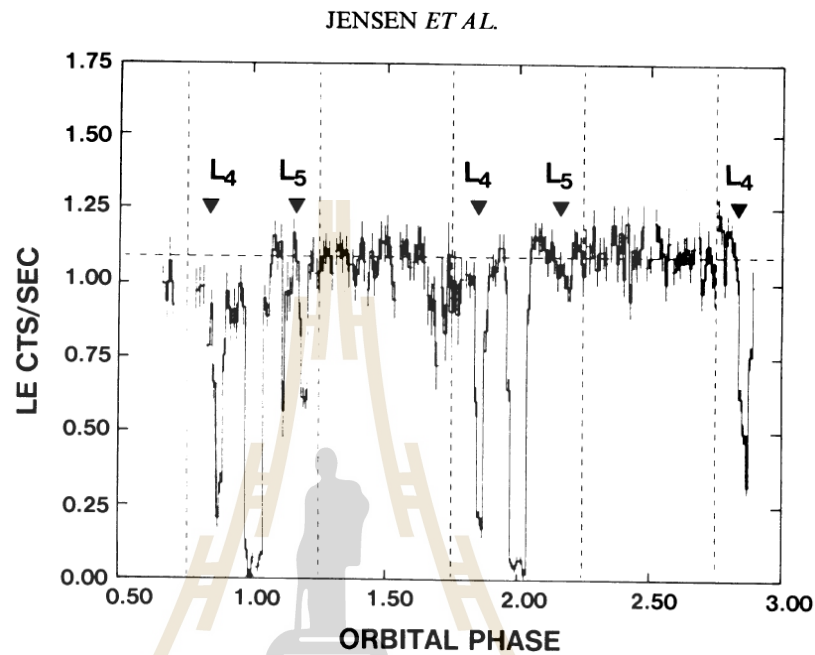


Figure 5.2 The light curve of the 0.03-2.5 keV flux from V471 Tauri. The phases at which the triangular Lagrangian points (L_4 and L_5) are in our line of sight to the white dwarf are indicated by the arrow, (Jensen et al., 1986).

In Figure 5.2, dips in soft X-ray flux at orbital phase 0.15, 0.18, and 0.85 can be seen in the light curve in occurred when the Lagrangian points of the binary orbit are near the line of sight to the white dwarf (Jensen et al., 1986). The line of sight to the white dwarf during the dips are illustrated in Figure 5.3 which shows the material located at phase 0.62-0.75 must be due to material located closer to the white dwarf than K star.

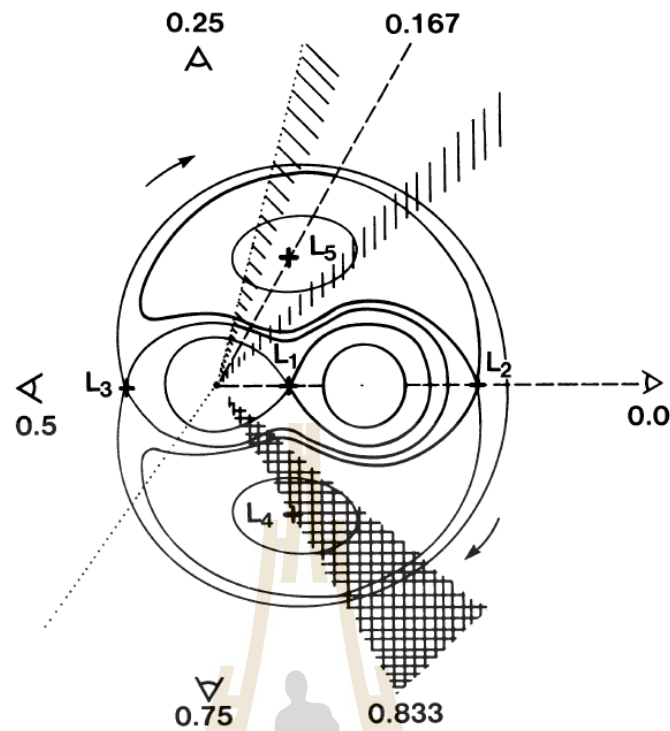


Figure 5.3 The schematic of V471 Tauri binary system with a mass ratio $q = 1$. Showing the location of five Lagrange points (L_1 to L_5), and the Roche geometry of equipotential, with respect to the white dwarf and K star. The shaded regions indicate the phases at which dips are seen. The dip near the L_4 point is unusual deep and persistent and is, therefore, more heavily shaded (Jensen et al., 1986).

Therefore in this study, we have to set the position of dip using number 1, 2, 3, 4 and 5 as indicated in Figure 5.4 and 5.5. We found the dips number 1 and 3 on 7 Jan to 15 Jan in g' , clear, r' and KG5 filters with exposure time about 1 minute. After that we change exposure time into 3 to 10 sec, 5 dips were observed in 2014 and mark sub of dip number 1 as 1a, 1b and 1c for small dips,. In 2015, we found two dips and cannot found any dips in 2016.

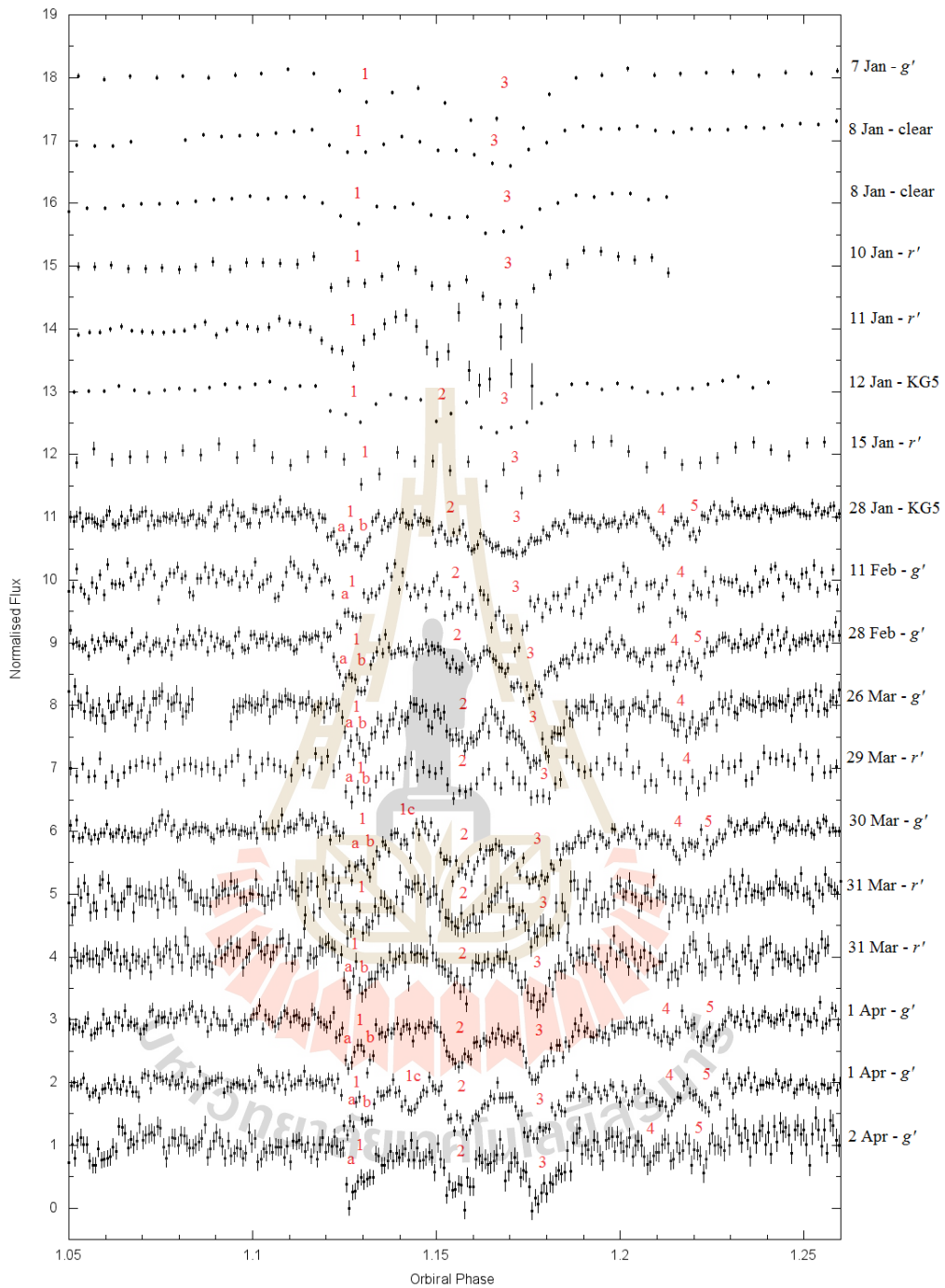


Figure 5.4 The light curve of SDSS J1021+1744 in 2014 with close up between orbital phases 1.05 to 1.26. This light curves are set the oldest light curve on the top and the newest on bottom.

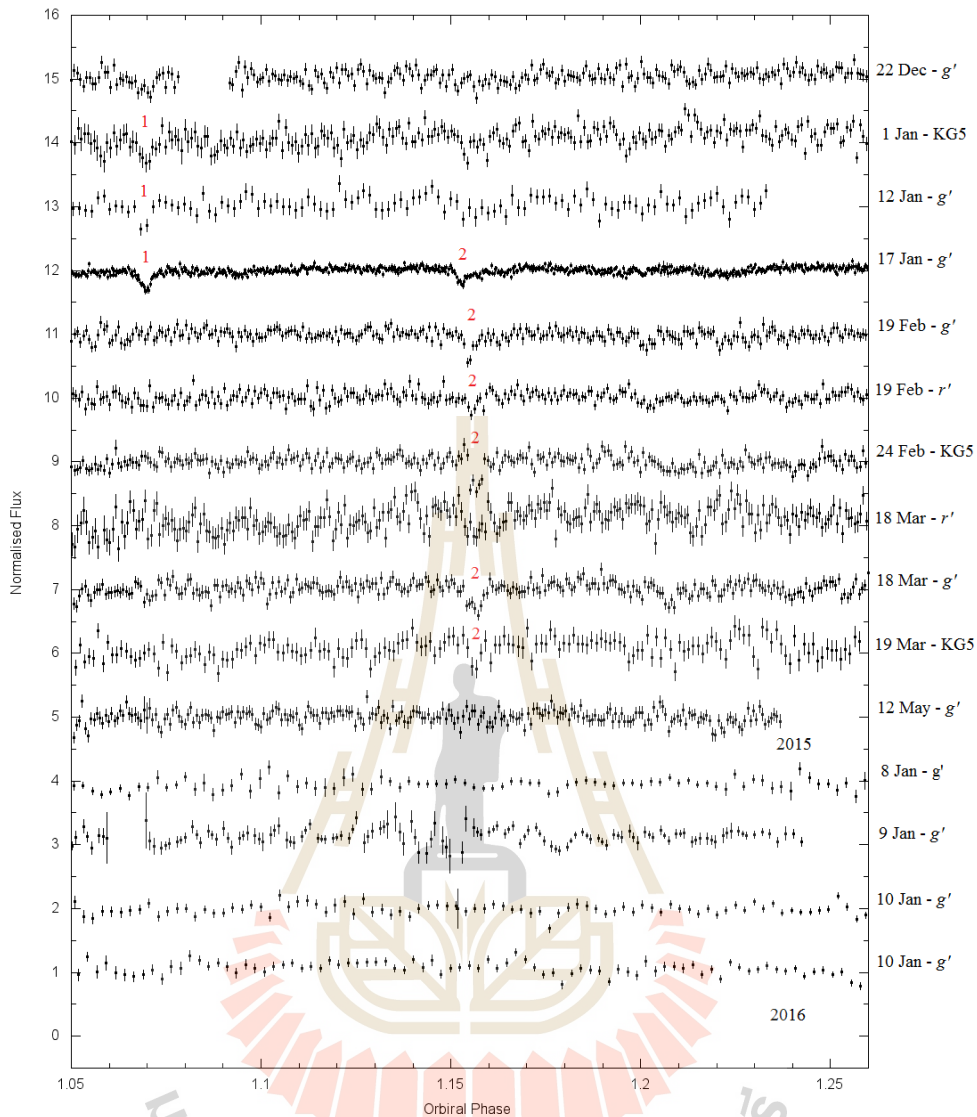


Figure 5.5 The light curve of SDSS J1021+1744 in 2014 with close up between orbital phases 1.05 to 1.26. This light curves are set the oldest light curve on the top and the newest on bottom.

In Figure 5.4 and 5.5, we marked the position of the dips from the light curve in 2014 to 2016 and then plot the lines of sight to the white dwarf during the dips which are presented in Figure 5.6 and 5.7. From the light curve, we can see that some dense material located along the line of sight is at the distance around 2 to 3 stellar radii

from red dwarf star. Five of dips at phases 0.13, 0.15, 0.18, 0.21 and 0.22 occurred 1 April 2014 and they were aligned near L_5 point which is illustrated in Figure 5.6.

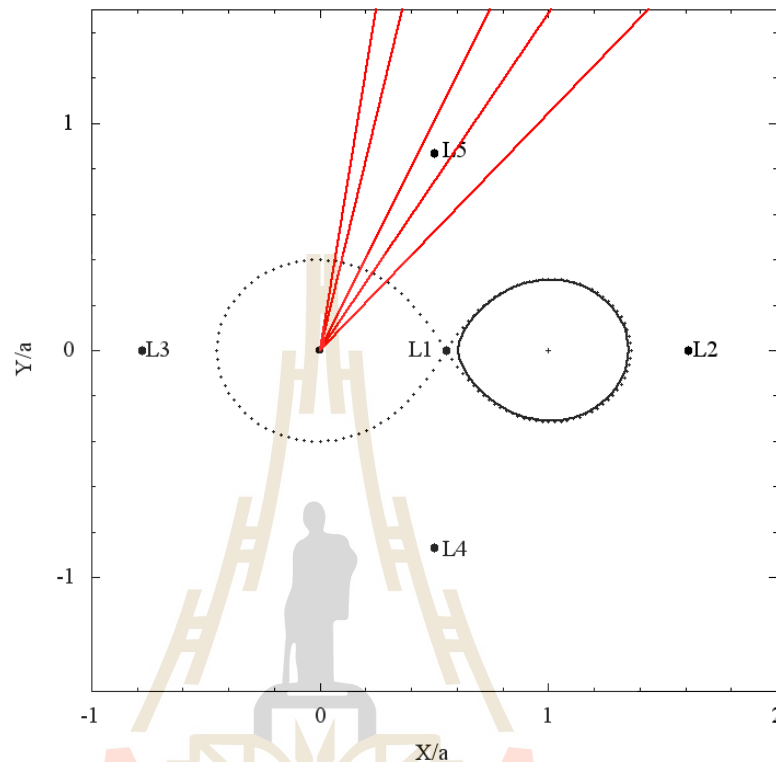


Figure 5.6 The Roche lobe inner potential geometry of SDSS J1021+1744, where the dips were seen on 1 April 2014 in g' filter. The dotted line is the Roche lobe potential, a black solid line is the red dwarf star. The red line shows the positions of the dips on orbital phase and all of dips are closer around the L_5 point.

At stability of L_4 and L_5 , while these points correspond to the local maxima of the generalized potential which are usually mean a state of unstable equilibrium but they are in fact stable. Their stability is due to the Coriolis force. Initially a mass situated near L_4 or L_5 will tend to slide down the potential, thus it picks up speed and the Coriolis force kicks in and sends it into an orbit around the Lagrangian point. The effect is analogous to how a hurricane form on the surface of the earth, when the L_4

and L_5 points yield stable orbits. The mass ratios in the earth-sun and earth-moon system are easily large enough for their L_4 and L_5 points to be home of Trojan satellites (Neil, 1998).

The L_5 point is at phase 0.167. It is possible that dense material ejected at this equipotential point (Jensen et al., 1986). On 19 February 2015, we found one dip at phase 0.15 is occurred near L_5 point in Figure 5.7.

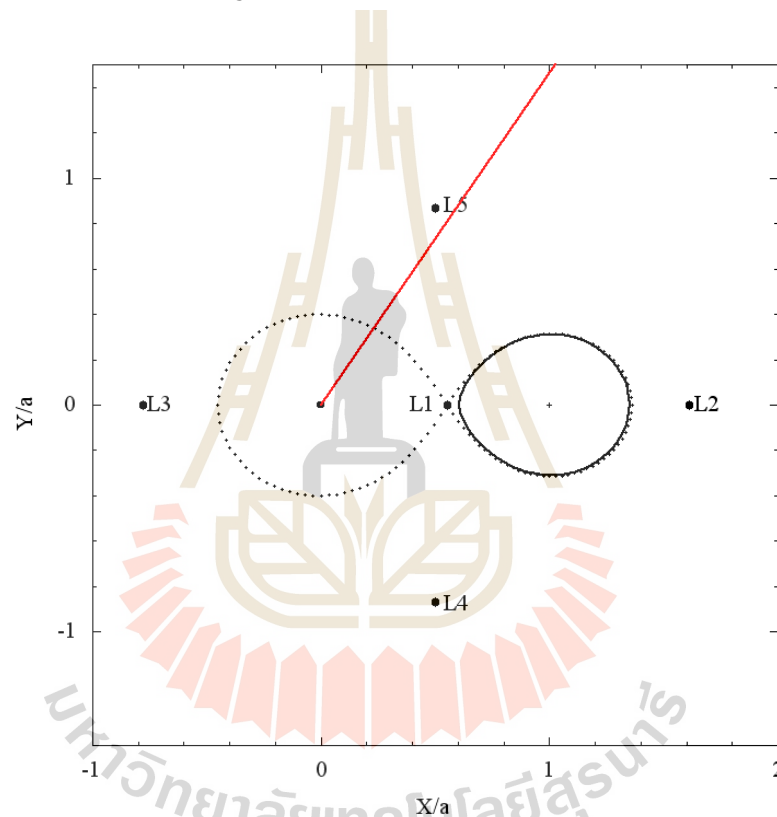


Figure 5.7 The Roche inner potential geometry of SDSS J1021+1744 with the dip.

We calculated the normalized flux at the position of dips (orbital phase) as shown in Figure 5.8. All the dips in 2014 are presented but in 2015, we found only 1 or 2 dips and in 2016, there is no dip.

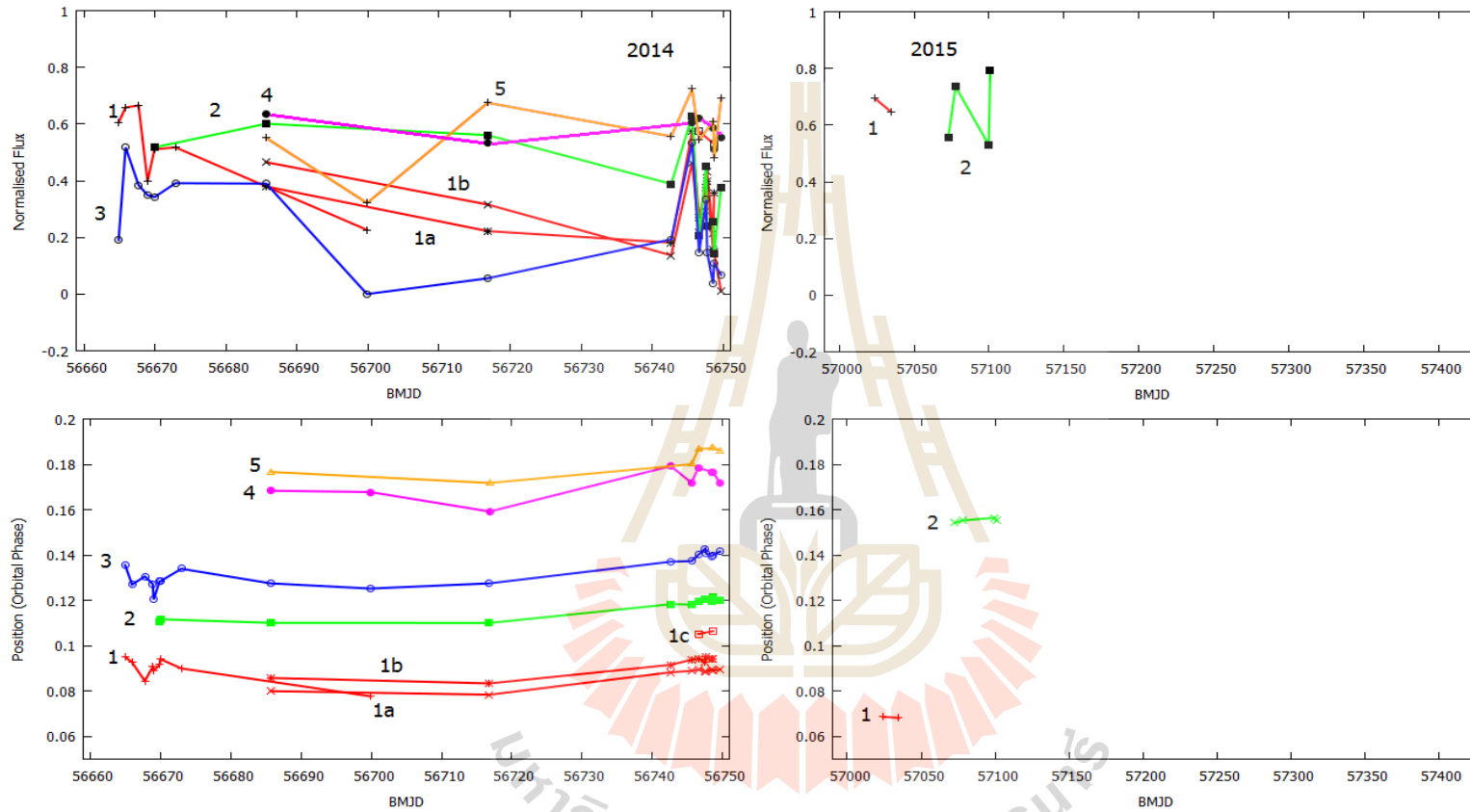


Figure 5.8 Top panels: show the normalized flux in each light curve in 2014 (left) and 2015 (right). Bottom panels: Show position of dips plot between orbital phase versus BMJD, we found maximum 5 dips in 2014, 2 dips in 2015 and in 2016, we cannot found any dips.

From Figure 5.8, we try to find the correlation from 28 January to 2 April 2014, because we got data almost 3 months with exposure times are 3 to 12 sec but we used long exposures time about 30 to 60 sec during 7 to 15 January 2014. The correlation coefficient between -1 and +1 indicate two variables are strongly related to each other. If a correlation coefficient of +1 indicates a perfect positive correlation. But if a -1 indicates a perfect negative correlation. And the correlation coefficient of zero indicates that there is no correlation at all. The correlation coefficients between the normalized flux and the time and the position of orbital phase and the time are presented in Table 5.1. The correlation of the dips position has changed significantly. For demonstrating the change in phase position, we select one of example: dip number 3 as shown in Figure 5.9. Show the position had changed diffusing during the end of January to the beginning of April in 2014. We found that the position of the dipping number 3 was moving out of Lagrangian L_5 point.

5.2 Conclusions

This is the first time that the dips have been observed for a few years. SDSS J1021+1744 is different from QS Virginis (O'Donoghue et al., 2003). The dips of QS Virginis were found only once, while in the SDSS J1021+1744 seems to be a permanent feature. The appearance of two short, but deep dips before the main eclipse in QS Virginis suggests that they are caused by flares or prominence from the main sequence star. And in V471 Tau (Jensen et al., 1986), which was observed in x-ray soft band and found dips at locations close to the L_4 and L_5 points, like material pass in front of white dwarf. Also, the peculiar dips of SDSS J1021+1744 are a possibility

that some materials from the prominence on the secondary passing in front of the white dwarf (Parsons et al., 2013).

Over 3 years of the unusual dips observations SDSS J1021+1744 are possibly caused by some dense materials from the prominence on the red dwarf passing in front of the white dwarf. These dips are located near the Lagrange L_5 point (Jensen et al., 1986) (Irawati et al., 2016). The object near Lagrangian point or Trojan object is a type of co-orbital object. In this arrangement, the massive star and the smaller star orbit around their common barycenter. A group of dense material of SDSS J1020+1744 located close to L_5 points which are subject to a combined gravitation

Table 5.1 Shows correlation between normalized flux and the time, and the position of orbital phase and the time from 28 Jan to 2 Apr 2014.

| Correlation | | |
|-------------|-----------------|-------------------|
| Dip | Normalized Flux | Position of Phase |
| 1a | -0.22 | 0.99 |
| 1b | -0.29 | 0.98 |
| 1c | -1.00 | 1.00 |
| 2 | -0.51 | 0.98 |
| 3 | -0.20 | 0.95 |
| 4 | 0.29 | 0.84 |
| 5 | -0.31 | 0.93 |

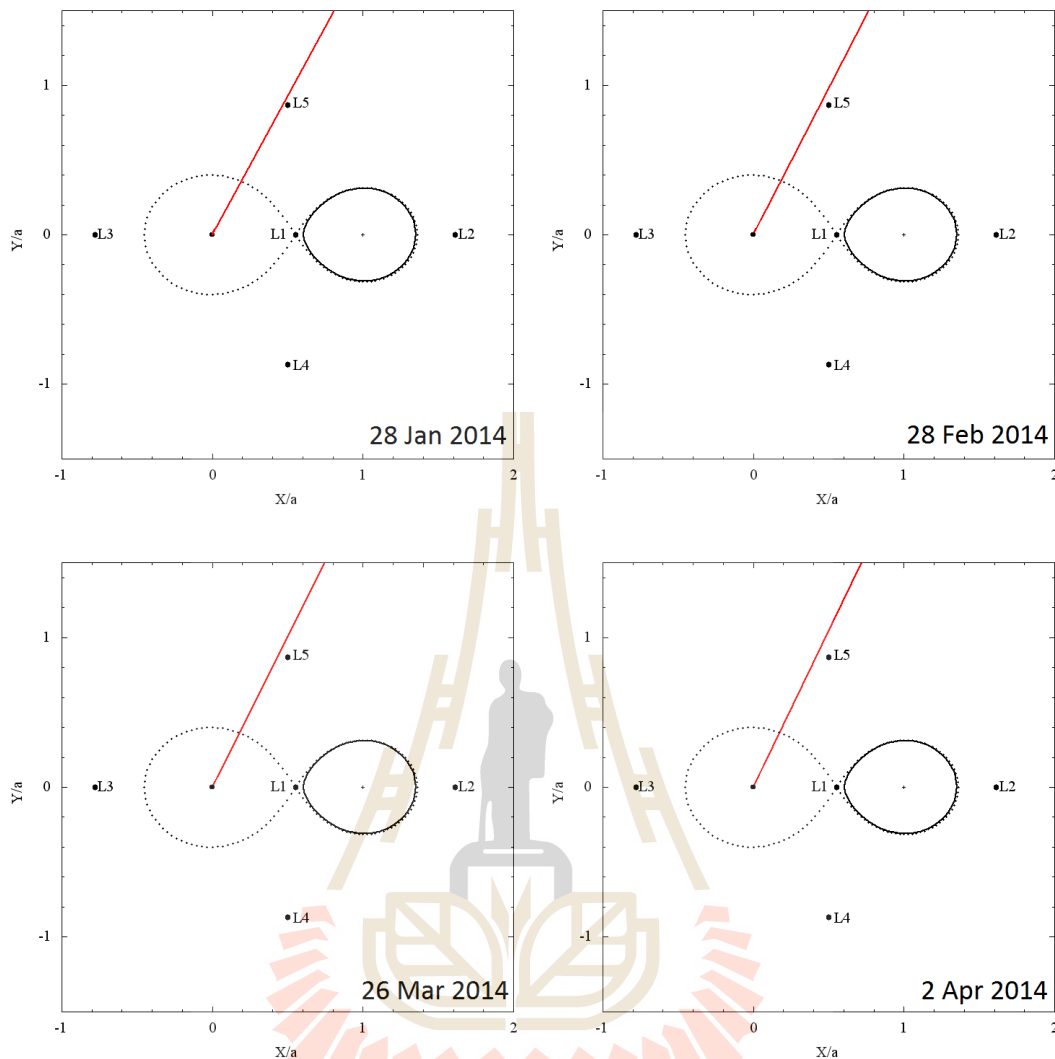


Figure 5.9 Show the dip number 3 on 28 Jan, 28 Feb, 26 Mar and 2 Apr, 2014. We can see the dip number 3 was moving which might be due to the dip was diffusing.

that acts through this barycenter. Hence the object can orbit around the barycenter with the same orbital period as the red dwarf star, the arrangement can remain stable over time and it is stable enough to have some material or asteroid around L_4 and L_5 point. In the future, there is possible to found the dips again at the Trojan points L_4 or both.

On 31 March 2014, we found a significant brightening around phase 0.7 on light curve of SDSS J1021+1744 (in Figure 5.10 and 5.11). The bright appeared two times of normalized flux and fade back within a few minutes. This is interpreted as a flare from the red dwarf, pointing to significant chromospheres' activity on main-sequence (Irawati et al., 2016). Whether such active behavior is partly responsible for mass ejections, which could funnel material to the observed dip positions, is an interesting possibility.

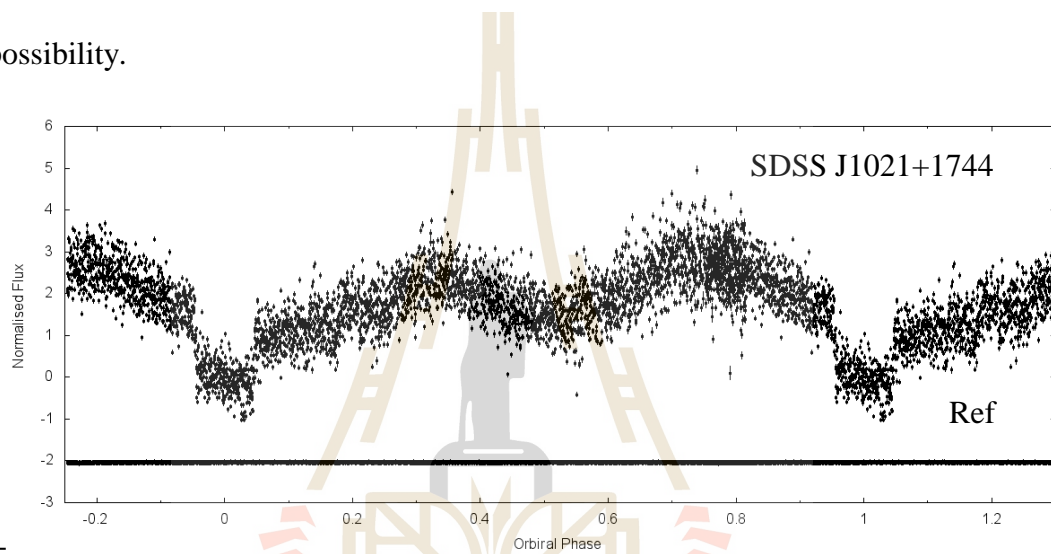


Figure 5.10 Light curve of SDSS J1021+1744 and reference star in i' filter on 30 Jan 2014, shows ellipsoidal modulation but only that date.

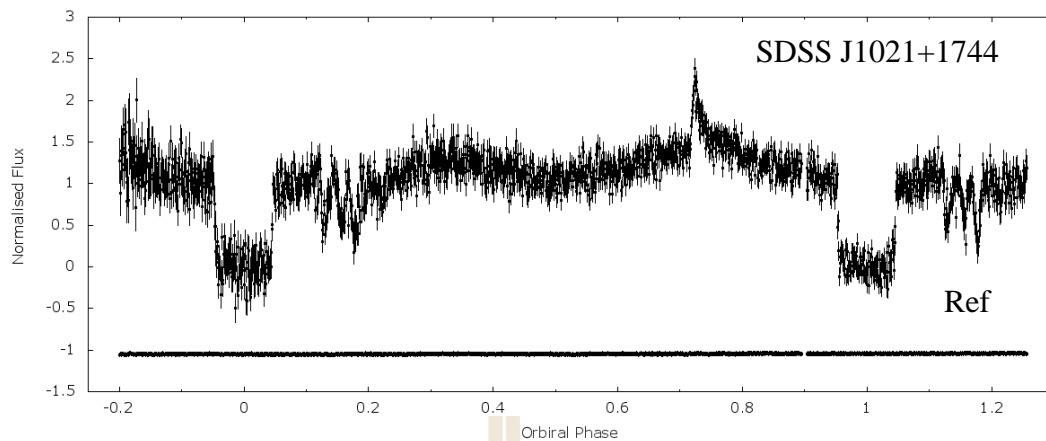


Figure 5.11 Full orbit light curves of SDSS J1021+1744 and reference star r' filter on 31 Mar 2014 in i' filter. At phase 0.7, a large flare is shown and also the dips position are around phase 0.1-1.2 and 1.1-1.2.

5.3 Future plan

For future works, we plan to study cause of the dips. At this work, we cannot model the variation of dips. This model can be improved, if we acquisition of more photometric data and more spectroscopic observation will allow us to obtain the masses of the system, radial velocity, characteristic of each component and spectrum, the effective temperature of the stars. If there are phenomenon on surface of the binary system or mass ejection, it will help us to understand the cause of unusual dips better. This system was observed on 26 January 2017 using g' and KG5 filters, we can see the dips as shown in Figure 5.12. Therefore, there is a possibility that we will find the dips in a near future.

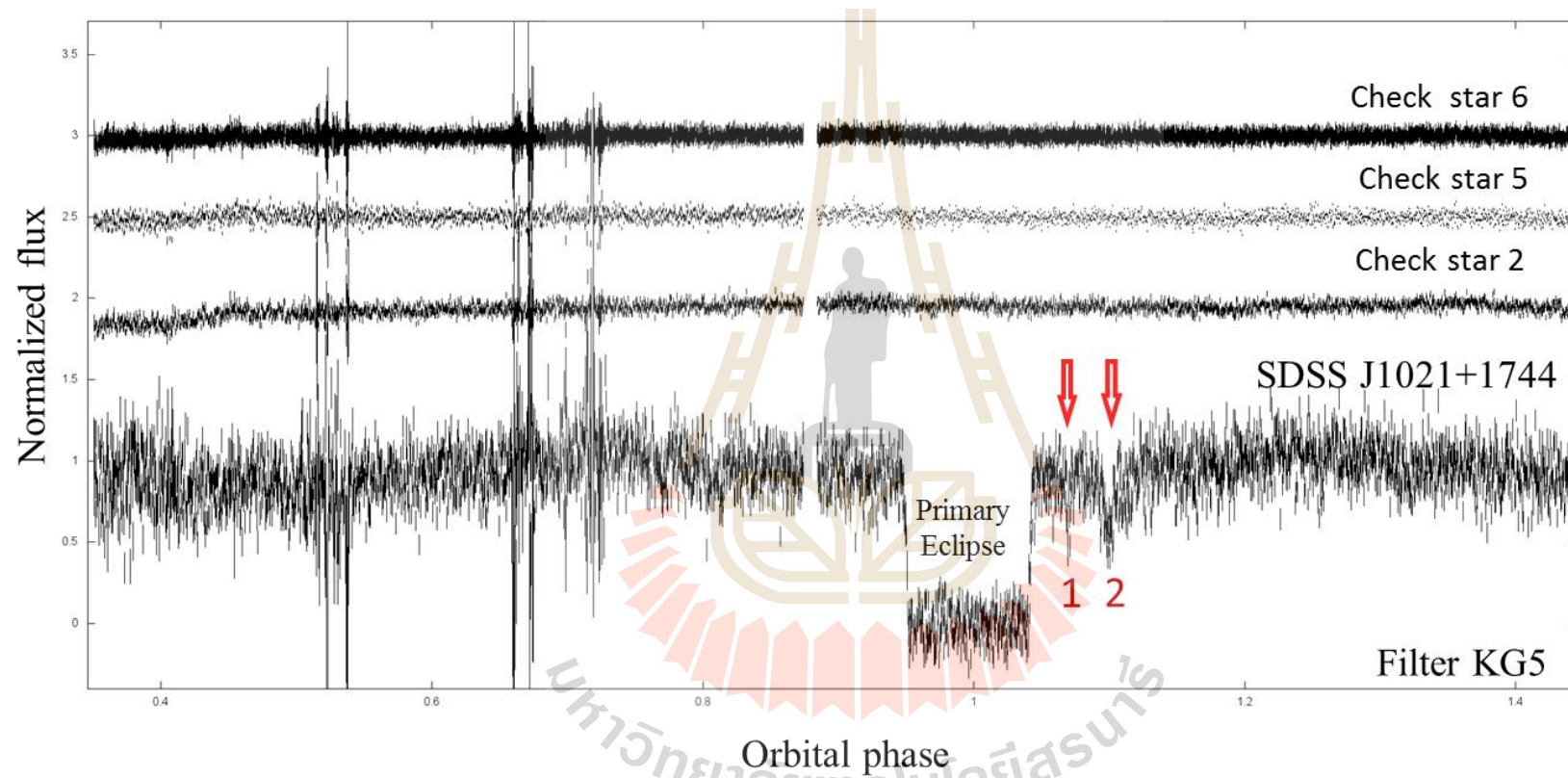
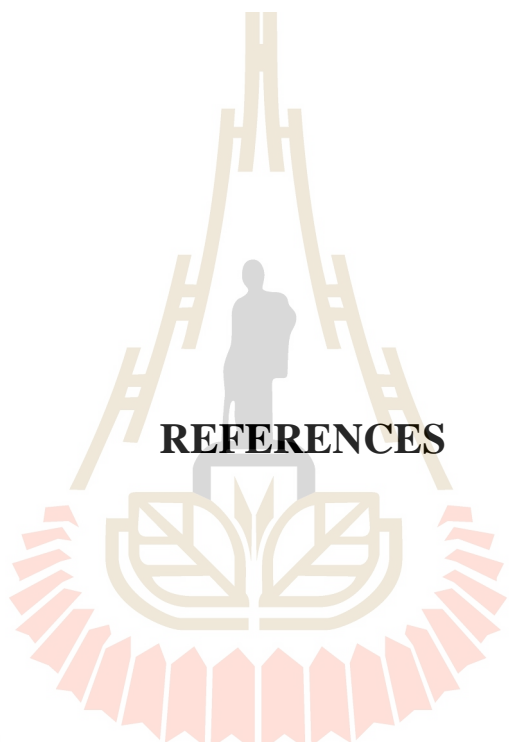


Figure 5.12 The light curve of SDSS J1021+1744 and check stars on 26 Jan 2017 in KG5 filter. We confirmed the dips come back. The large scatters are thin cloud and gap before the primary eclipse is the limit of the telescope.



REFERENCES

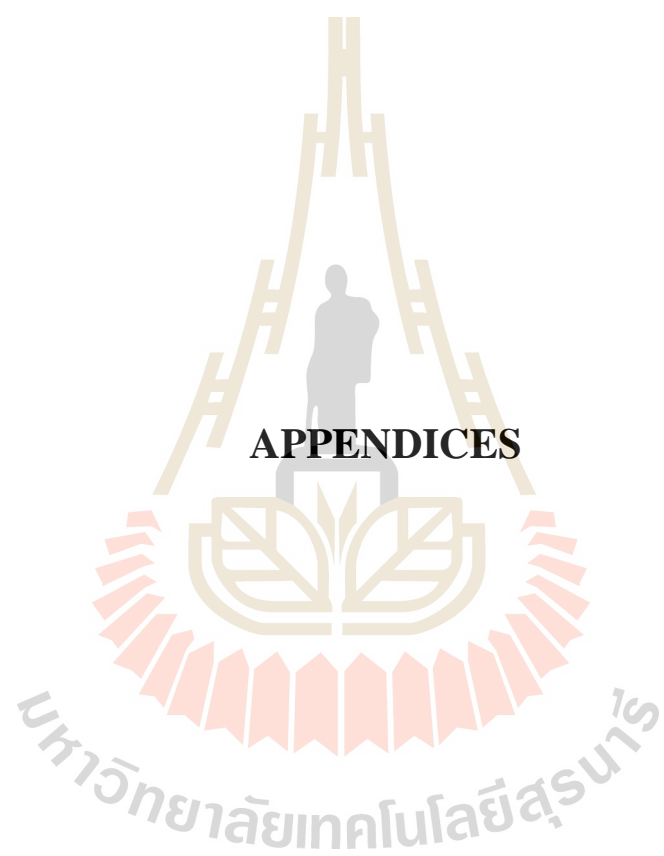
มหาวิทยาลัยเทคโนโลยีสุรนารี

REFERENCES

- Aungwerojwit, A. (2007). The properties of a spectroscopically selected sample of cataclysmic variables. **Ph.D. Thesis**. The university of Warwick.
- Bours, M.C.P. (2015). Detailed studies of white dwarf binaries and their orbital periods. **Ph.D. Thesis**. The University of Warwick.
- Bradstreet, D.H. (2005). Fundamentals of Solving Eclipsing Binary Light Curves Using Binary Maker 3. **SAS** 23-37.
- Bruton, D. (2011). Roche Lobes and the Morphologies of Close Binary Stars. Stephen F. Austin State University.
- Carroll, B.W. and Ostlie, D.A. (2007). An Introduction to Modern Astrophysics. **Pearson**. 2.
- Ceawford, D. (2014). gnuplot 4.6 An Interactive Plotting Program.
- Dhillon, V.S., Marsh, T.R., Atkinson, D.C., Bezawada, N., Bours, M.C.P., Copperwheat, C.M., Gamble, T., Hardy, L.K., Hickman, R.D., Irawati, P., Ives, D.J., Kerry, P., Leckngam, A., Littlefair, McLay, S.A., O'Brien, K, Peacocke, P.T., Poshyachinda, S., Richichi, A., Soonthornthum, B. and Vick, A. (2014). ULTRASPEC: a high-speed imaging photometer on the 2.4-m Thai National Telescope. **MNRAS** 444: 3504-3516.
- Eastman, J., Siverd, R. and Gaudi, B.S. (2010). Achieving Better Than 1 Minute Accuracy in the Heliocentric and Barycentric Julian Dates. **PASP**, 122: 935.

- Irawati, P., Richichi, A., Bours, M.C.P., Marsh, T.R., Sanguansak, N., Chanthorn, K., Hermes, J.J., Hardy, L.K., Parsons, S.G., Dhillon, V.S. and Littlefair, S.P. (2016). A large, long-lived structure near the trojan L5 point in the post common-envelope binary SDSS J1021+1744. **MNRAS** 456: 2446
- Izzard, R.G., Hall, P.D., Tauris, T.M. and Tout, C.A. (2011). An Eye to the Future Proceedings IAU Symposium. Common envelope evolution, 283.
- Meeus, J. (1998). *Astronomical Algorithms*. 2nd Edition.
- Jensen, K.A., Swank, J.H., Petre, R., Guinan, E.F., Sion, E.M. and Shipman, H.L. (1986). EXOSAT observations of V471 Tauri - A 9.25 minute white dwarf pulsation and orbital phase dependent X-ray dips. 309, 27.
- Mitra-Kraev, U. (2007). Flares on active M-type stars observed with XMM-Newton and Chandra. **A&A** 73: 144.
- Neil, J. (1998). The Lagrange Point. WMAP Education and Outreach.
- O'Donoghue, D., Koen, C., Kilkenny, D., Stobie, R.S., Koester, D., Bessell, M.S., Hambly, N. and MacGillivray, H., (2003). The DA+dMe eclipsing binary EC13471-1258: its cup runneth over ... just. **MNRAS** 345: 506.
- Parsons, S.G., Gaensicke, B.T., Boris, T., Marsh, T.R., Drake, A.J., Dhillon, V.S., Littlefair, S.P., Pyrzas, S., Rebassa-Mansergas, A. and Schreiber, M.R. (2013). Eclipsing Post Common Envelope Binaries from the Catalina Surveys. **MNRAS** 429: 256.
- Parsons, S.G., Marsh, T.R., Gaensicke, B.T. and Tepper, C. (2011). A stellar prominence in the white dwarf/red dwarf binary QS Vir: evidence for a detached system. **MNRAS** 412: 2563.

- Parsons, S.G., Hill, C.A., Marsh, T.R., Gaensicke, B.T., Watson, C.A., Steeghs, D., Dhillon, V.S., Littlefair, S.P., Copperwheat, C.M., Schreiber, M.R. and Zorotovic, M. (2016). The crowded magnetosphere of the post-common-envelope binary QS Virginis. **MNRAS** 458: 2793.
- Parsons, S.G., Gänsicke, B.T., Marsh, T.R., Ashley, R.P., Bours, M.C.P., Breedt, E., Burleigh, M.R., Copperwheat, C.M., Dhillon, V.S., Green, M., Hardy, L.K., Hermes, J.J., Irawati, P., Kerry, P., Littlefair, S.P., McAllister, M.J., Rattanasoon, S., Rebassa-Mansergas, A., Sahman, D.I. and Schreiber, M.R. (2017). Testing the white dwarf mass-radius relationship with eclipsing binaries. **MNRAS** 470: 4473-4492.
- Prsa, A. (2011). PHOEBE Scientific Reference.
- Rebassa-Mansergas, A. (2008). Post-Common-Envelope Binaries from the SloanDigital Sky Survey. **Ph.D. Thesis**. The University of Warwick.
- Rebassa-Mansergas, A., Nebot Gómez-Morán, A., Schreiber, M.R., Gänsicke, B.T., Schwöpe, A., Gallardo, J. and Koester, D., (2012). **MNRAS** 419: 806.
- Southworth J. (2014). JKTEBOP for analysing light curves of detached eclipsing binaries and transiting planets. Retrieved Feb 29, 2016, from <http://www.astro.keele.ac.uk/jkt/codes/jktebop.html>.
- Zorotovic, M., and Schreiber, M.R. (2013). **A&A** 549: A95.



APPENDICES

APPENDIX A

THE MORPHOLOGIES AND ROCHE LOBE

OF CLOSE BINARY STAR

Table A.1 The model of \tilde{r}_1 for radii of white dwarf in term of semi-major axis scale.

| ϕ | θ | \tilde{r}_1 | x | z |
|--------|----------|---------------|-------------|----------|
| 0 | 0 | 0.011353 | 0 | 0.011353 |
| 0 | 5 | 0.011353 | 0.000989479 | 0.011310 |
| 0 | 10 | 0.011353 | 0.001971428 | 0.011181 |
| 0 | 15 | 0.011353 | 0.002938373 | 0.010966 |
| 0 | 20 | 0.011353 | 0.003882956 | 0.010668 |
| 0 | 25 | 0.011353 | 0.004797987 | 0.010289 |
| 0 | 30 | 0.011353 | 0.005676504 | 0.009832 |
| 0 | 35 | 0.011353 | 0.006511819 | 0.009300 |
| 0 | 40 | 0.011353 | 0.007297575 | 0.008697 |
| 0 | 45 | 0.011353 | 0.008027793 | 0.008028 |
| 0 | 50 | 0.011353 | 0.008696915 | 0.007298 |
| 0 | 55 | 0.011353 | 0.009299849 | 0.006512 |
| 0 | 60 | 0.011353 | 0.009832005 | 0.005677 |
| 0 | 65 | 0.011353 | 0.010289333 | 0.004798 |
| 0 | 70 | 0.011353 | 0.010668354 | 0.003883 |

Table A.1 The model of \tilde{r}_1 for radii of white dwarf in term of semi-major axis scale (Continued).

| ϕ | θ | \tilde{r}_1 | x | z |
|--------|----------|---------------|-------------|-----------|
| 0 | 75 | 0.011353 | 0.010966181 | 0.002938 |
| 0 | 80 | 0.011353 | 0.01118055 | 0.001971 |
| 0 | 85 | 0.011353 | 0.011309826 | 0.000989 |
| 0 | 90 | 0.011353 | 0.011353028 | 6.95E-19 |
| 0 | 95 | 0.011353 | 0.011309826 | -0.000989 |
| 0 | 100 | 0.011353 | 0.01118055 | -0.001971 |
| 0 | 105 | 0.011353 | 0.010966181 | -0.002938 |
| 0 | 110 | 0.011353 | 0.010668354 | -0.003883 |
| 0 | 115 | 0.011353 | 0.010289333 | -0.004798 |
| 0 | 120 | 0.011353 | 0.009832005 | -0.005677 |
| 0 | 125 | 0.011353 | 0.009299849 | -0.006512 |
| 0 | 130 | 0.011353 | 0.008696915 | -0.007298 |
| 0 | 135 | 0.011353 | 0.008027793 | -0.008028 |
| 0 | 140 | 0.011353 | 0.007297575 | -0.008697 |
| 0 | 145 | 0.011353 | 0.006511819 | -0.009300 |
| 0 | 150 | 0.011353 | 0.005676504 | -0.009832 |
| 0 | 160 | 0.011353 | 0.003882956 | -0.010668 |
| 0 | 165 | 0.011353 | 0.002938373 | -0.010966 |

Table A.1 The model of \tilde{r}_1 for radii of white dwarf in term of semi-major axis scale (Continued).

| ϕ | θ | \tilde{r}_1 | \mathbf{x} | \mathbf{z} |
|--------|----------|---------------|--------------|--------------|
| 0 | 170 | 0.011353 | 0.001971428 | -0.011181 |
| 0 | 175 | 0.011353 | 0.000989479 | -0.01131 |
| 0 | 180 | 0.011353 | 1.39091E-18 | -0.011353 |
| 180 | 0 | 0.011353 | 0 | 0.011353 |
| 180 | 5 | 0.011353 | -0.000989479 | 0.011310 |
| 180 | 10 | 0.011353 | -0.001971428 | 0.011181 |
| 180 | 15 | 0.011353 | -0.002938373 | 0.010966 |
| 180 | 20 | 0.011353 | -0.003882956 | 0.010668 |
| 180 | 25 | 0.011353 | -0.004797987 | 0.010289 |
| 180 | 30 | 0.011353 | -0.005676504 | 0.009832 |
| 180 | 35 | 0.011353 | -0.006511819 | 0.00930 |
| 180 | 40 | 0.011353 | -0.007297575 | 0.008697 |
| 180 | 45 | 0.011353 | -0.008027793 | 0.008028 |
| 180 | 50 | 0.011353 | -0.008696915 | 0.007298 |
| 180 | 55 | 0.011353 | -0.009299849 | 0.006512 |
| 180 | 60 | 0.011353 | -0.009832005 | 0.005677 |
| 180 | 65 | 0.011353 | -0.010289333 | 0.004798 |

Table A.1 The model of \tilde{r}_1 for radii of white dwarf in term of semi-major axis scale (Continued).

| ϕ | θ | \tilde{r}_1 | \mathbf{x} | \mathbf{z} |
|--------|----------|---------------|--------------|--------------|
| 180 | 75 | 0.011353 | -0.010966181 | 0.002938 |
| 180 | 80 | 0.011353 | -0.011180549 | 0.001971 |
| 180 | 85 | 0.011353 | -0.011309826 | 0.000989 |
| 180 | 90 | 0.011353 | -0.011353028 | 6.95E-19 |
| 180 | 95 | 0.011353 | -0.011309826 | -0.000989 |
| 180 | 100 | 0.011353 | -0.011180549 | -0.001971 |
| 180 | 105 | 0.011353 | -0.010966181 | -0.002938 |
| 180 | 110 | 0.011353 | -0.010668354 | -0.003883 |
| 180 | 115 | 0.011353 | -0.010289333 | -0.004798 |
| 180 | 120 | 0.011353 | -0.009832005 | -0.005677 |
| 180 | 125 | 0.011353 | -0.009299849 | -0.006512 |
| 180 | 130 | 0.011353 | -0.008696915 | -0.007298 |
| 180 | 135 | 0.011353 | -0.008027793 | -0.008028 |
| 180 | 140 | 0.011353 | -0.007297575 | -0.008697 |
| 180 | 145 | 0.011353 | -0.006511819 | -0.009300 |
| 180 | 150 | 0.011353 | -0.005676504 | -0.009832 |
| 180 | 155 | 0.011353 | -0.004797987 | -0.010289 |

Table A.1 The model of \tilde{r}_1 for radii of white dwarf in term of semi-major axis scale (Continued).

| ϕ | θ | \tilde{r}_1 | \mathbf{x} | \mathbf{z} |
|--------|----------|---------------|--------------|--------------|
| 180 | 160 | 0.011353 | -0.003882956 | -0.010668 |
| 180 | 165 | 0.011353 | -0.002938373 | -0.010966 |
| 180 | 170 | 0.011353 | -0.001971428 | -0.011181 |
| 180 | 175 | 0.011353 | -0.000989479 | -0.011310 |
| 180 | 180 | 0.011353 | -1.39091E-18 | -0.011353 |



Table A.2 The model of \tilde{r}_2 for radii of main-sequence in term of semi-major axis scale.

| ϕ | θ | \tilde{r}_2 | x | z |
|--------|----------|---------------|-------------|----------|
| 0 | 0 | 0.309411 | 1 | 0.309411 |
| 0 | 5 | 0.309112 | 0.973059137 | 0.307935 |
| 0 | 10 | 0.309286 | 0.946293008 | 0.304587 |
| 0 | 15 | 0.30996 | 0.919776472 | 0.299398 |
| 0 | 20 | 0.311162 | 0.89357641 | 0.292396 |
| 0 | 25 | 0.312926 | 0.867751948 | 0.283607 |
| 0 | 30 | 0.315291 | 0.842354478 | 0.27305 |
| 0 | 35 | 0.318305 | 0.817427566 | 0.26074 |
| 0 | 40 | 0.322024 | 0.793006843 | 0.246685 |
| 0 | 45 | 0.326513 | 0.769120095 | 0.230880 |
| 0 | 50 | 0.33185 | 0.745788015 | 0.213309 |
| 0 | 55 | 0.338122 | 0.723026625 | 0.193939 |
| 0 | 60 | 0.345424 | 0.700853732 | 0.172712 |
| 0 | 65 | 0.353847 | 0.679305324 | 0.149542 |
| 0 | 70 | 0.363441 | 0.658477623 | 0.124304 |
| 0 | 75 | 0.374108 | 0.638639814 | 0.096826 |
| 0 | 80 | 0.385302 | 0.62055129 | 0.066907 |
| 0 | 85 | 0.395195 | 0.606309036 | 0.034443 |

Table A.2 The model of \tilde{r}_2 for radii of main-sequence in term of semi-major axis scale (Continued).

| ϕ | θ | \tilde{r}_2 | x | z |
|--------|----------|---------------|-------------|----------|
| 0 | 90 | 0.399569 | 0.600430739 | 2.45E-17 |
| 0 | 95 | 0.395195 | 0.606309036 | -0.03444 |
| 0 | 100 | 0.385302 | 0.62055129 | -0.06691 |
| 0 | 105 | 0.374108 | 0.638639814 | -0.09683 |
| 0 | 110 | 0.363441 | 0.658477623 | -0.12430 |
| 0 | 115 | 0.353847 | 0.679305324 | -0.14954 |
| 0 | 120 | 0.345424 | 0.700853732 | -0.17271 |
| 0 | 125 | 0.338122 | 0.723026625 | -0.19394 |
| 0 | 130 | 0.33185 | 0.745788015 | -0.21331 |
| 0 | 135 | 0.326513 | 0.769120095 | -0.23088 |
| 0 | 140 | 0.322024 | 0.793006843 | -0.24668 |
| 0 | 145 | 0.318305 | 0.817427566 | -0.26074 |
| 0 | 150 | 0.315291 | 0.842354478 | -0.27305 |
| 0 | 155 | 0.312926 | 0.867751948 | -0.28361 |
| 0 | 160 | 0.311162 | 0.89357641 | -0.2924 |
| 0 | 165 | 0.30996 | 0.919776472 | -0.2994 |
| 0 | 170 | 0.309286 | 0.946293008 | -0.30459 |

Table A.2 The model of \tilde{r}_2 for radii of main-sequence in term of semi-major axis scale (Continued).

| ϕ | θ | \tilde{r}_2 | x | z |
|--------|----------|---------------|-------------|----------|
| 0 | 175 | 0.309112 | 0.973059137 | -0.30794 |
| 0 | 180 | 0.309411 | 1 | -0.30941 |
| 180 | 0 | 0.309411 | 1 | 0.309411 |
| 180 | 5 | 0.310161 | 1.027032318 | 0.308981 |
| 180 | 10 | 0.311134 | 1.054063672 | 0.30661 |
| 180 | 15 | 0.312927 | 1.080991479 | 0.302264 |
| 180 | 20 | 0.314898 | 1.107701625 | 0.295908 |
| 180 | 25 | 0.317229 | 1.134066739 | 0.287507 |
| 180 | 30 | 0.319888 | 1.15994407 | 0.277031 |
| 180 | 35 | 0.322839 | 1.185173019 | 0.264454 |
| 180 | 40 | 0.326037 | 1.209572402 | 0.249759 |
| 180 | 45 | 0.329424 | 1.232937655 | 0.232938 |
| 180 | 50 | 0.332929 | 1.255038405 | 0.214003 |
| 180 | 55 | 0.336466 | 1.275617078 | 0.192989 |
| 180 | 60 | 0.339932 | 1.294389613 | 0.169966 |
| 180 | 65 | 0.343205 | 1.311049725 | 0.145045 |
| 180 | 70 | 0.346154 | 1.325278367 | 0.118392 |

Table A.2 The model of \tilde{r}_2 for radii of main-sequence in term of semi-major axis scale (Continued).

| ϕ | θ | \tilde{r}_2 | x | z |
|--------|----------|---------------|-------------|----------|
| 180 | 70 | 0.346154 | 1.325278367 | 0.118392 |
| 180 | 75 | 0.348639 | 1.336759742 | 0.090235 |
| 180 | 80 | 0.350529 | 1.345204047 | 0.060869 |
| 180 | 85 | 0.351713 | 1.350374908 | 0.030654 |
| 180 | 90 | 0.352117 | 1.352116672 | 2.16E-17 |
| 180 | 95 | 0.351713 | 1.350374908 | -0.03065 |
| 180 | 100 | 0.350529 | 1.345204047 | -0.06087 |
| 180 | 105 | 0.348639 | 1.336759742 | -0.09023 |
| 180 | 110 | 0.346154 | 1.325278367 | -0.11839 |
| 180 | 115 | 0.343205 | 1.311049725 | -0.14504 |
| 180 | 120 | 0.339932 | 1.294389613 | -0.16997 |
| 180 | 125 | 0.336466 | 1.275617078 | -0.19299 |
| 180 | 130 | 0.332929 | 1.255038405 | -0.21400 |
| 180 | 135 | 0.329424 | 1.232937655 | -0.23294 |
| 180 | 140 | 0.326037 | 1.209572402 | -0.24976 |
| 180 | 145 | 0.322839 | 1.185173019 | -0.26445 |
| 180 | 150 | 0.319888 | 1.15994407 | -0.27703 |

Table A.2 The model of \tilde{r}_2 for radii of main-sequence in term of semi-major axis scale (Continued).

| ϕ | θ | \tilde{r}_2 | x | z |
|--------|----------|---------------|-------------|----------|
| 180 | 155 | 0.317229 | 1.134066739 | -0.28751 |
| 180 | 160 | 0.314898 | 1.107701625 | -0.29591 |
| 180 | 165 | 0.312927 | 1.080991479 | -0.30226 |
| 180 | 170 | 0.311134 | 1.054063672 | -0.30661 |
| 180 | 175 | 0.310161 | 1.027032318 | -0.30898 |
| 180 | 180 | 0.309411 | 1 | -0.30941 |

Table A.3 The result of Roche lobe inner potential from model of \tilde{r}_{1_inner} for white dwarf in term of semi-major axis scale.

| ϕ | θ | \tilde{r}_{1_inner} | \mathbf{x} | \mathbf{z} |
|--------|----------|------------------------|--------------|--------------|
| 0 | 0 | 0.39885 | 0 | 0.39885 |
| 0 | 5 | 0.398482 | 0.034730038 | 0.396966 |
| 0 | 10 | 0.39868 | 0.069230036 | 0.392623 |
| 0 | 15 | 0.39947 | 0.103390442 | 0.385858 |
| 0 | 20 | 0.400885 | 0.137110893 | 0.376709 |
| 0 | 25 | 0.402966 | 0.1703006 | 0.365211 |
| 0 | 30 | 0.405759 | 0.202879324 | 0.351397 |
| 0 | 35 | 0.409325 | 0.234779047 | 0.335299 |
| 0 | 40 | 0.413739 | 0.265946491 | 0.316943 |
| 0 | 45 | 0.419098 | 0.296346707 | 0.296347 |
| 0 | 50 | 0.425521 | 0.32596811 | 0.27352 |
| 0 | 55 | 0.433167 | 0.354829525 | 0.248454 |
| 0 | 60 | 0.442239 | 0.382990228 | 0.221120 |
| 0 | 65 | 0.453008 | 0.41056462 | 0.191449 |
| 0 | 70 | 0.465838 | 0.437744583 | 0.159326 |
| 0 | 75 | 0.481233 | 0.464835226 | 0.124552 |
| 0 | 80 | 0.499910 | 0.492315365 | 0.086808 |

Table A.3 The result of Roche lobe inner potential from model of \tilde{r}_{1_inner} for white dwarf in term of semi-major axis scale (Continued).

| ϕ | θ | \tilde{r}_{1_inner} | \mathbf{x} | \mathbf{z} |
|--------|----------|------------------------|--------------|--------------|
| 0 | 85 | 0.522932 | 0.520941671 | 0.045576 |
| 0 | 90 | 0.548902 | 0.548902146 | 3.36E-17 |
| 0 | 95 | 0.522932 | 0.520941671 | -0.045576 |
| 0 | 100 | 0.49991 | 0.492315365 | -0.086808 |
| 0 | 105 | 0.481233 | 0.464835226 | -0.124552 |
| 0 | 110 | 0.465838 | 0.437744583 | -0.159326 |
| 0 | 115 | 0.453008 | 0.41056462 | -0.191449 |
| 0 | 120 | 0.442239 | 0.382990228 | -0.221120 |
| 0 | 125 | 0.433167 | 0.354829525 | -0.248454 |
| 0 | 130 | 0.425521 | 0.32596811 | -0.273520 |
| 0 | 135 | 0.419098 | 0.296346707 | -0.296347 |
| 0 | 140 | 0.413739 | 0.265946491 | -0.316943 |
| 0 | 145 | 0.409325 | 0.234779047 | -0.335299 |
| 0 | 150 | 0.405759 | 0.202879324 | -0.351397 |
| 0 | 155 | 0.402966 | 0.170300600 | -0.365211 |
| 0 | 160 | 0.400885 | 0.137110893 | -0.376709 |
| 0 | 165 | 0.399470 | 0.103390442 | -0.385858 |

Table A.3 The result of Roche lobe inner potential from model of \tilde{r}_{1_inner} for white dwarf in term of semi-major axis scale (Continued).

| ϕ | θ | \tilde{r}_{1_inner} | \mathbf{x} | \mathbf{z} |
|--------|----------|------------------------|--------------|--------------|
| 0 | 170 | 0.39868 | 0.069230036 | -0.392623 |
| 0 | 175 | 0.398482 | 0.034730038 | -0.396966 |
| 0 | 180 | 0.39885 | 4.8865E-17 | -0.398850 |
| 180 | 0 | 0.39885 | 0 | 0.398850 |
| 180 | 5 | 0.399758 | -0.034841178 | 0.398236 |
| 180 | 10 | 0.401182 | -0.069664579 | 0.395087 |
| 180 | 15 | 0.403101 | -0.104330101 | 0.389365 |
| 180 | 20 | 0.405487 | -0.138684775 | 0.381033 |
| 180 | 25 | 0.408313 | -0.172560574 | 0.370057 |
| 180 | 30 | 0.411543 | -0.205771705 | 0.356407 |
| 180 | 35 | 0.415135 | -0.23811144 | 0.340058 |
| 180 | 40 | 0.419032 | -0.269348602 | 0.320997 |
| 180 | 45 | 0.423167 | -0.29922399 | 0.299224 |
| 180 | 50 | 0.427452 | -0.327447241 | 0.274761 |
| 180 | 55 | 0.431782 | -0.353695006 | 0.24766 |
| 180 | 60 | 0.436028 | -0.37761175 | 0.218014 |
| 180 | 65 | 0.440044 | -0.398814968 | 0.18597 |

Table A.3 The result of Roche lobe inner potential from model of \tilde{r}_{1_inner} for white dwarf in term of semi-major axis scale (Continued).

| ϕ | θ | \tilde{r}_{1_inner} | \mathbf{x} | \mathbf{z} |
|--------|----------|------------------------|--------------|--------------|
| 180 | 70 | 0.443663 | -0.416906854 | 0.151742 |
| 180 | 75 | 0.446716 | -0.431494119 | 0.115619 |
| 180 | 80 | 0.449038 | -0.442216155 | 0.077975 |
| 180 | 85 | 0.450493 | -0.448779005 | 0.039263 |
| 180 | 90 | 0.450989 | -0.450989174 | 2.76E-17 |
| 180 | 95 | 0.450493 | -0.448779005 | -0.039263 |
| 180 | 100 | 0.449038 | -0.442216155 | -0.077975 |
| 180 | 105 | 0.446716 | -0.431494119 | -0.115619 |
| 180 | 110 | 0.443663 | -0.416906854 | -0.151742 |
| 180 | 115 | 0.440044 | -0.398814968 | -0.18597 |
| 180 | 120 | 0.436028 | -0.377611750 | -0.218014 |
| 180 | 125 | 0.431782 | -0.353695006 | -0.24766 |
| 180 | 130 | 0.427452 | -0.327447241 | -0.274761 |
| 180 | 135 | 0.423167 | -0.29922399 | -0.299224 |
| 180 | 140 | 0.419032 | -0.269348602 | -0.320997 |
| 180 | 145 | 0.415135 | -0.238111440 | -0.340058 |
| 180 | 150 | 0.411543 | -0.205771705 | -0.356407 |

Table A.3 The result of Roche lobe inner potential from model of \tilde{r}_{1_inner} for white dwarf in term of semi-major axis scale (Continued).

| ϕ | θ | \tilde{r}_{1_inner} | \mathbf{x} | \mathbf{z} |
|--------|----------|------------------------|--------------|--------------|
| 180 | 155 | 0.408313 | -0.172560574 | -0.370057 |
| 180 | 160 | 0.405487 | -0.138684775 | -0.381033 |
| 180 | 165 | 0.403101 | -0.104330101 | -0.389365 |
| 180 | 170 | 0.401182 | -0.069664579 | -0.395087 |
| 180 | 175 | 0.399758 | -0.034841178 | -0.398236 |
| 180 | 180 | 0.398850 | -4.8865E-17 | -0.398850 |



Table A.4 The result of Roche lobe inner potential from model of \tilde{r}_{2_inner} for main-sequence in term of semi-major axis scale.

| ϕ | θ | \tilde{r}_{2_inner} | \mathbf{x} | \mathbf{z} |
|--------|----------|------------------------|--------------|--------------|
| 0 | 0 | 0.315 | 1 | 0.315 |
| 0 | 5 | 0.31467 | 0.972574679 | 0.313473 |
| 0 | 10 | 0.314846 | 0.945327479 | 0.310063 |
| 0 | 15 | 0.315556 | 0.918328021 | 0.304804 |
| 0 | 20 | 0.316832 | 0.891637052 | 0.297725 |
| 0 | 25 | 0.318713 | 0.865306267 | 0.288852 |
| 0 | 30 | 0.321245 | 0.839377718 | 0.278206 |
| 0 | 35 | 0.324485 | 0.813882788 | 0.265803 |
| 0 | 40 | 0.328506 | 0.788840598 | 0.25165 |
| 0 | 45 | 0.333393 | 0.764255689 | 0.235744 |
| 0 | 50 | 0.339256 | 0.74011464 | 0.21807 |
| 0 | 55 | 0.346235 | 0.716381059 | 0.198592 |
| 0 | 60 | 0.354507 | 0.692987824 | 0.177254 |
| 0 | 65 | 0.364309 | 0.669824179 | 0.153964 |
| 0 | 70 | 0.375962 | 0.646711526 | 0.128586 |
| 0 | 75 | 0.389939 | 0.623347772 | 0.100924 |
| 0 | 80 | 0.407063 | 0.599121362 | 0.070686 |

Table A.4 The result of Roche lobe inner potential from model of \tilde{r}_{2_inner} for white dwarf in term of semi-major axis scale (Continued).

| ϕ | θ | \tilde{r}_{2_inner} | \mathbf{x} | \mathbf{z} |
|--------|----------|------------------------|--------------|--------------|
| 0 | 85 | 0.429986 | 0.571649897 | 0.037476 |
| 0 | 90 | 0.454592 | 0.545407764 | 2.78E-17 |
| 0 | 95 | 0.429986 | 0.571649897 | -0.03748 |
| 0 | 100 | 0.407063 | 0.599121362 | -0.07069 |
| 0 | 105 | 0.389939 | 0.623347772 | -0.10092 |
| 0 | 110 | 0.375962 | 0.646711526 | -0.12859 |
| 0 | 115 | 0.364309 | 0.669824179 | -0.15396 |
| 0 | 120 | 0.354507 | 0.692987824 | -0.17725 |
| 0 | 125 | 0.346235 | 0.716381059 | -0.19859 |
| 0 | 130 | 0.339256 | 0.74011464 | -0.21807 |
| 0 | 135 | 0.333393 | 0.764255689 | -0.23574 |
| 0 | 140 | 0.328506 | 0.788840598 | -0.25165 |
| 0 | 145 | 0.324485 | 0.813882788 | -0.2658 |
| 0 | 150 | 0.321245 | 0.839377718 | -0.27821 |
| 0 | 155 | 0.318713 | 0.865306267 | -0.28885 |
| 0 | 160 | 0.316832 | 0.891637052 | -0.29772 |
| 0 | 165 | 0.315556 | 0.918328021 | -0.30480 |

Table A.4 The result of Roche lobe inner potential from model of \tilde{r}_{2_inner} for white dwarf in term of semi-major axis scale (Continued).

| ϕ | θ | \tilde{r}_{2_inner} | \mathbf{x} | \mathbf{z} |
|--------|----------|------------------------|--------------|--------------|
| 0 | 170 | 0.314846 | 0.945327479 | -0.31006 |
| 0 | 175 | 0.31467 | 0.972574679 | -0.31347 |
| 0 | 180 | 0.315 | 1 | -0.315 |
| 180 | 0 | 0.315 | 1 | 0.315 |
| 180 | 5 | 0.315811 | 1.027524777 | 0.31461 |
| 180 | 10 | 0.317082 | 1.055060743 | 0.312265 |
| 180 | 15 | 0.318791 | 1.082509092 | 0.307928 |
| 180 | 20 | 0.320914 | 1.109759128 | 0.301561 |
| 180 | 25 | 0.323428 | 1.13668645 | 0.293125 |
| 180 | 30 | 0.326301 | 1.16315067 | 0.282585 |
| 180 | 35 | 0.329499 | 1.188992632 | 0.269909 |
| 180 | 40 | 0.332973 | 1.21403121 | 0.255072 |
| 180 | 45 | 0.336667 | 1.238059849 | 0.23806 |
| 180 | 50 | 0.340507 | 1.260843241 | 0.218873 |
| 180 | 55 | 0.344399 | 1.282114832 | 0.197539 |
| 180 | 60 | 0.34823 | 1.301576367 | 0.174115 |
| 180 | 65 | 0.351869 | 1.318901162 | 0.148706 |

Table A.4 The result of Roche lobe inner potential from model of \tilde{r}_{2_inner} for white dwarf in term of semi-major axis scale (Continued).

| ϕ | θ | \tilde{r}_{2_inner} | \mathbf{x} | \mathbf{z} |
|--------|----------|------------------------|--------------|--------------|
| 180 | 70 | 0.355162 | 1.333743286 | 0.121473 |
| 180 | 75 | 0.357952 | 1.345754681 | 0.092645 |
| 180 | 80 | 0.360081 | 1.35461101 | 0.062527 |
| 180 | 85 | 0.36142 | 1.360044249 | 0.0315 |
| 180 | 90 | 0.361876 | 1.361876207 | 2.22E-17 |
| 180 | 95 | 0.36142 | 1.360044249 | -0.0315 |
| 180 | 100 | 0.360081 | 1.35461101 | -0.06253 |
| 180 | 105 | 0.357952 | 1.345754681 | -0.09264 |
| 180 | 110 | 0.355162 | 1.333743286 | -0.12147 |
| 180 | 115 | 0.351869 | 1.318901162 | -0.14871 |
| 180 | 120 | 0.34823 | 1.301576367 | -0.17412 |
| 180 | 125 | 0.344399 | 1.282114832 | -0.19754 |
| 180 | 130 | 0.340507 | 1.260843241 | -0.21887 |
| 180 | 135 | 0.336667 | 1.238059849 | -0.23806 |
| 180 | 140 | 0.332973 | 1.21403121 | -0.25507 |
| 180 | 145 | 0.329499 | 1.188992632 | -0.26991 |
| 180 | 150 | 0.326301 | 1.16315067 | -0.28259 |

Table A.4 The result of Roche lobe inner potential from model of \tilde{r}_{2_inner} for white dwarf in term of semi-major axis scale (Continued).

| ϕ | θ | \tilde{r}_{2_inner} | \mathbf{x} | \mathbf{z} |
|--------|----------|------------------------|--------------|--------------|
| 180 | 155 | 0.323428 | 1.13668645 | -0.29313 |
| 180 | 160 | 0.320914 | 1.109759128 | -0.30156 |
| 180 | 165 | 0.318791 | 1.082509092 | -0.30793 |
| 180 | 170 | 0.317082 | 1.055060743 | -0.31226 |
| 180 | 175 | 0.315811 | 1.027524777 | -0.31461 |
| 180 | 180 | 0.315 | 1 | -0.315 |

APPENDIX B

LIGHT CURVE OF SDSS J1021+1744

In this work, we obtain data with ULTRASPEC and ULTRACAM installed on TNT and WHT and show light curve of SDSS J102102.25+174439.9 in normalized flux scale and orbital phase, observation date, cycle number of eclipsing and filter in multi-band.

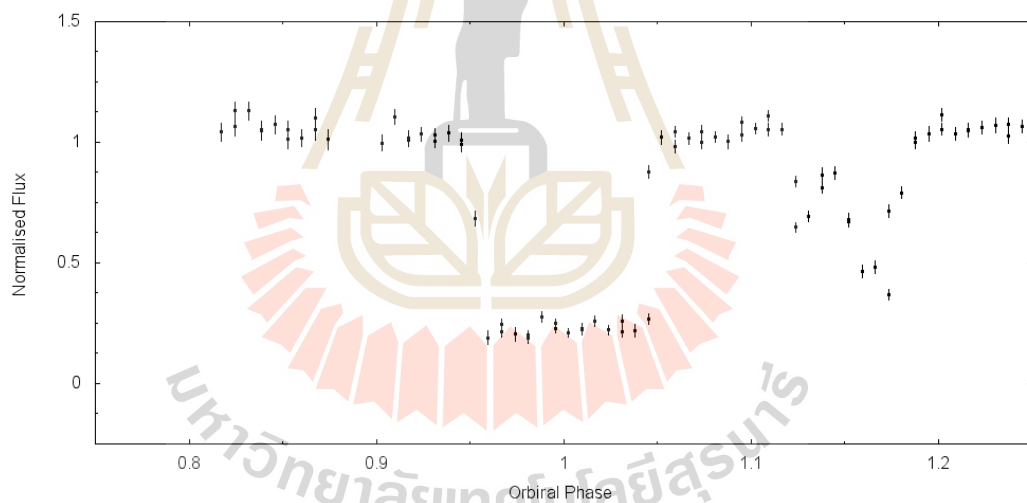


Figure B.1 First observation on 2014, 7 Jan, cycle zero with g' filter.

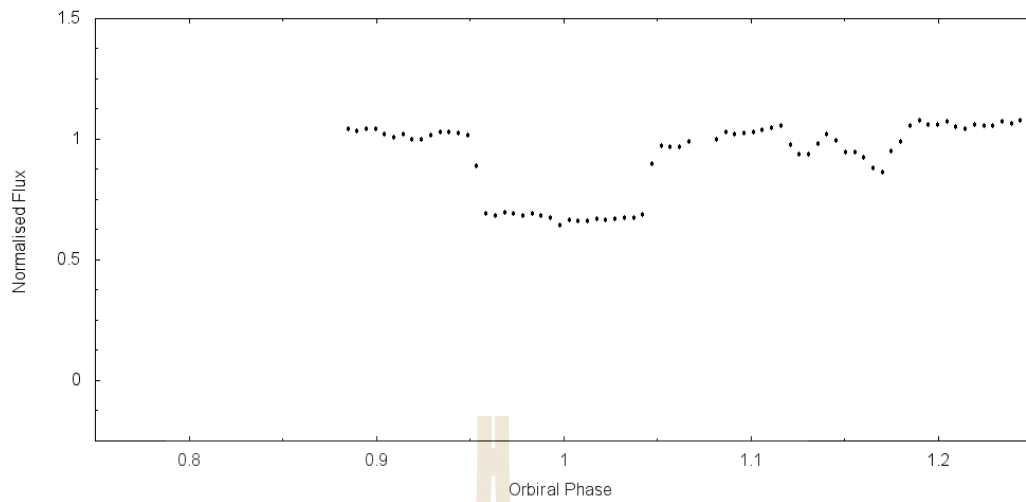


Figure B.2 Observation date on 2014, 8 Jan, cycle 6 with Clear filter.

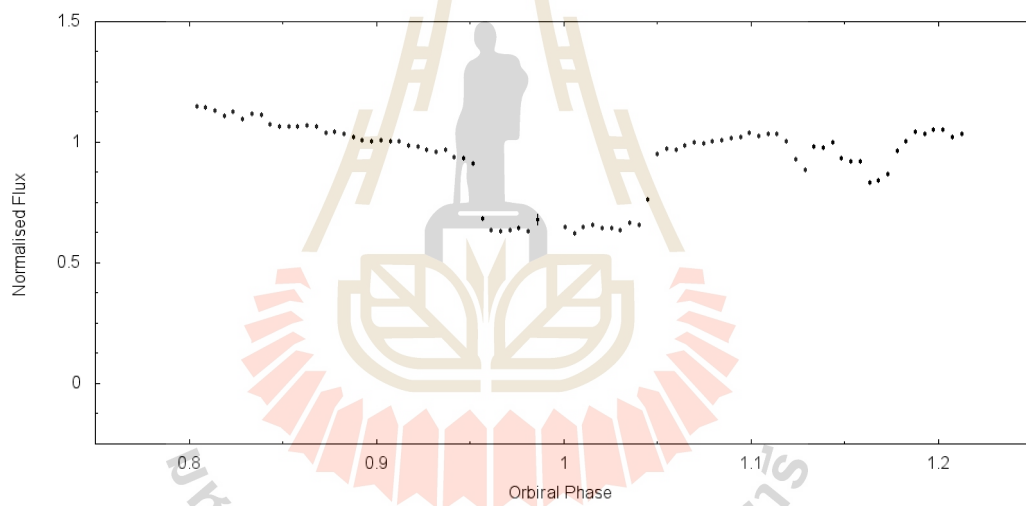


Figure B.3 Observation date on 2014, 8 Jan, cycle 7 with Clear filter.

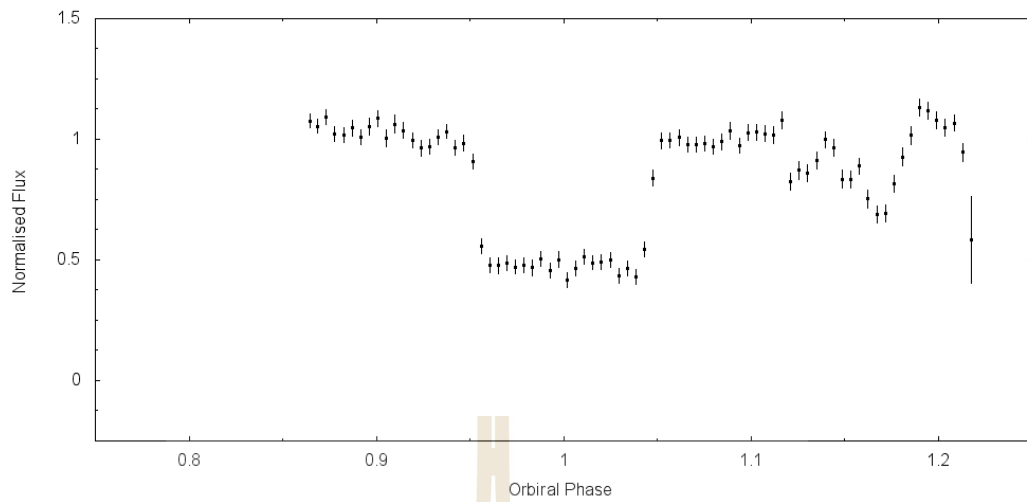


Figure B.4 Observation date on 2014, 10 Jan, cycle 20 with r' filter.

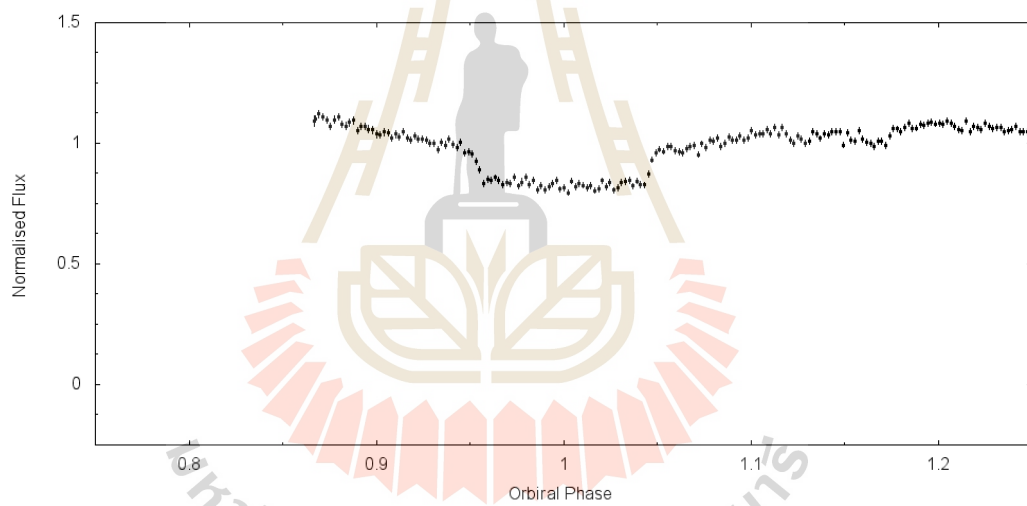


Figure B.5 Observation date on 2014, 11 Jan, cycle 28 with $i'+z'$ filter.

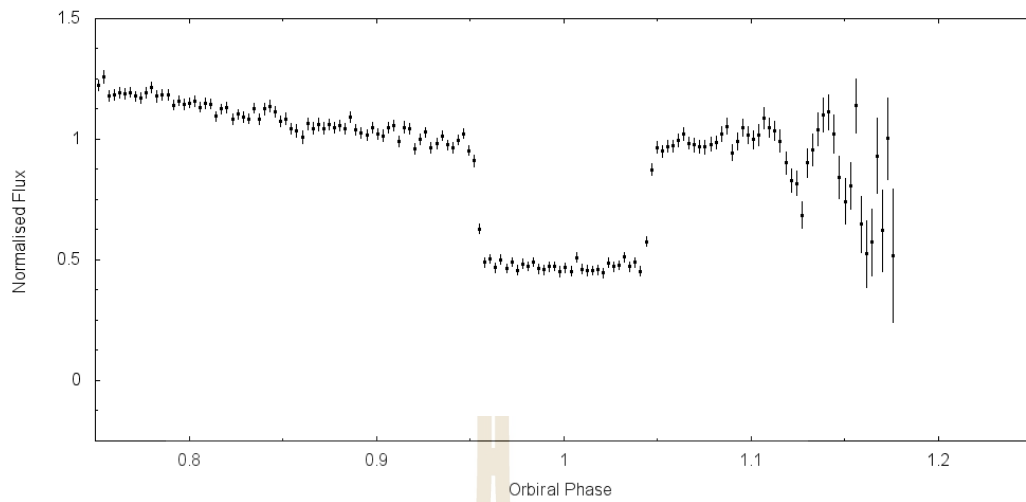


Figure B.6 Observation date on 2014, 11 Jan, cycle 29 with r' filter.

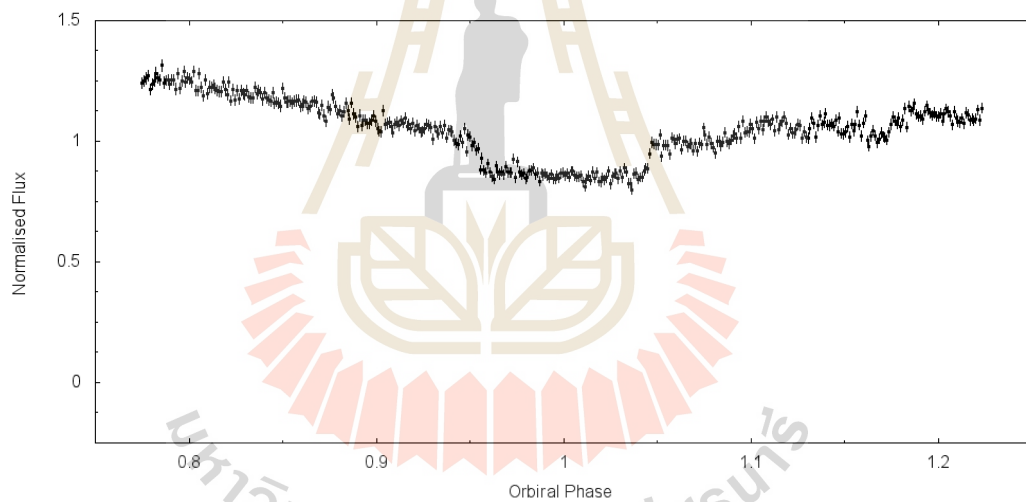


Figure B.7 Observation date on 2014, 12 Jan, cycle 35 with $i'+z'$ filter.

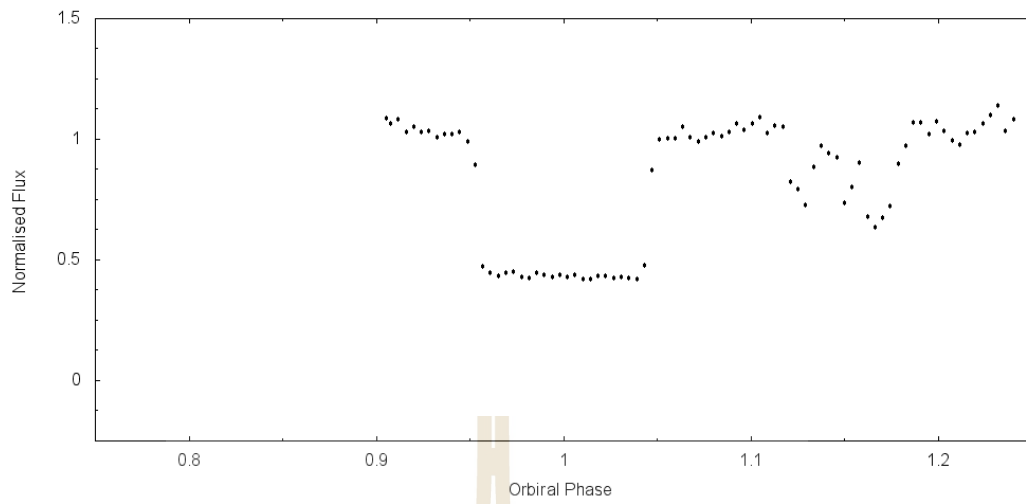


Figure B.8 Observation date on 2014, 12 Jan, cycle 36 with KG5 filter.

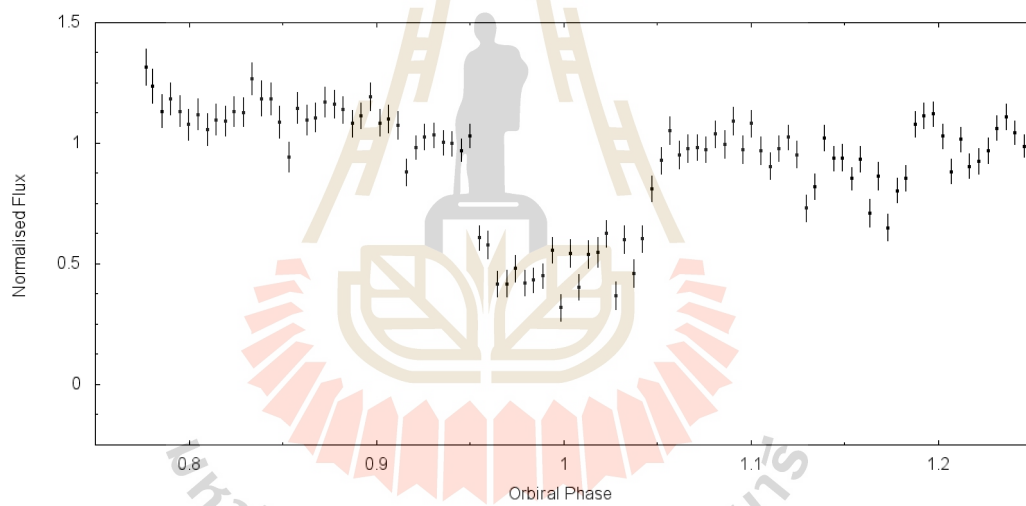


Figure B.9 Observation date on 2014, 15 Jan, cycle 57 with r' filter.

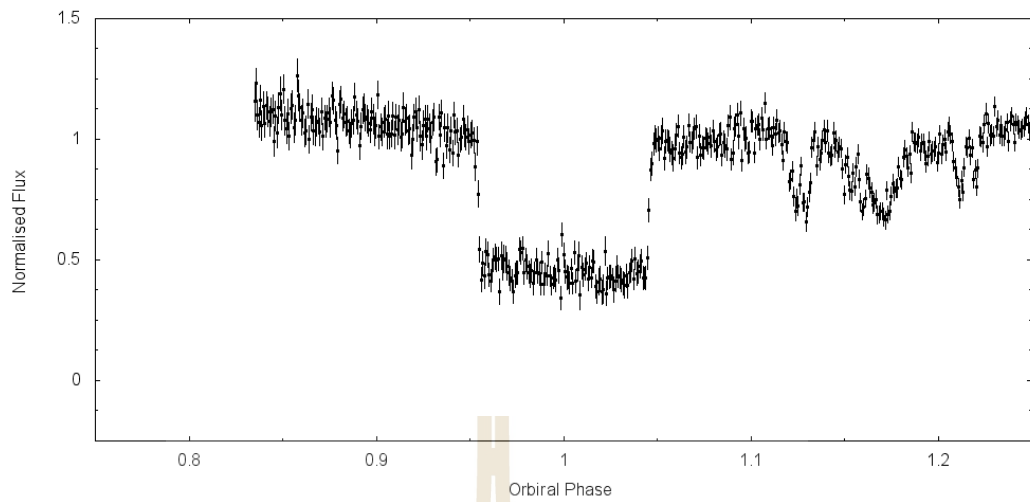


Figure B.10 Observation date on 2014, 28 Jan, cycle 148 with KG5 filter.

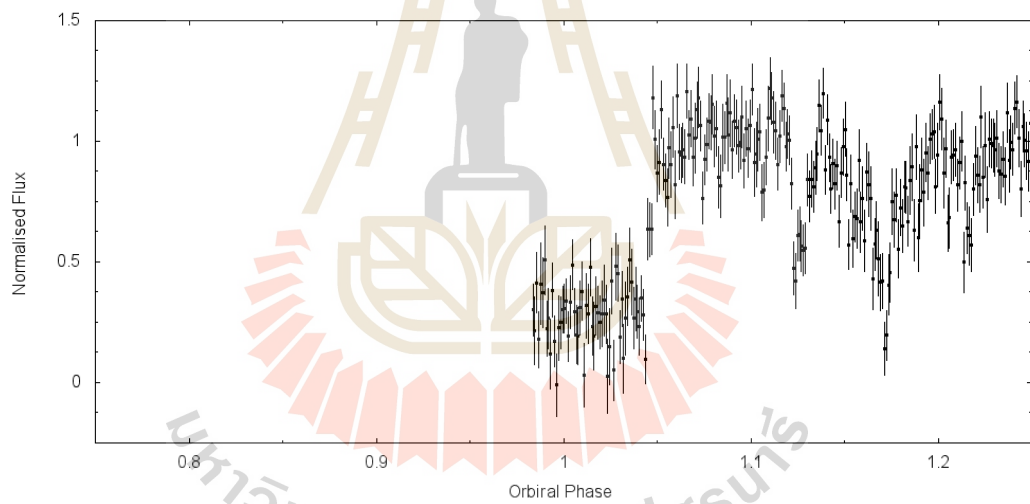


Figure B.11 Observation date on 2014, 11 Feb, with g' filter.

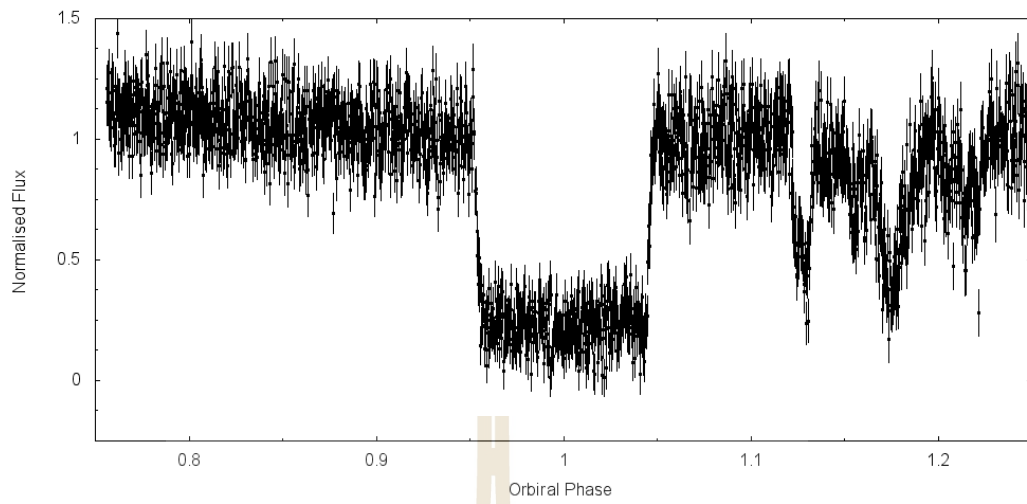


Figure B.12 Observation date on 2014, 28 Jan, cycle 370 with g' filter.

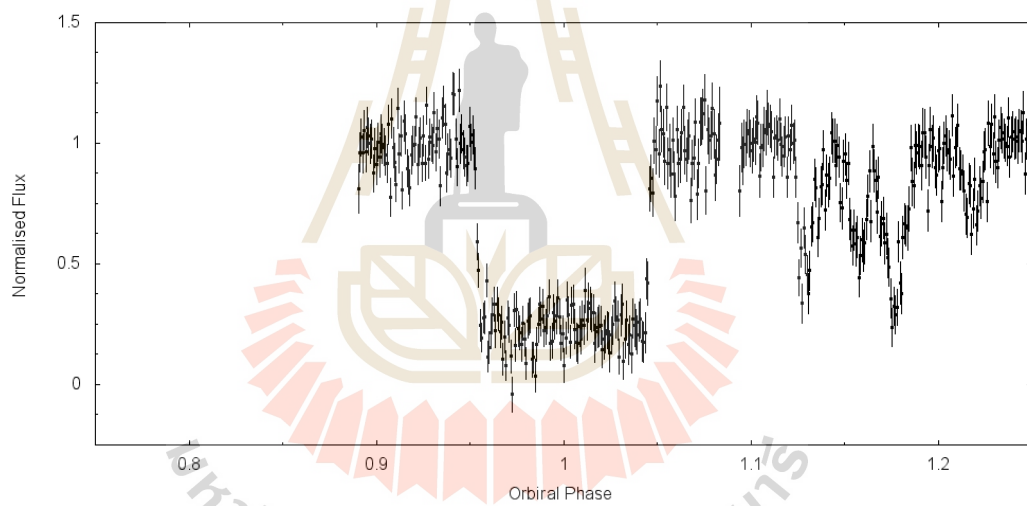


Figure B.13 Observation date on 2014, 26 Mar, cycle 554 with g' filter.

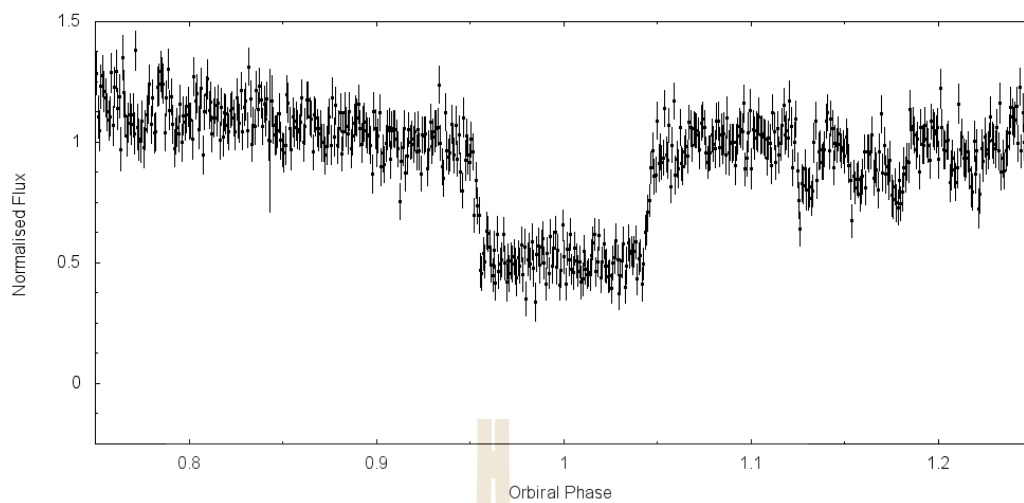


Figure B.14 Observation date on 2014, 29 Mar, cycle 575 with r' filter.

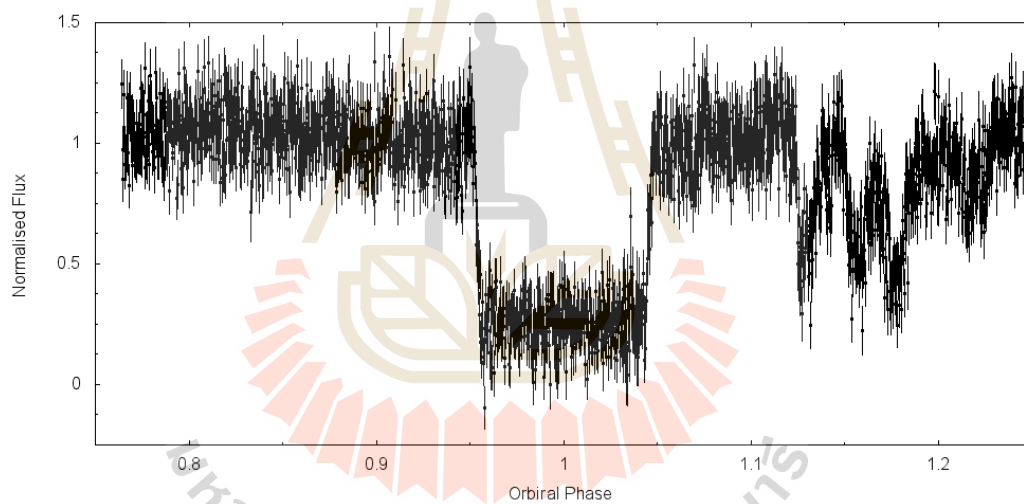


Figure B.15 Observation date on 2014, 30 Mar, cycle 582 with g' filter.

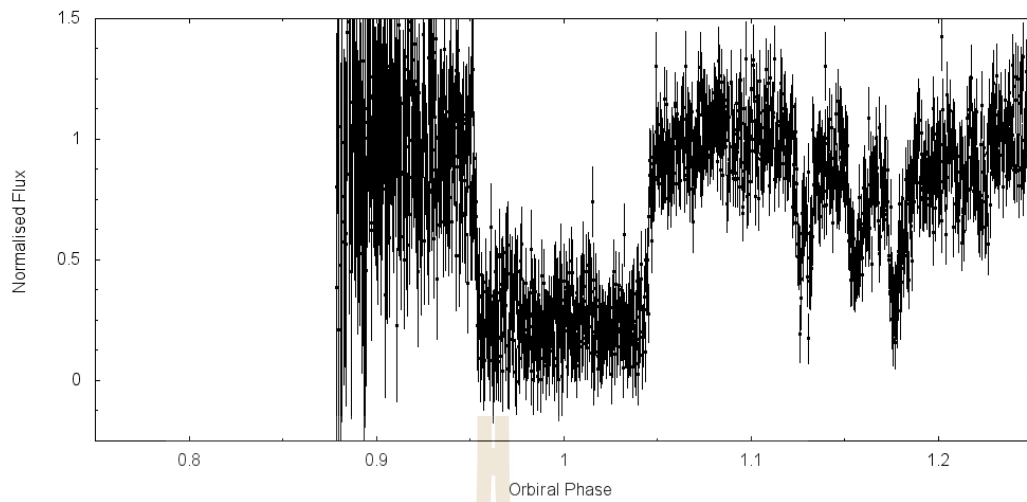


Figure B.16 Observation date on 2014, 1 Apr, cycle 596 with g' filter.

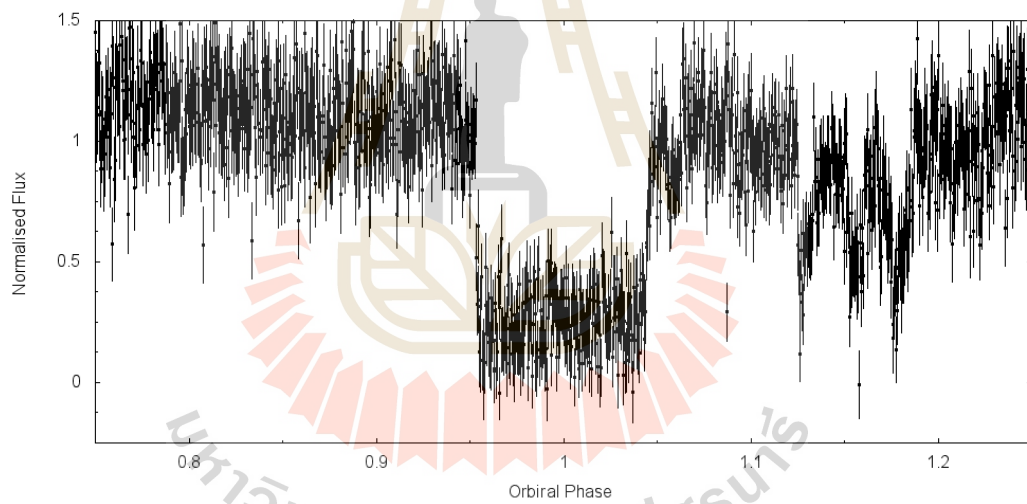


Figure B.17 Observation date on 2014, 2 Apr, cycle 604 with g' filter.

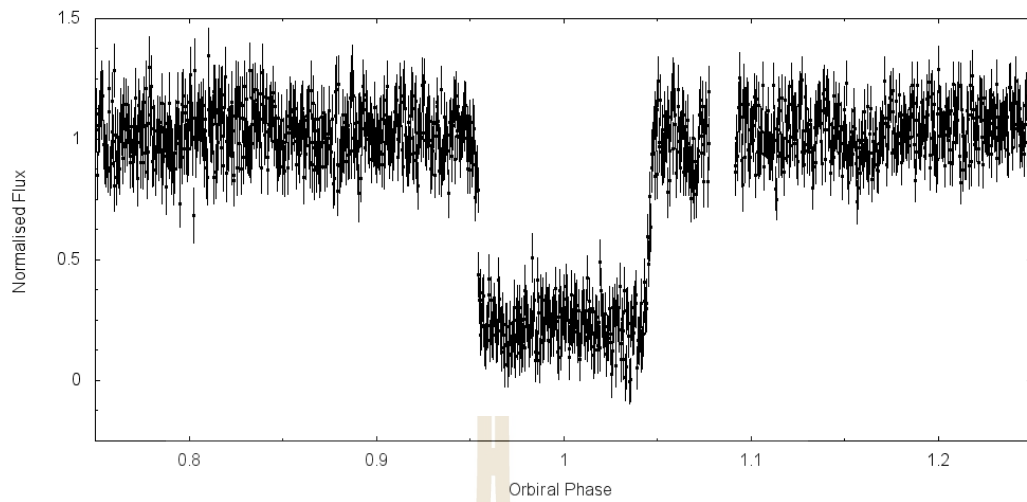


Figure B.18 Observation date on 2014, 22 Dec, cycle 2,486 with g' filter.

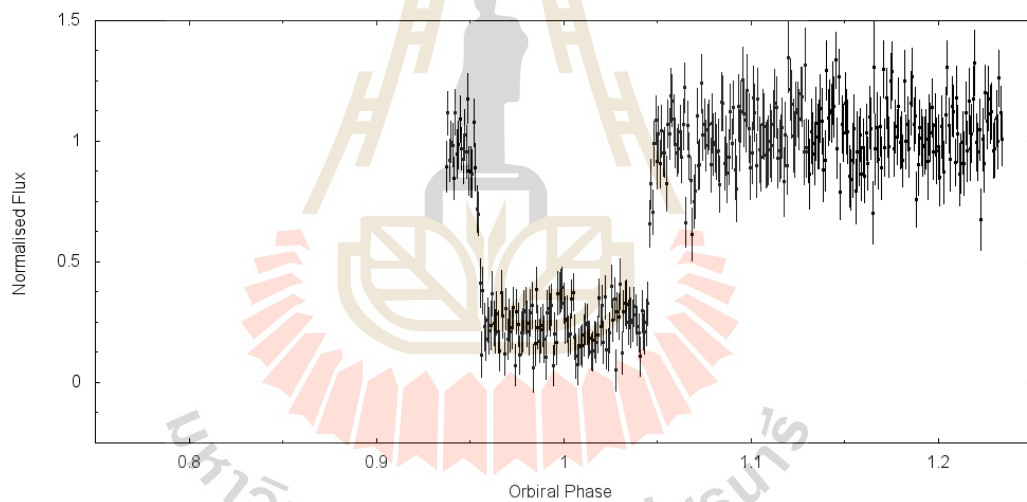


Figure B.19 Observation date on 2015, 12 Jan, cycle 2,635 with g' filter.

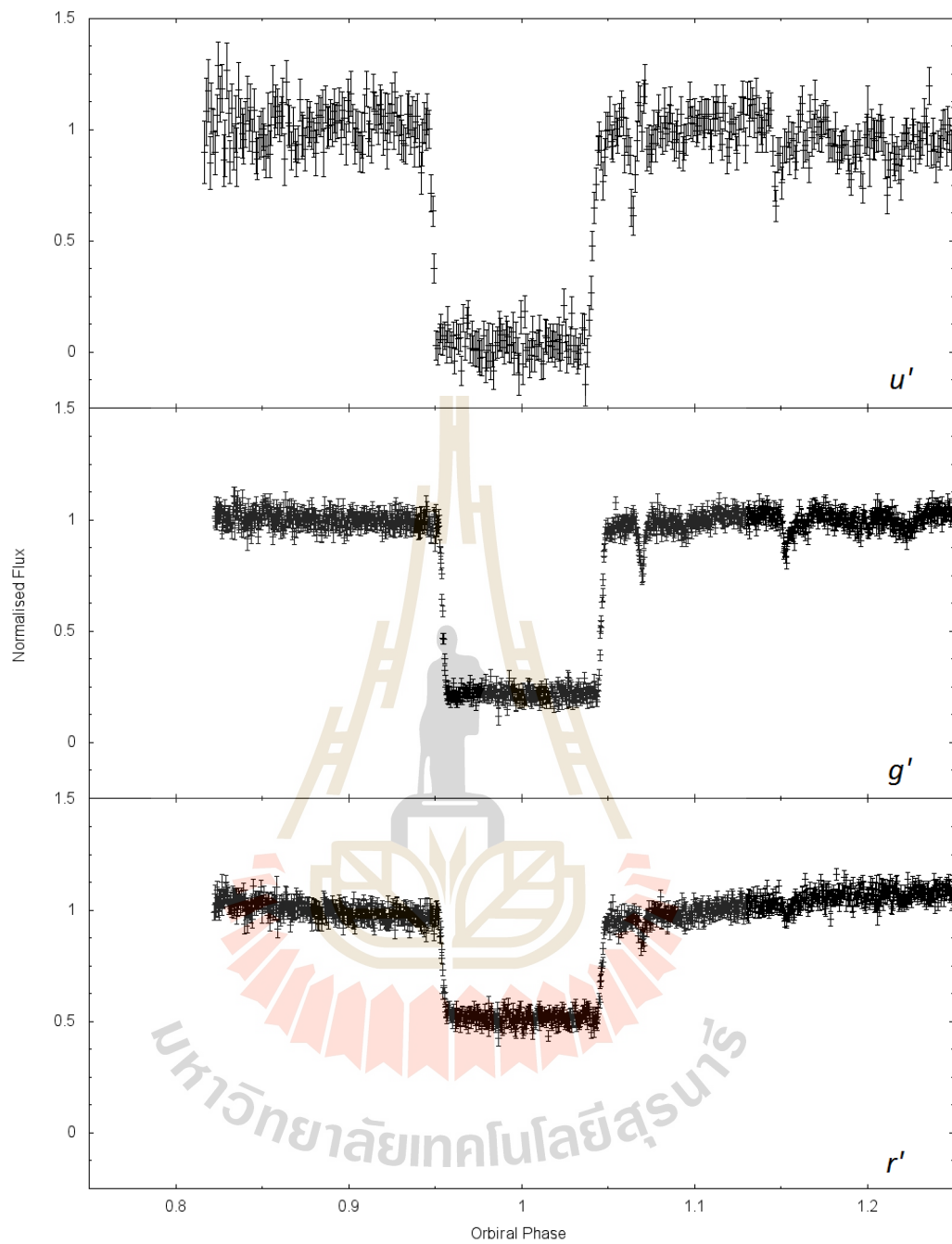


Figure B.20 Observation date on 2015, 17 Jan from WHF telescope with ULTRACAM, cycle 2,666 with r' , g' and u' filters.

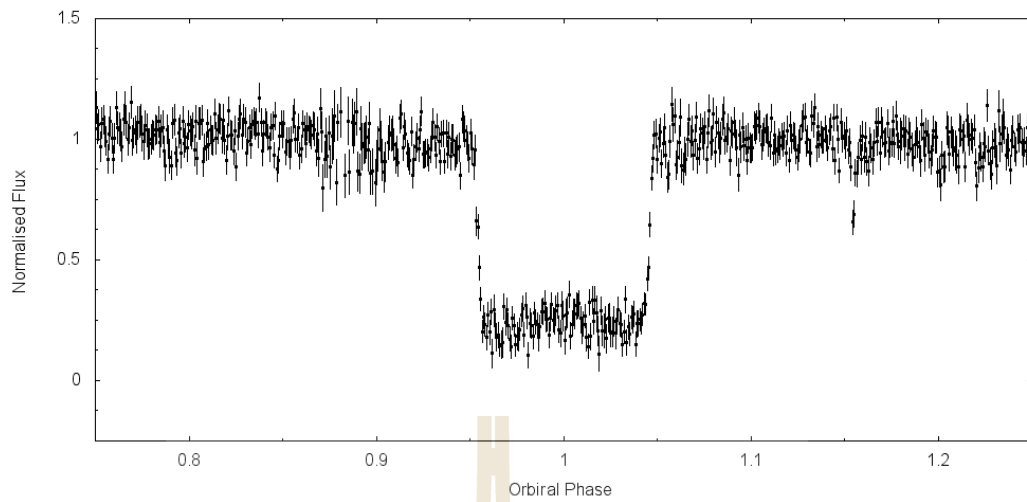


Figure B.21 Observation date on 2015, 19 Feb, cycle 2,906 with g' filter.

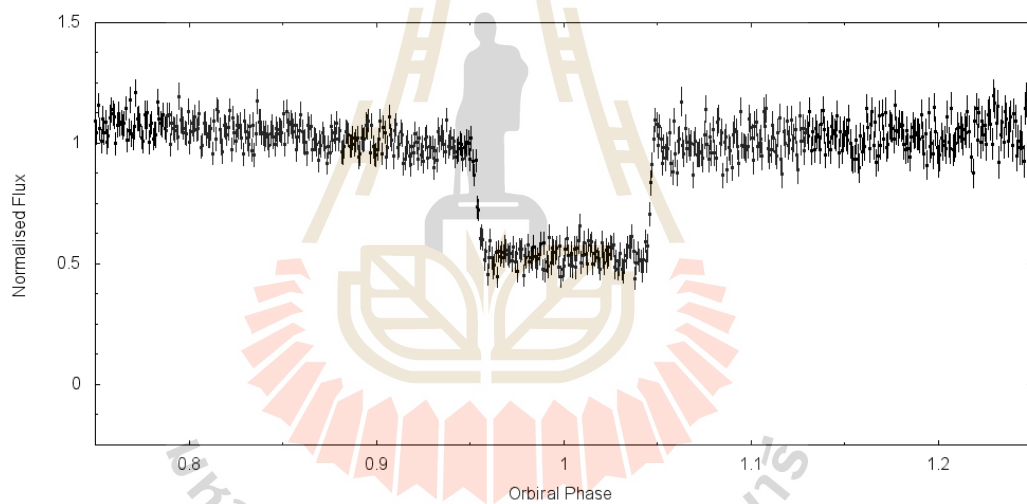


Figure B.22 Observation date on 2015, 19 Feb, cycle 2,907 with r' filter.

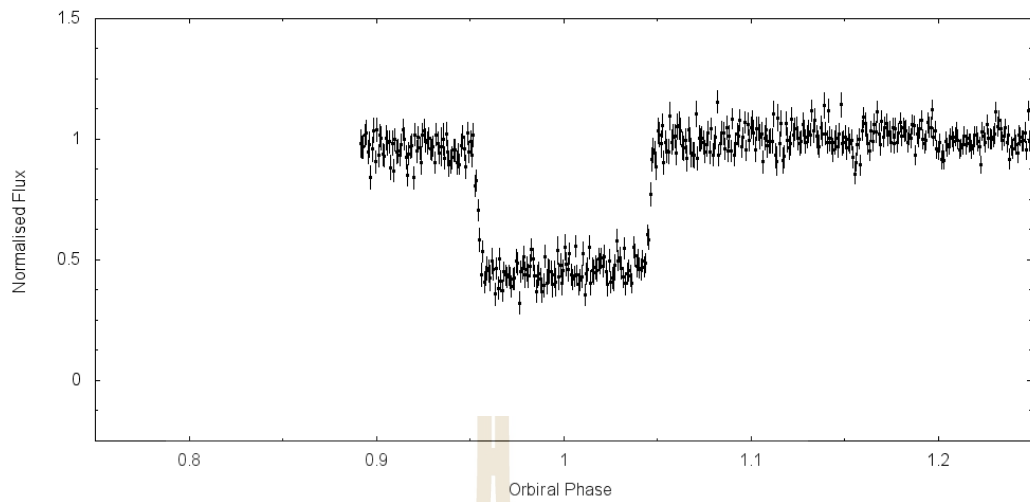


Figure B.23 Observation date on 2015, 24 Feb, cycle 2,941 with KG5 filter.

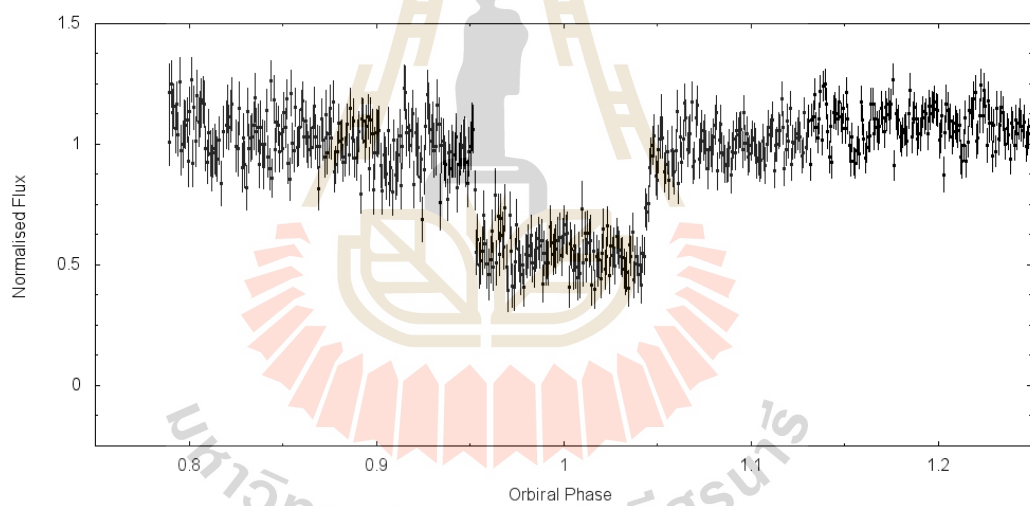


Figure B.24 Observation date on 2015, 18 Mar, cycle 3,097 with r' filter.

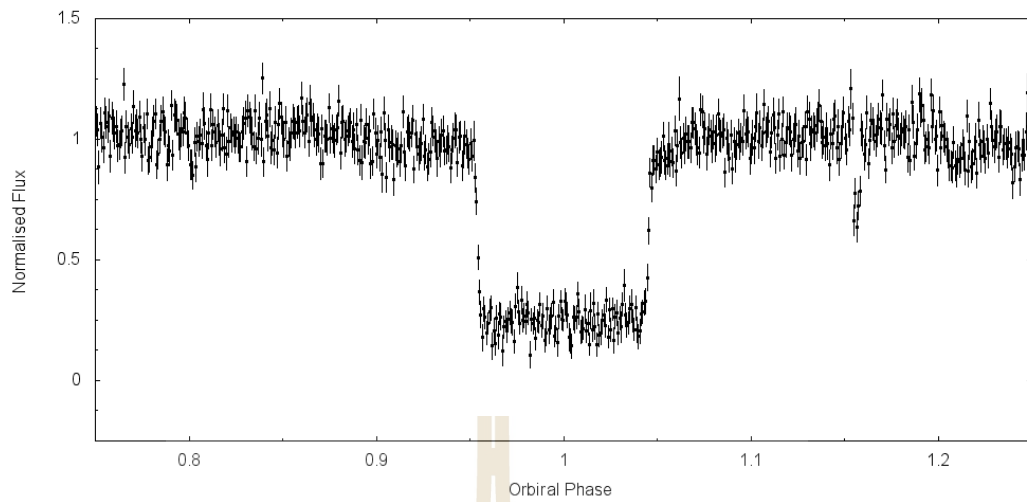


Figure B.25 Observation date on 2015, 18 Mar, cycle 3,098 with g' filter.

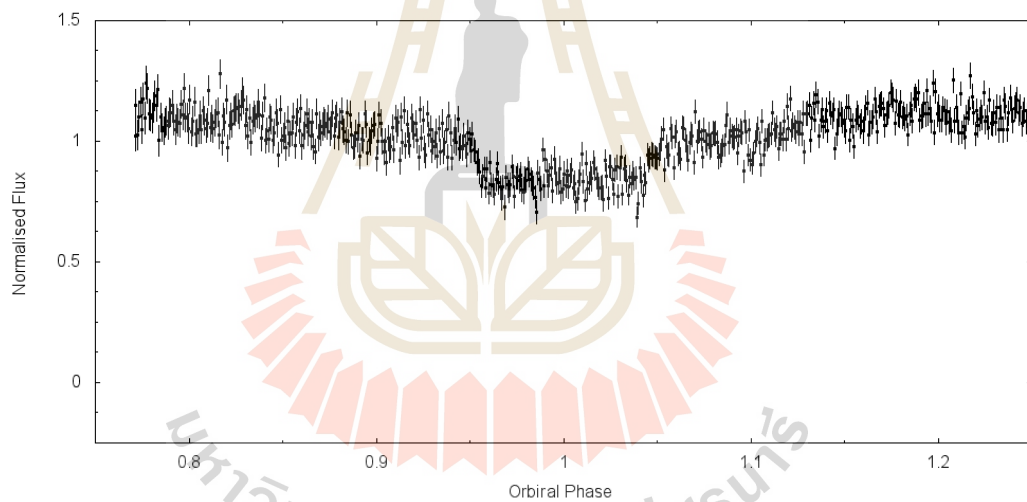


Figure B.26 Observation date on 2015, 19 Mar, cycle 3,104 with i' filter.

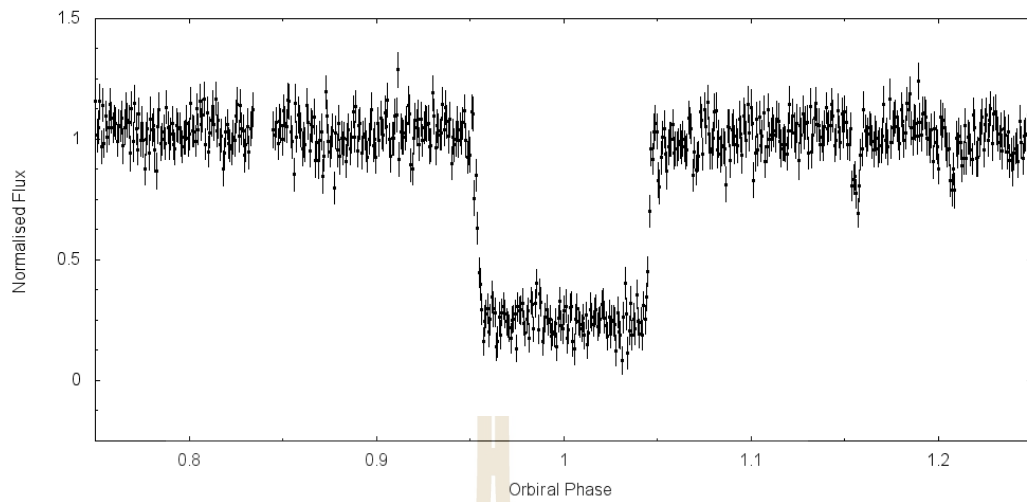


Figure B.27 Observation date on 2015, 19 Mar, cycle 3,105 with g' filter.

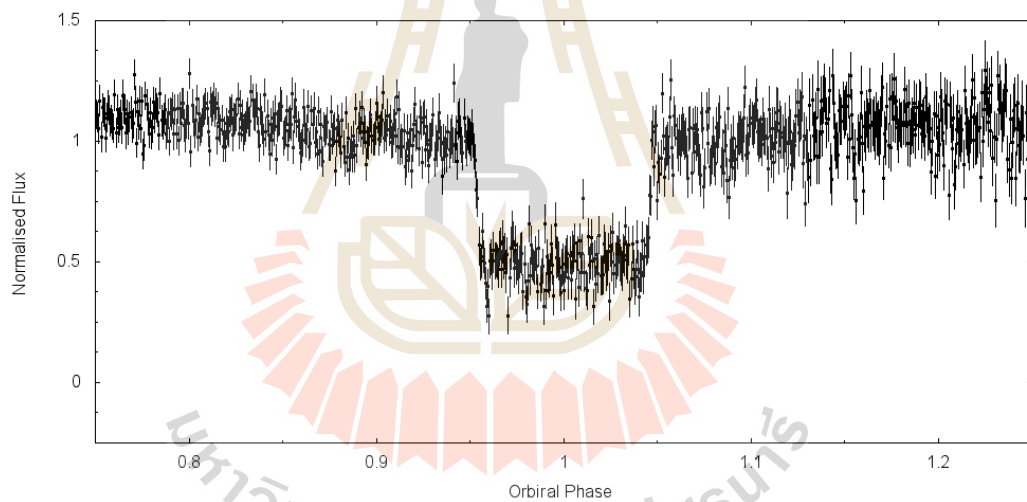


Figure B.28 Observation date on 2015, 19 Mar, cycle 3,106 with KG5 filter.

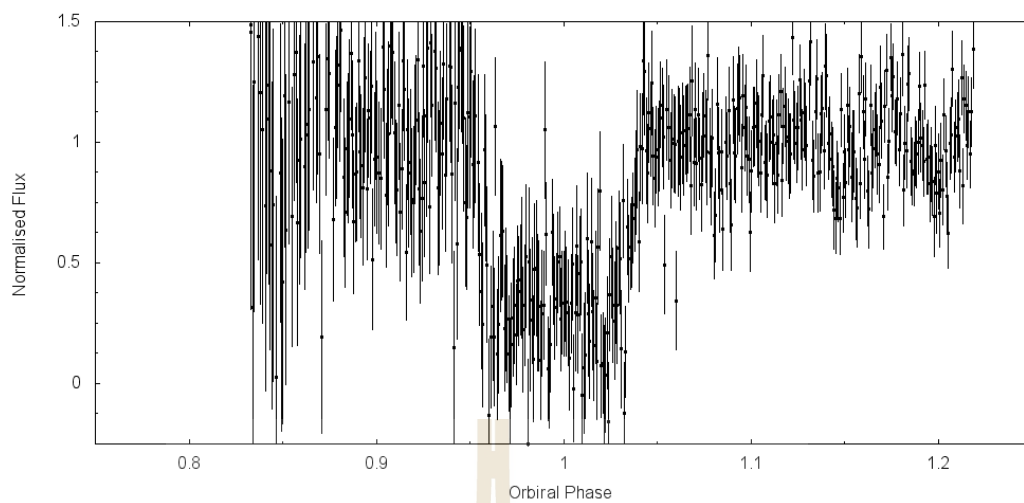


Figure B.29 Observation date on 2015, 20 Mar, cycle 3,111 with g' filter.

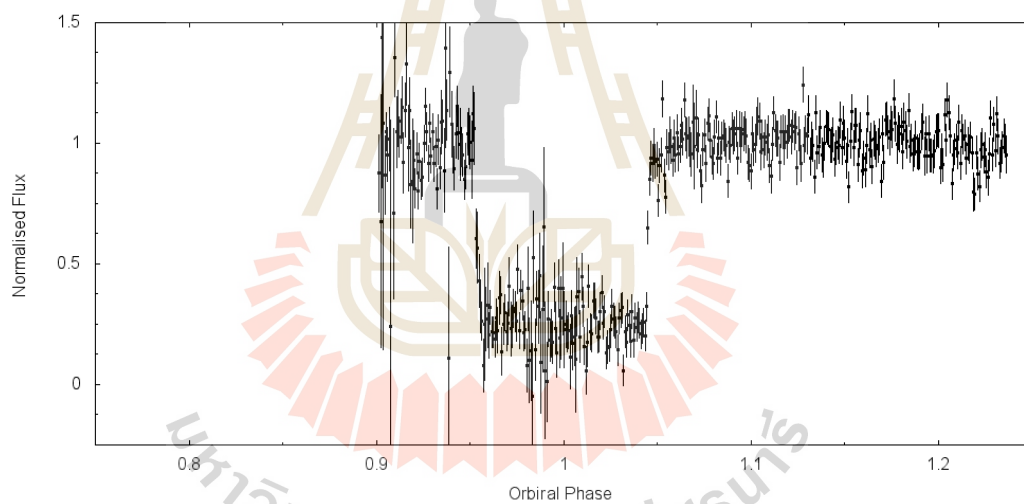


Figure B.30 Observation date on 2015, 12 May, cycle 3,489 with g' filter.

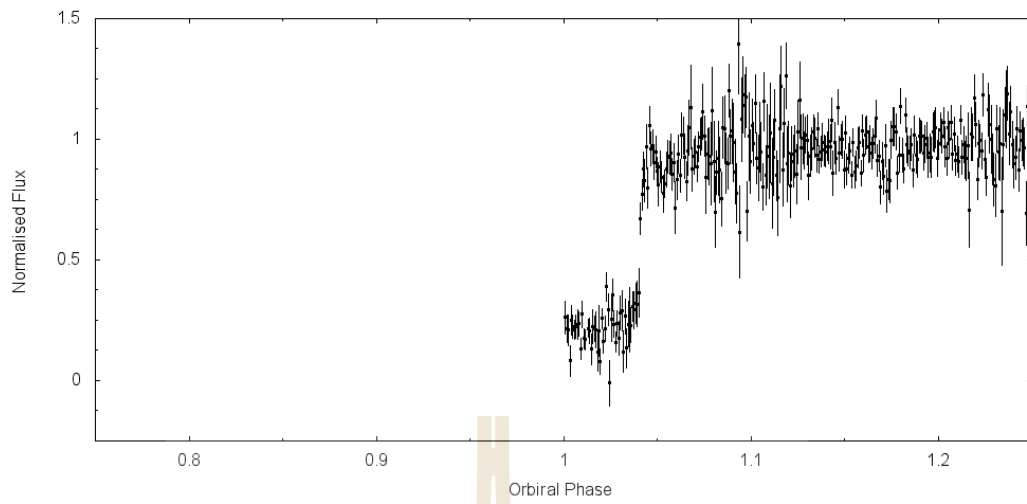


Figure B.31 Observation date on 2016, 8 Jan, cycle with g' filter.

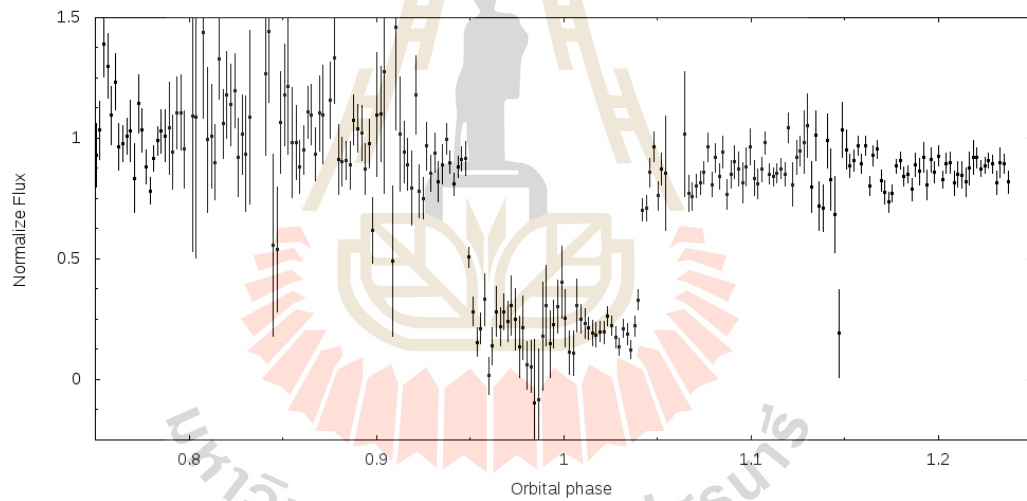


Figure B.32 Observation date on 2016, 9 Jan, cycle 5,215 with g' filter.

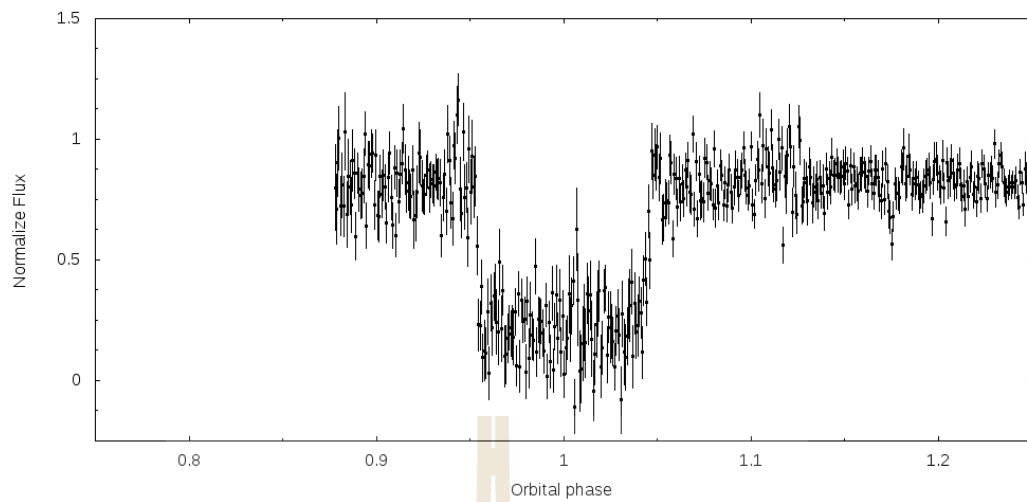


Figure B.33 Observation date on 2016, 10 Jan, cycle 5,222 with g' filter.

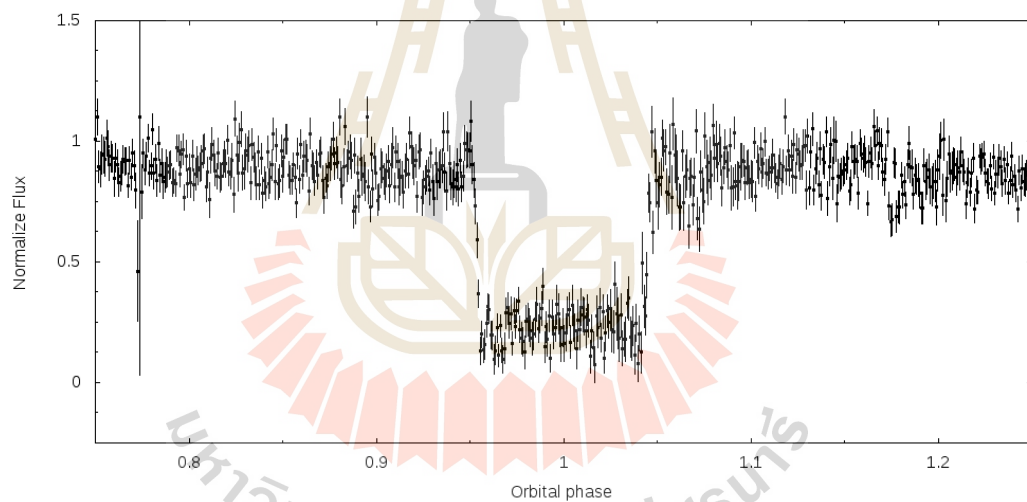


Figure B.34 Observation date on 2016, 10 Jan, cycle 5,223 with filter g' filter.

CURRICULUM VITE

Name: Khunagorn Chanthorn

Date of Birth: 11 July 1990

Place of Birth: Khon Kaen, Thailand

Education:

- Bachelor Degree of Science (Physics), Khon Kaen University
- Finished Senior and Junior High School (Grade 7-12), The Demonstration School of Khon Kaen University (Moodindaeng)
- Finished Elementary School (Grade 1-6), The Demonstration School of Khon Kaen University (Moodindaeng)

Publications

- The conference on the 12th Asia-Pacific Regional IAU Meeting (APRIM2014) in the article of “Analysis of The Eclipsing Binaries SDSS J1021+1744: A WDMS System With Unusual Dips” during 18-22 August 2014 at Daejeon South Korea.
- The conference on Siam Physics Congress 2015 (SPC2015) in article of “Analysis of Peculiar Dips Changed of SDSS J102102.25+174439.9 Light Curve” during 20-22 May 2015 at Krabi Thailand.
- Named one of the authors in article of “Analysis of The Eclipsing Binaries SDSS J1021+1744: A WDMS System With Unusual Dips” in Monthly Notices of the Royal Astronomical Society Journal (MNRAS), Published in 2015.